eman ta zabal zazu

Universidad del País Vasco

Euskal Herriko Unibertsitatea

Interaction of ions, electrons, and laser pulses with surfaces

Doctoral thesis submitted by

Iñigo Aldazabal Mensa

for the degree of Doctor of Philosophy in Physics

December 2015

Interaction of ions, electrons, and laser pulses with surfaces

Doctoral thesis submitted by

Iñigo Aldazabal Mensa

for the degree of Doctor of Philosophy in Physics

Supervisors:

Andrés Arnau Pino & Víctor H. Ponce

December 2015

[git] • Branch: tag: 3.0 @ 468feff • Release: 3.0 (2015-12-10 14:40:27 +0100)
Head tags: 3.0-0-g468feff • Author: Inigo Aldazabal `inigo_aldazabal@ehu.es`

Agradecimientos

En primer lugar quiero agradecer a mis directores de tesis, Andrés y Víctor, por la paciencia mostrada durante todos estos años, y por su apoyo en todo momento en este largo viaje que, créanlo o no, parece que llega a su fin.

To Andrei because of his hospitality on my stay on Orsay, my first time out on a research trip. Also for taking the time to show me the ins and outs of the Wave Packet Propagation technique, and for being always ready to answer questions in great detail. He made me appreciate how one can modify his own code in record times, and keep it working properly in the process. Amazing indeed!

Para José Manuel del CEIT, quien me inició en este negocio de la investigación hace ya tanto tiempo, y de quien guardo un recuerdo muy especial. Del CEIT también recordar a Cristina, Marta, Tito, Ibón, Edison y... mi hermano Josh. Todos del despacho donde... ¡se fumaba! y se hablaba de música en los descansos entre simulación y simulación.

Tras ello, en un salto a de la ingeniería a la física, un recuerdo también para mis compañeros de despacho en la facultad de Químicas: Roberto, Ibán, Remi, David y Ane. A Ane especialmente tengo que agradecerle el día que me enseñó unos comandos básicos del *vim*; sin saberlo puso en marcha un camino que ha dirigido la mayor parte de mi vida en los últimos tiempos. Además de haber creado un monstruo, jajaja. ¡Todavía recuerdo el día con claridad! Gracias Ane.

Mas tarde, ya en el DIPC, compartí muchos momentos con Txomin, Belén y Carmen. Txomin especialmente me llevó de la mano a los rincones

oscuros de lo que es mi principal trabajo hoy en día. También compartimos viajes a lugares llenos de siglas en un universo muy distinto al mío y que, gracias a ello, ya no me es tan ajeno actualmente.

Y en los últimos tiempos, ya en el CFM, un recuerdo a mis compañeros de despacho que tanto contribuyeron a poner en marcha el centro: Zuriñe, Gari y Garbiñe. Además de tener que soportarme en muchas ocasiones, son los héroes muchas veces no mencionados de las trincheras de la informática. De esta época quiero también recordar especialmente a Eli y a Ricardo, piezas clave en mi entorno durante varios años, siempre dispuestos a ayudar, y también a escuchar las penas de uno. ¡Se os echa de menos por nuestro pasillo! También un agradecimiento a Javi, por haberme permitido dedicar parte de mi tiempo a finalizar esta tesis.

Del CFM y aledaños no olvidar a mis otros viejos compañeros de desdichas y celebraciones, Asier y Xabi, y a otros no tan desdichados como Rubén y Jorge, ni a los habituales del Cine Club CFM, Mads e Ivor especialmente. El Cine Club revivirá después de esto, ¡os lo aseguro!

Ya de fuera del entorno académico, aunque no tanto, a mis amigos Guillermo, Carlos, Marta, Daniel y... Karlos, del club de las "cenas Virgen del Carmen", donde lo divino y lo humano se mezclan, y las conclusiones a las que uno puede llegar son impredecibles. ¡Hasta puede uno acabar una tesis entre cena y cena!

Todo este camino empezó hace muchos años en Zaragoza, donde se forjaron las mejores amistades de mi vida, y otras muchas cosas. No es posible olvidar a Miguel Ángel, Emiliano y Rosa, a los veo mucho menos a menudo de lo que me gustaría. Y antes a Santi, Salto, Antonio, Iñaki, Alberto,... y tantos más que sería imposible de enumerar.

Y por supuesto, a mis padres, sin los que hoy no estaría escribiendo estas palabras, y a los que tengo que agradecer especialmente por ser como son: ¡los mejores padres que pueda uno tener! Y por aguantarme y soportar mis cosas estoicamente durante tanto tiempo.

Mi hermano Josh siempre ha estado ahí para contarnos las penas y darnos la chapa bien a gusto en modo binario 0100011011. ¡Y lo bien que nos lo pasamos!

Y por último, como no podía ser de otra forma, a María por aguantar mis interminables chapas y rarezas durante todos estos años y estar siempre ahí. Y a Inés, mi dibujante de cómics, artista y geek favorita, por

alegrarme todos los días, aunque ella crea que su trabajo sea justamente el contrario. ¡No lo conseguirás! jajaja. ¡Os quiero!

San Sebastian, diciembre del 2015.

Resumen

Following the UPV/EHU regulations for thesis submitted in languages other than the official ones in the University, a brief summary in Spanish of the thesis follows.

Siguiendo la normativa de la UPV/EHU sobre tesis doctorales redactadas en lenguas no oficiales de la universidad, se presenta a continuación un breve resumen en castellano del presente manuscrito.

La presente tesis se centra en el estudio teórico del efecto que ciertas perturbaciones ejercen sobre superficies cristalinas, tanto aislantes como conductoras. Veremos cómo estas superficies, y más específicamente sus propiedades electrónicas, responden cuando suceden estas perturbaciones.

Como estudiaremos procesos que suceden en la escala atómica utilizaremos para este trabajo un formalismo mecánico cuántico, basándonos en modelos habituales tanto de física atómica como de física de superficies y de estado sólido.

El objetivo general será llegar a entender lo esencial de los fenómenos que tengan lugar en los sistema a estudiar, más que a obtener una predicción o reproducción numérica precisa de una medida experimental. Esto nos llevará a obtener un conocimiento más profundo de los fenómenos implicados, lo que nos permitirá por un lado dar una interpretación física a los resultados experimentales, y por otro diseñar nuevos experimentos.

La forma general de proceder consistirá en realizar en primer lugar un modelo físico–matemático de nuestro sistema en base a ciertas simplificaciones, para posteriormente resolver dichos modelos numéricamente.

El desarrollo de las técnicas numéricas de computación necesarias para esta resolución ha constituido gran parte del trabajo llevado a cabo para esta tesis.

A lo largo de la tesis se han estudiado tres sistemas físicos diferentes, lo que viene reflejado en la división en tres partes diferenciadas de la presente memoria[1]

En la Parte I estudiaremos la emisión electrónica resultante de la colisión de un protón de alta energía en colisión rasante con una superficie cristalina aislante. Modelizaremos los procesos principales de intercambio de carga a lo largo de la trayectoria que sigue el proyectil, con el fin de entender el peso que cada uno de ellos tiene en el espectro final de emisión electrónica.

En la Parte II, veremos cómo islas de tamaño atómico depositadas sobre superficies metálicas afectan a las propiedades electrónicas de estas superficies. Modelizaremos la física de un microscopio de efecto túnel (*Scanning Tunneling Microscopy – STM*) en ciertas configuraciones experimentales con el fin de determinar el efecto que sobre las mediciones tiene por un lado el tamaño de la punta del microscopio, y por otro la presencia de las islas adsorbidas.

La Parte III representa una mezcla entre los sistemas estudiados en las Partes I y II, y se realizó en el momento de transición entre ambos campos de investigación. Estudiaremos, al igual que en la Parte I, la emisión electrónica de una superficie, en este caso debida a la influencia de un pulso láser incidiendo de forma rasante sobre la misma.

A continuación se describen algo más en profundidad cada una de las partes, así como las conclusiones que se han podido extraer en cada una de ellas.

Parte I: Emisión electrónica en colisiones rasantes de protones con superficies aislantes

Cuando protones de alta energía colisionan con superficies aislantes de forma rasante, la interacción entre dichos protones y la superficie da lugar

[1]La estructura la presente memoria se basa en la compilación de los artículos publicados como resultado del trabajo realizado. Los capítulos principales en los que se divide este documento corresponden con cada uno de dichos artículos, reproducidos tal y como fueron publicados.

a una emisión de electrones de la superficie. El espectro de esta emisión electrónica producto de la colisión nos da información sobre la estructura electrónica tanto del proyectil como de la superficie, así como de las diferentes interacciones que se dan a lo largo de la trayectoria del proyectil. Este espectro presenta, en la región de alta energía, dos picos bien definidos, típicos de colisiones atómicas: los llamados picos binario y convoy. En nuestro estudio nos fijaremos específicamente en los electrones convoy, así llamados por "seguir" al proyectil en su trayectoria.

El hecho de tratar con colisiones rasantes implica que, debido a la baja velocidad perpendicular a la superficie del proyectil, el mismo no puede penetrar en el material y es reflejado por la superficie. Esto, unido al hecho de que las superficies de estudio son aislantes típicos con una banda de energía prohibida (*gap*) ancha y una banda de valencia estrecha, nos permite asumir que el proyectil únicamente interaccionará con los electrones de valencia pertenecientes a la capa atómica más superficial del material. Además, debido al carácter localizado de los electrones de valencia, la interacción entre el proyectil y la superficie puede ser vista como el efecto acumulado de colisiones individuales del proyectil con cada uno de los átomos de la superficie.

De esta forma, el problema de la colisión proyectil–superficie se reduce a un problema de múltiples colisiones binarias con los átomos de la superficie.

En la interacción del proyectil con la superficie se dan tres procesos de intercambio de carga: i) los electrones de la superficie son capturados por el proyectil que es neutralizado, ii) los electrones de la superficie son extraidos de la misma, pero no capturados por el proyectil, en el proceso denominado *Electron Capture to the Continuum* (ECC), y iii) los electrones previamente capturados por el proyectil son reemitidos a estados del contínuo en el proceso denominado *Electron Loss to the Continuum* (ELC).

Concretamente la contribución al pico de convoy de los electrones del proceso de ELC es el principal objeto de estudio de esta parte de la tesis.

En el Capítulo 1 planteamos un primer modelo básico para la colisión proyectil–átomo superficial sobre el que construiremos posteriormente un modelo más completo de todo el proceso de colisión. Mediante este modelo calculamos la sección eficaz de colisión doblemente diferencial en función de la altura sobre la superficie. Esto, junto al cálculo de la trayectoria

usando un potencial planar semiempírico para la la superficie, nos permite calcular la emisión electrónica para la colisión en función de la energía y el ángulo de emisión de los electrones.

Los resultados nos muestran que con un modelo sencillo de colisión binaria podemos reproducir cualitativamente el comportamiento del pico convoy en función del ángulo de emisión electrónica. Además, el modelo está realizado de forma que pueda ser utilizado con otras superficies sin más que modificar algunos parámetros.

En el Capítulo 2 ampliamos el modelo previo de electrones ELC con una descripción más completa del sistema, teniendo en cuenta en este caso la probabilidad de emisión electrónica de electrones superficiales (ECC). Adicionalmente calculamos la probabilidad de que el proyectil se encuentre en estado neutralizado, frente al ionizado inicialmente, a lo largo de su trayectoria.

Así, teniendo en cuenta este estado de carga del proyectil utilizamos dicha información para pesar las probabilidades de emisión ELC y ECC y de esta forma calcular la sección eficaz de emisión electrónica, pero manteniendo el conocimiento de las contribuciones relativas de los electrones originados en cada proceso.

Analizando estas contribuciones encontramos que, a la energía alrededor del pico convoy y a bajos ángulo de emisión, ambas son del mismo orden, siendo la contribución del proyectil (ELC) algo mayor. Si nos movemos a ángulos de emisión mayores vemos que la contribución de los electrones superficiales al pico convoy se hace despreciable, y en este caso prácticamente todos los electrones del (disminuido) pico convoy proceden de la ionización del proyectil.

Finalmente en el Capítulo 3 aplicamos el modelo desarrollado previamente al estudio de diferentes superficies, y para incidencias tanto de protones como de hidrógeno neutro. Calculamos para estos sistemas la emisión electrónica total y estudiamos las contribuciones respectivas de electrones ECC y ELC.

En este caso podemos concluir que, debido a la baja probabilidad del proyectil de encontrarse en su estado de carga neutro en su trayectoria de colisión, la contribución de los electrones del mismo a la emisión electrónica total es en este caso despreciable frente a los electrones procedentes de la superficie.

Parte II: Resonancias de emisión de campo en superficies de Cu(100)

El estudio de los fenómenos que suceden sobre superficies metálicas requiere de un entendimiento en profundidad de la dinámica de los electrones en dicha superficie.

Con el fin de estudiar esta dinámica, la espectroscopía de efecto túnel (*Scanning Tunneling Spectroscopy – STS*), una extensión de la técnicas de microscopía de efecto túnel, ha resultado ser una técnica experimental adecuada para obtener información cualitativa sobre la misma. En un STM, su punta metálica se coloca muy próxima, del orden de décimas de nanómetros, al material conductor a estudiar y se aplica una diferencia de potencial entre la punta y la muestra. Esta diferencia de potencial permite que, debido al efecto túnel, los electrones pasen de la punta a la muestra a través del vacío intermedio. Esto produce una corriente eléctrica que puede ser medida experimentalmente y que depende, esencialmente, de la posición de la punta, el voltaje aplicado y la densidad local de estados (*Local Density of States – LDOS*) del sistema punta–muestra.

Típicamente se coloca la punta en una posición concreta sobre la superficie y se mide la corriente túnel en función de la energía de los electrones, variando el voltaje punta–muestra aplicado. De esta forma, midiendo la variación de la corriente en función de la energía de los electrones (i.e. el voltaje aplicado), se obtiene un espectro de la corriente túnel denominado curva dI/dV.

Estos experimentos se llevan a cabo normalmente en condiciones de bajo voltaje punta–muestra, de forma que el campo eléctrico aplicado no perturbe de forma significativa las medidas. Sin embargo, si este voltaje aplicado se incrementa, la barrera de potencial que los electrones tienen que superar se eleva sobre el nivel de vacío de la superficie, lo que da lugar a la creación de nuevas resonancias que no existían en el régimen de bajo voltaje; las denominadas resonancias de emisión de campo (*field-emission resonances – FERs*).

Sucede que estas resonancias, si bien están relacionadas con el proceso de medida en si, nos pueden proporcionar información sobre la dinámica electrónica y las propiedades electrónicas de la superficie por encima del nivel de vacío.

En esta parte de la tesis nos centraremos precisamente en el estudio de dos factores que afectan a estas resonancias de emisión de campo. Veremos el efecto que sobre ellas tienen por una lado la extensión lateral de la propia punta de medida, y por otro la deposición de islas de tamaño nanométrico sobre la superficie.

En el Capítulo 4 estudiamos el efecto que la extensión lateral de la punta del STM tiene sobre la distribución del momento de los electrones, así como la forma en que el proceso de medida misma afecta al espectro dI/dV.

Para ello se desarrollan dos modelos teóricos. En el primero se propone un potencial unidimensional como forma de representar el efecto que la curvatura de la punta (que nos da su extensión lateral) tiene sobre la distribución de momentos de los electrones. Este modelo nos permite estudiar grosso modo la densidad electrónica en la superficie y reproduce cualitativamente los patrones de onda estacionaria observados experimentalmente, lo que nos permite dar una interpretación física a los mismos.

En el segundo modelo, también basado en un potencial unidimensional, tratamos esta vez de reproducir las características esenciales del sistema punta–muestra a lo largo de su eje de simetría longitudinal, perpendicular a la superficie. Utilizamos potenciales modelo típicos para la punta (modelo simple de jellium) y la superficie (potencial de Chulkov que reproduce magnitud y posición de la banda prohibida en el punto $\overline{\Gamma}$), así como un potencial complejo que emula las transmisiones electrónicas dentro del gap debidas a efectos de dispersión inelástica.

Este modelo nos permite explicar el ensanchamiento observado en los picos del espectro de dI/dV como debido a la forma en la que se realizan las medidas, es decir, utilizando un ajuste dinámico del sistema para obtener las condiciones deseadas de intensidad de corriente constante.

En el Capítulo 5 estudiamos el efecto que islas de metales alcalinos adsorbidas en la superficie tienen sobre la resonancias de efecto de campo.

En este caso utilizamos un modelo completo tridimensional del sistema, restringiendo el estudio a casos de simetría cilíndrica con un fin doble; por un lado el de facilitar los procesos de resolución numérica y, por otro, obtener una relación entre cada uno de los picos FER y los subespacios de simetría m del sistema[2].

[2]Siendo m la proyección del momento angular sobre el eje de simetría del sistema, z

Los potenciales utilizados para modelizar los diferentes elementos del montaje experimental son calculados por separado y luego agrupados formando el sistema completo. Para la isla adsorbida utilizamos un potencial obtenido de cálculos basados en la teoría del funcional de densidad (*Density Functional Theory – DFT*). Para la superficie utilizamos un potencial semi-empírico que reproduce las características principales de la misma (potencial de Chulkov), al que añadimos, como en el caso anterior, un potencial complejo que simule los efectos de dispersión inelástica. Finalmente, para la punta utilizamos un potencial simple de tipo jellium.

Utilizando el potencial del sistema completo así obtenido, podemos calcular la dependencia con la energía del los coeficientes de transmisión electrónica a través de la barrera túnel, lo que nos permitirá a su vez explicar las medidas relevantes. Para obtener estos valores utilizamos la técnica de propagación de paquetes de onda (*Wave Packet Propagation – WPP*), en la que un paquete de ondas monoelectrónico es propagado desde la punta hacia la muestra, y a través de la separación entre ambas. Para calcular dicha propagación resolvemos la ecuación de Schrödinger dependiente del tiempo para el sistema completo. Debido a la simetría del sistema, la evolución temporal de cada subespacio m se realiza de forma independiente.

Con el fin de identificar el carácter superficial o de isla de las resonancias procedemos de forma idéntica a como se realizan los experimentos: en primer lugar calculamos las resonancias de la superficie desnuda, para posteriormente añadir el potencial de la isla adsorbida y repetir los cálculos en las mismas condiciones. Comparando ambos resultados podemos identificar efectivamente los orígenes de las diferentes resonancias.

De este análisis podemos concluir que las resonancias asociadas a la superficie están deslocalizadas sobre la misma y tienen contribuciones de todos los canales m, mientras que las resonancias originadas en las islas tiene un carácter m bien definido. También observamos que, debido al efecto de la barrera centrífuga, el número de resonancias localizadas en la isla disminuye drásticamente al aumentar m. Este efecto es tan pronunciado que, en nuestro caso de islas pequeñas, solo las resonancias de la isla en el canal $m = 0$ contribuyen al espectro final.

Nuestro modelo también nos permite obtener planos de corte de la densidad de carga en planos paralelos a la superficie. Comparando éstos con las medidas experimentales de mapas de dI/dV observamos que cualitativamente obtenemos una buena concordancia entre ambos, en lo que

respecta a las formas y distribución de las distribuciones de carga para los diferentes canales. Estos cálculos nos permiten concluir, en lo que respecta a la distribución espacial de las resonancias, que aquellas con origen en la isla se localizan espacialmente en el centro de las mismas, mientras que las resonancias mezcla de estados de la isla y de la superficie formas estructuras con forma de anillo que se extienden desde el borde de la isla hacia afuera de la misma.

Parte III: Emisión electrónica en metales inducida por láseres

Para la realización de esta parte de la tesis se utiliza una combinación de las técnicas desarrolladas previamente en las Partes I y II. Mientras se estaban desarrollando las técnicas numéricas para la resolución de la ecuación de Schrödinger dependiente del tiempo en la Parte II, se propuso realizar un modelo para el estudio de la emisión electrónica inducida por pulsos láser sobre superficies metálicas. Este sistema presentaba por un lado elementos de emisión electrónica por superficies, tema ya estudiado en la Parte I, y otro resolución de la evolución temporal de un sistema a través de la resolución de la ecuación de Schrödinger dependiente del tiempo, tal y como se estaba estudiando en la Parte II.

El objetivo del estudio es obtener información sobre la dinámica electrónica en superficies metálicas, pero en este caso estudiando el proceso de fotoemisión inducido por pulsos láser ultra-cortos incidiendo de forma rasante sobre dichas superficies. Cuando un pulso láser incide sobre una superficie metálica, la redistribución que el campo electromagnético de éste induce sobre los electrones de valencia del metal da lugar a su vez a un potencial inducido. Para frecuencias mayores que la del plasmón superficial los electrones no son capaces de responder lo suficientemente rápido al campo láser, de que forma el potencial inducido no se creará y no es de esperar efecto alguno sobre la emisión electrónica. Sin embargo, para frecuencias del pulso cercanas a, o por debajo de, la frecuencia del plasmón superficial, los electrones superficiales pueden seguir las fluctuaciones del campo láser de forma que el potencial creado por la redistribución de carga es de esperar que pueda ser del orden de el del propio láser. En estos casos, el potencial inducido no puede ser ignorado a priori ya que parecería que su efecto pudiera ser relevante en los procesos de emisión electrónica.

En esta parte calculamos la probabilidad de emisión electrónica de electrones en la banda de valencia de la superficie bajo la incidencia de pulsos láser de diferentes frecuencias y duraciones, analizando el efecto del potencial inducido sobre la emisión electrónica final.

Para ello utilizamos un modelo de jellium para la superficie y, como consideramos la incidencia del láser paralela a la superficie por ser incidencia rasante, modelizamos el láser como un campo eleć trico uniforme, perpendicular a la superficie, y que varía en el tiempo. Para obtener el potencial inducido utilizamos la teoría de respuesta lineal que nos permite calcular la densidad electrónica inducida en la superficie por el pulso láser, y de ella este potencial.

Para realizar los cálculos de emisión electrónica se utilizan dos modelos diferentes que tienen en cuenta el potencial inducido, y un tercer modelo en el que éste no es tenido en cuenta con el fin de observar el efecto causado por la introducción del mismo. No teniendo resultados experimentales directos con los que realizar comparaciones, el uso de dos modelos diferentes nos permitirá validar nuestros resultados.

Una vez realizados los cálculos obtenemos, en todos los casos estudiados, una concordancia cuantitativa entre los resultados de los dos modelos que tienen en cuenta el potencial inducido. Las comparaciones con el modelo que no tiene en cuenta el efecto del potencial inducido muestran, como era de esperar, discrepancias en los casos de frecuencias cercanas y por debajo de la del plasmón superficial. De estos resultados podemos concluir que, para frecuencias alrededor de la del plasmón superficial, el potencial inducido produce un incremento notable en la probabilidad de emisión electrónica. Asimismo, observamos que al reducir la frecuencia tendiendo al caso estático, la densidad electrónica inducida apantalla el campo eléctrico en el interior del sólido, dando lugar a una reducción en el número de electrones emitidos.

También se estudia el caso del denominado régimen colisional, asociado con pulsos de solo medio ciclo, donde el campo electromagnético no oscila y produce una perturbación similar a la de un ioń rápido incidiendo sobre la superficie. En estos casos observamos que, una vez el pulso finaliza, el potencial inducido permanece oscilando de manera apreciable a medida que se atenúa, dando lugar a un incremento de la emisión electrónica a bajas velocidades, lo que produce un máximo en el espectro de emisión a bajas energías.

Contents

Introduction

Preamble

The present work focuses on the theoretical study of the effects taking place at crystal surfaces, both insulators and conductors, under different perturbations. We will see how these surfaces, and more specifically their electronic properties, react when these perturbations occur.

As we will be dealing with processes taking place at the atomic scale, a Quantum Mechanical treatment of the systems will be used, mainly by means of Atomic and Surface Physics models. In all cases, the objective will be to grasp the essential features of the phenomena that are taking place, rather than achieving a numerically exact prediction or a precise reproduction of the experimental results. This understanding of the essential features of our systems will allow us to give a better interpretation of the experimental data, as well as to design new experiments more thoughtfully .

The general way to proceed will be first setting up a theoretical model for our physical systems based on some basic assumptions and simplifications. Then, as those models are typically not analytically solvable, we will develop some computing codes and algorithms in order to numerically solve them under the desired initial conditions. In order to do this, advanced usage on Scientific Computing techniques and specific High Performance Computing hardware equipment will be used. This scientific numerical codes development, as well as their execution and results post-processing and analysis, will be one of the main tasks carried out in this thesis.

We will consider three different physical systems that are studied in each of the three Parts in which the present work is divided.

In Part I, we will study the electron emission resulting from a grazing collision of a high energy proton projectile against an insulator surface. We will model the main processes occurring as the projectile moves along its trajectory, as well as the trajectory itself, in order to understand the different contributions to the peaks appearing in the electron emission experimental spectra. In this Part we will show the evolution of the model from a basic collision one, up to a much more complete description of the system accounting for the essential features of the proton–surface collision, as well as for the projectile charge states along its trajectory.

In Part II, we will focus our attention on metallic surfaces. We will see how atomic-sized islands deposited on top of the atomic surface affect the surface electronic properties. We will model a Scanning Tunelling Microscope system in order to simulate the experimental setup, and see first how the microscope tip size and shape would affect a certain type of measurements, and second how would those measurements be modified by the presence of an adsorbate island placed on top of the surface.

Part III represents a link between Part I and Part II, and happened in time as we were transitioning from one field of study to the other. In this case we will study, as in Part I, induced electron emission from surfaces but, instead, as in Part II, happening on metallic surfaces: we will model the electron emission from metallic surfaces under the influence of a short laser pulse that impinges grazingly on them.

Manuscript structure

The present manuscript is based on a compilation of the published papers result of the work carried out along the thesis.

Apart from this general introduction, the thesis main chapters reproduce the papers as–published in the corresponding peer–reviewed journals[3]. Each of the three Parts conforming the main body of the present work group together papers related to a same system under study. A general section summarizing the main conclusions of the work has been added, as well as a list of the publications derived from the present work. Also, and following UPV/EHU internal normative regarding thesis pre-

[3]See every chapter preamble for a reference to the original paper.

sented in languages other than the official ones in the University, an intial small section has been added, containing a general summary of the thesis in Spanish language.

In what follows, the these three Parts of the thesis are presented. For every Part a background on the study, as well as the general motivations for it, is given. This is followed by a summary of the general strategy followed along the study, as well as the main hypothesis used. Finally, a brief description of the work methodology used, mainly related to the computational work developed, is given.

Part I: Electron emission in grazing collisions of protons with insulator surfaces

When high energy protons collide with crystal insulator surfaces in a grazing trajectory, electrons are emitted as a consequence of the proton–surface interaction. The electron spectra resulting from these collisions bring information from both the electronic structure of the target and projectile electrons, as well as from the different interactions happening along the collision path [1–5]. The low energy region of the spectra reflects the distribution of the density of final estates, the surface electronic structure and the residual interaction charges of the combined projectile–target system. In our case this low energy area of the spectra does not present any significant feature but, on the other hand, the high energy region shows two distinctive cusps; the so-called *convoy* and *binary* peaks, well known from atomic collisions [6–8]. Specifically, the convoy electrons[4] peak structure has been object of study both from the theoretical and the experimental points of view for long [6, 9, 10], and we will focus on them in this part ot the thesis.

Having a grazing incidence collision means that the projectile energy in the direction perpendicular to the surface is very small, in fact so small that the projectile can not penetrate the material and it is reflected by the surface. Since the materials we will study are typical broad band-gap insulators, with a narrow valence band and with their valence electrons keeping most of their atomic character, under this collision geometry the projectile will essentially interact with the valence electrons belonging to the surface top most atomic plane. Furthermore, the localized character

[4]These electrons move at velocities and trajectories close to the impinging proton ones, "following" the projectile in its way; thus their name.

of the valence electrons will also allow us to assume that the interaction between the projectile and the surface can be viewed as the added effect of individual, independent interactions between the projectile and every atom at the surface [11]. Thus, effectively, the projectile-surface collision problem is reduced to a multiple binary collisions one: the projectile along its trajectory will suffer a series of successive single collisions with the surface atoms [12].

As the projectile interacts with the surface atoms, three different charge exchange processes occur: i) electrons from the surface are captured into the projectile bound states so that it becomes a neutral Hydrogen atom, ii) electrons are extracted from the surface without being captured by the projectile in the so-called *Electron Capture to the Continuum* (ECC) process, and iii) surface electrons previously captured by the projectile are reemitted into continuum states in the process named *Electron Loss to the Continuum* (ELC). Precisely the ELC contribution to both the convoy electron peak and to the total electron emission yield is the main subject of the study carried out in Part I of the present work. The papers published as a result of this study conform Chapters 1, 2 and 3 of this manuscript.

The different chapters reflect the natural evolution of the study, going from a simple model for the collision system for a neutral Hydrogen projectile to a final stage in which different effects are considered, accounting for a more realistic approach to electron emission along the collision trajectory. Finally, calculations are done for different target materials, taking into account all previously studied effects.

In Chapter 1 we settle the basic ELC emission model that will be the building block for the rest of the study. We use a collision model [13, 14] for the neutral Hydrogen–surface atoms system which accounts for the surface electronic characteristics, and from it we calculate the *doubly differential ionization cross section* (DDCS) for the ELC electrons. Integrating this DDCS along the projectile trajectory we obtain the total electron emission probability from ELC as a function of the emission angle. In these calculations we do not account for the charge state of the projectile and we assume a neutral H^0 projectile at all times along the collision path. This has to be viewed as a first approach to the collision problem, and the charge state of the projectile will be taken into account in later stages of the study.

For the neutral Hydrogen–surface collision we consider, as has already been mentioned, binary collision between the H^0 and the surface electrons. We calculate the collision DDCS as a function of the impact parameter, in the first Born approximation [15]. This collision DDCS is calculated in the projectile center of mass frame of reference, to be later brought to the laboratory frame of reference through a Galilean transformation. The surface electrons are considered to have a certain momentum distribution which accounts for the material to study, LiF in this case, and it will allow us to generalize the model to different surfaces. This momentum distribution is included by means of the *incoherent scattering function*, which accounts for the target electronic structure and its excitations [16].

For computing the projectile trajectory we use a semi-empirical planar potential for the surface [17] acting on a bare H^+ ion. We can assume a bare ion for the projectile as, at the energies we are working, the proton capture cross section is about ten times lower that the ionization cross section, thus the Hydrogen atom will be most of the trajectory in its ionized state. Once we compute the trajectory, the integration of the DDCS along it finally gives us the ELC electron emission spectra[5].

In Chapter 2 we include the previous ELC model in a more complete description of the collision system. Regarding the electron emission, we now take into account the surface electrons emission probability in addition to the projectile emitted electrons. We also calculate the probabilities of both the projectile being ionized from its neutral states and the projectile being neutralized from its ionized state, as a function of the height above the surface. This allows us to compute the projectile charge state along its trajectory over the surface. Weighting the ELC and ECC emission cross sections previously calculated with the data for the projectile charge state along its trajectory, we can calculate the final electron emission cross section, while keeping the knowledge of the separate contributions from both the ELC and ECC electrons. In this Chapter we again consider impinging protons against a LiF surface.

In addition to the hypothesis used in Chapter 1, we make use of the *continuum-distorted-wave eikonal-initial-state* (CDW-EIS) approximation [18, 19] for the surface ECC electrons, and the *exact eikonal im-*

[5]This is just an theoretical result, as in reality we will have to weight the ELC emission with the charge state of the projectile, and we already know that the projectile will be most of the time in its ionized stated as just mentioned. This way, once we later account for this effect, this magnitude will be much reduced.

pulse approximation to evaluate the probability of electron capture by the ionized projectile [20, 21].

Finally in Chapter 3 no new hypothesis are made and the work is mainly an application of the model developed in Chapters 1 and 2 to different collisions geometries, energies and surfaces, where experiments are available.

Using the model developed in the previous Chapters, the study is generalized to different target surfaces, namely LiF, KCl and KI and also in some cases H^0 projectiles are considered. Calculations are done for different incidence angles as well as for different impact energies. Total electron emission yields are calculated and the respective contributions of the ELC and ECC processes are analyzed. Also comparisons are done with experimental results.

The work carried out in this Part I consisted in two clearly separated aspects: the development of the collision physical models with their corresponding approximations and hypothesis, on the one hand, and the numerical resolution of these models in order to obtain specific results on the other.

For the numerical calculations specific numerical codes were developed. This development, together with the results testing and code debugging and optimization, represented a substantial part of the total work carried out in this Part. The more heavy calculations where developed in the C programming language making use in part of the GNU Scientific Library (GSL) [22], while GNU *awk* was used as a scripting language for data pre and post processing. Figures were produced using xmgrace and xfig plotting software. Exclusively Open Source / Free software was used for all the computing related tasks.

Part II: Field Emission Resonances in Cu(100) surfaces

Understanding the phenomena taking place at metallic surfaces, such as electron scattering and charge transport dynamics across interfaces, as well as the influence adsorbates and surface defects have on those, requires a detailed knowledge of the surfaces' electron dynamics.

Scanning Tunneling Spectroscopy (STS), an extension of the *Scanning Tunneling Microscopy* (STM), has become an experimental technique which can provide qualitative information about the electron dy-

namics at metal surfaces [23–27]. In STM, a metallic tip is brought very close, of the order tenths of a nanometers, to the conducting sample to be studied and a bias voltage is applied between the tip and the sample. The applied bias allows electrons to tunnel through the vacuum existing between the tip and the sample[6], thus producing a current between both that can be experimentally measured. This current essentially depends on the tip position, bias voltage, and the *local density of states* (LDOS) of the sample. STS allows to measure the number of electrons on the surface-tip system (i.e. essentially the LDOS) as a function of the electron energy. Basically the STM tip is placed at a fixed position over the surface and the tunneling current is measured as a function of the electron energy by varying the tip–surface applied bias voltage. A tunneling spectrum, typically called dI/dV curve, is obtained from the change in the current in relation to the energy of the electrons (given by the bias voltage).

Those experimental studies are typically conducted using low tip–surface bias voltages so that the applied electric field does not play a relevant role in the resulting measurements [28]. However, as the bias voltages become larger than the tip work function, the applied electric field raises the potential barrier the electrons have to overcome above the surface vacuum level. As a consequence of this, new resonances appear that are not present in the low bias regimes, the so-called field-emission resonances (FERs) [29, 30].

It turns out that these FERs, even if being related to the bias voltage and hence to the measurement process itself, carry information about the intrinsic properties of the surface, specifically about the electron dynamics and surface electronic properties at energies above the vacuum level. Through these information, they allow us to identify different surface elements [31–35] and additionally, and more relevant in our case, to study the effects that nanometer-size metallic and molecular adsorbed structures have on the bare surface electron LDOS and thus, on the whole system electron dynamics of hot electrons.

In Chapters 4 and 5 we present both an experimental STM study as well as a theoretical model for the tip–surface system which will allow us to interpret these experimental results. The theoretical and computational aspects of this study constitute the essence of the work carried out for this Part of the thesis.

[6] hence the name of *tunneling microscopy*

In Chapter 4 we study the effect the STM tip lateral size has over the electronic momentum distribution, as well as the way in which the measurement process itself affects the dI/dV spectra.

In order to obtain an insight into the experimental results, two theoretical models are developed. First, a very simple one dimensional potential is proposed as a way to mimic the lateral effect of the finite curvature of the tip on the electron wave vector distribution. This potential has its maximum at the tip axis position and vanishes as we move away from this point. For this one dimensional potential box, we compute the charge density of electrons with energies just below, slightly above, and above the "tip" induced potential. We then compute their corresponding Fourier Transformation in order to compare it with the equivalent experimental measurements.

A second one-dimensional potential is also proposed. In this case modeling the system along the tip longitudinal axis, that is perpendicular to the surface plane, in order to better understand the experimental dI/dV spectra. A free-electron-like behavior is assumed in the directions parallel to the surface in order to have a full 3D model. In this case we want to have a realistic model for the tip–surface physical system, as compared to the "toy" model just described for the tip lateral extension. For the tip a simple jellium potential with a certain work function and Fermi energy is used, while for the surface we consider a periodic sinusoidal potential which reproduces the magnitude and position of the energy gap at the $\overline{\Gamma}$ point [36]. Also, a complex potential at the surface is included in order to model electron transmissions inside the gap due to inelastic scattering effects [37, 38].

In both cases the aim of the models is to provide a qualitative understanding of the effect the tip has on the electron dynamics, in the first case because of we are using a very simplified "toy" model, and in the second as a cause of the lack of quantitative information about some of the system parameters such as the effective tunneling areas, tip-sample distances or tip work functions.

In Chapter 5 we study the effect that adsorbed alkali islands on the nanometer size, i.e. nanoislands, have on the bare surface FERs.

Experiments are carried out on Cu(100) surfaces with Li islands over it. dI/dV spectra are measured with and without islands, as well as STM topographies and dI/dV maps at the resonance peaks positions.

In this case we use a full three dimensional model, although we restrict ourselves to a cylindrical symmetry geometry in order to both make the calculation times of a reasonable duration, as well as to clearly relate the origin of every FER peak to a m-symmetry subspace, being m the projection of the angular momentum over the symmetry axis, z. As in the previous Chapter, the theoretical model does not pretend to provide a full quantitative agreement with the experiments, but to draw conclusions generic to any alkali adsorbate island structures deposited on noble metal surfaces with a projected band-gap.

The potentials used for the model are calculated separately and later on added together to get the full system potential, and are described in what follows.

For the adsorbate island, and as the essential features of the model do not depend on the specific alkali, we use a model potential based on a Density Functional Theory calculation for Na islands on Cu(111) surfaces developed for previous works [39,40] , and adapt it to the Cu(100) surface.

For the surface we use a semi-empirical parametrized one-electron model potential, the so-called *Chulkov* potential, for the Cu(100) case. This potential reproduces the essential features of the surface such as the projected band gap and the surface image states [36]. We also add an imaginary potential inside the metal which accounts for inelastic scattering effects inside the gap [37, 38], exactly as we did in the previous Chapter.

The tip is again modeled by a simple jellium potential with a certain work function and Fermi energy. The applied electric field is then defined as the potential difference between the tip and the surface Fermi levels. As we work in the field emission regime and the tip radius of curvature is bigger than both the typical island diameters and the tip–surface distances, electrons will tunnel from the tip mesoscopic surface and we can therefore neglect the radius of curvature of the tip and use the flat tip approximation [41, 42].

Using this model potential for the system we can compute the energy dependence of the electron transmission coefficients across the tunneling barrier. This allows us to emulate the experimental measurements we are interested in, and many more, such as the current-voltage, conductance-voltage and distance-voltage characteristics, real space maps of the electronics wave function at a given energy as well as the projected density of

electronic states. In order to compute this, we use the *wave packet propagation* (WPP) technique [43, 44], in which a one-electron wave packet is propagated from the tip, through the junction, and into the surface, by solving the *time dependent Schrödinger equation* (TDSE) of the system. As mentioned previously, our model presents cylindrical symmetry so that in our case m is a good quantum number, and thus the time evolution for the different m-subspaces can be treated independently.

To numerically compute the TDSE time evolution, the *split operator technique* [45,46] is used. The initial wave packet is chosen to be gaussian-like shaped on the tip axis component, z, and its parameters selected so that in every calculation i) it has no sensible overlap over the STM junction, and ii) its energy spectrum covers the energy range of interest for the "measurement".

In order to determine the tunneling current the *virtual detector method* [47] is used, in which we measure in a certain z-plane the transmission flux from the tip into the surface, for every m channel. This allows us to compute the total tunneling transmission flux and from it the total current I(V,Z), as well as the current-voltage, conductance-voltage and distance-voltage characteristics.

To identify the surface-like or island-like character of the calculated FERs, we adopt the same strategy as the one used in the experiments, that is comparing spectra taken on top of the bare metal surface against the ones taken on top of the alkali island.

The numerical calculations for this part were extensive and required the use of High Performance Computing (HPC) equipment[7]. A single m-state calculation took of the order of hours in a single core machine, so that the codes had to be parallelized in order to be able to achieve the desired results in a reasonable amount of time. The Message Passing Interface (MPI) parallelization paradigm was used for the parallelization and, due to the orthogonality of the quantum base we were using, we were able to evolve every quantum space component independently, obtaining an almost linear parallelization scaling up to the order of 10^2 processes. A generic loop parallelization library, appropriately named *loopsplit*, was developed for the task, having both C and FORTRAN bindings, and has been later reused in other projects.

[7]Donostia International Physics Center (DIPC) HPC facilities were used for the calculations

Also, diverse methods were specifically developed for the calculations, such as a Poisson solver for the tip accounting for tip-surface multiple images, written in C, and a high level driver program, written in Python, which computed the constant current feedback-loop for the Z(V) curves. Also hybrid codes were developed in a variety of programming languages, mainly C, FORTRAN and Python, in order to fit all the computing pieces together in an integrated executable program.

1D, 2D and 3D plots were produced using xmgrace, gnuplot and MayaVi, and also some wave packet propagation animations were produced for demonstration purposes.

Part III: Laser induced electron emission in metals

This Part represents a natural bridge between Parts I and II. While developing the numerical techniques for the TDSE related problems appearing in Part II, a model for the study of the electron emission induced by laser pulses in metals was proposed. The problem presented a mixture of the already treated subject of electron emission from surfaces in Part I, and the TDSE and wave function time evolution in metals being developed in Part II. This represented a good opportunity to merge part of the techniques developed for previous, different works in a single contribution.

The idea is, as in Part II, to obtain information about the electron dynamics at metal surfaces, but this time studying the photoelectron emission induced by short laser pulses. As an ultra-short laser pulse grazingly impinges on a metal surface, the rearrangement of the metal valence band electrons due to the pulse electromagnetic field produces itself an induced potential. For frequencies higher than the surface plasmon frequency the surface electrons are not able to respond to the laser field fast enough and thus the induced potential is not expected to play a role in the electron emission process. On the other hand, when the pulse frequency is around or below the surface plasmon frequency, surface electrons can "follow" the fluctuations of the laser field and the generated field by this electron rearrangement is expected to be of the order of that of the laser. Under this conditions, the induced potential can no longer be neglected a priori, as its effect can be relevant on the electron emission yield.

In this Part we calculate the electron emission probability from the valence band of an Al surface under different laser pulse frequencies and

durations, analyzing in detail the effect of the induced potential on the electron distribution.

For the system potentials we use a jellium model for the surface and, as the laser incidence is almost parallel to the surface, we model it as a time-dependent uniform electric field perpendicular to the surface, i.e. along the z axis. The laser field modulation is represented by a sinusoidal pulse with a determined duration, given by a $\sin^2$ half cycle envelope.

Regarding the induced potential, by using the linear response theory we obtain the response function of the system to the laser pulse [48], which in turn allows us to compute the induced electronic density which, finally, permits us to derive the induced potential itself.

To calculate the total electron emission from the surface we compute the electron emission differential probability by means of the transition matrix for electrons going from an initial state in the metal valence band to a final continuum state above the vacuum level, due to the influence of the laser electric field. For the transition matrix calculation we use two different models, both accounting for the induced potential, and a third one derived in a previous work, in which the surface response is not considered.

For the first model we use the *Surface Jellium–Volkov* (SJV) approximation [49], a time-dependent distorted wave method which describes the interaction of the surface electrons with the laser field and the induced field.

For the second model, based on solving the *Time Dependent Schrödinger Equation* (TDSE), we use a one-dimensional slab for the surface potential, from which we obtain the initial electronic states as the discretized eigenstates of the potential. The time evolution of these eigenstates under the laser pulse is then driven by the one-dimensional time-depend Schrödinger equation. The TDSE with the time dependent potentials is then numerically solved [50] and the transition amplitudes are obtained. The time evolution calculation starts as the laser pulse is "switched on" and is considered finished when the induced potential decays two orders of magnitude from its value at the moment the laser pulse ends.

Results are also obtained from a third model, developed in a previous work [51], based in the Impulsive Jellium–Volkov approximation and which does not account for the dynamic response of the surface, in order to study the influence of the induced potential on the system.

For this work, part of the numerical codes developed for Part II where used and adapted for the TDSE calculations. Calculations themselves were carried out in the DIPC HPC computing facilities. Regarding the response calculations, new codes where developed in order to derive the response potential from the response function. Also, a visualization program was developed in order to better understanding the surface response under different parameters of the laser pulse. Again, essentially Open Source / Free software was use for all the computing related tasks.

References

[1] K. Kimura, M. Tsuji, M. hiko Mannami, Phys. Rev. A **46 (5)** 2618 (1992).

[2] E. Sanchez, O. Grizzi, G. Nadal, G. Gómez, M. Martiarena, V. Ponce, Nucl. Instrum. Methods Phys. Res. **B90** 261 (1994) .

[3] M. Martiarena, E. Sánchez, O. Grizzi, V. Ponce, Phys. Rev. A **53 (2)** 895 (1996).

[4] K. Kimura, G. Andou, K. Nakajima, Nucl. Instrum. Methods Phys. Res. B **164-165** 933 (2000).

[5] H. Winter, Physics Reports **367** 387 (2002).

[6] J. Briggs, F. Drepper, J. Phys. B **23 (23)** 4033 (1978).

[7] Y. T. Lee, J. C. Chen, Phys. Rev. A **19 (2)** 526 (1979).

[8] V. Ponce, R. Baragiola, J. Phys. B **17** 2467 (1984).

[9] K.O. Groeneveld, W. Meckbach, I.A. Sellin and J. BurgdÃ¶rfer, Comments At. Mol. Phys. **187** (1984).

[10] J. Burgdörfer, M. Breining, S.B. Elston and I.A. Sellin, Phys. Rev. A **28**, 3277 (1983).

[11] A. Zunger and A. J. Freeman, Phys. Rev. B **16**, 2901 (1977).

[12] M. S. Gravielle, Phys. Rev. A **62**, 062903 (2000).

[13] M. L. Martiarena, V. H. Ponce, Nucl. Instrum. Methods Phys. Res. B **203** (2003) 62.

[14] L. Landau, E. Lifschitz, Quantum Mechanics, Pergamon, Oxford, 1977.

[15] M.R.C. Mc Dowell and J.P. Coleman, Introduction to the theory of ion-atom collisions (North-Holland, Amsterdam, 1970).

[16] J.H. Hubbell et al., J. Phys. Chem. Ref. Data **3**, 471 (1975).

[17] J. Ziegler, J. Biersack, U. Littmark, The Stopping and Range of Ions in Matter, Vol. 1, Pergamon, New York, 1985.

[18] P. Fainstein, V. Ponce, R. Rivarola, J. Phys. B **22** 1207 (1989).

[19] P. Fainstein, V. Ponce, R. Rivarola, J. Phys. B **24** 3091 (1991).

[20] M. Gravielle, J. Miraglia, Phys. Rev. A **44** 7299 (1991).

[21] M. Gravielle, J. Miraglia, Phys. Rev. A **51** 2131 (1995).

[22] M. Galassi et al, GNU Scientific Library Reference Manual (3rd Ed.), ISBN 0954612078.

[23] M. F. Crommie, C. P. Lutz, and D. M. Eigler, Nature **363**, 524 (1993).

[24] Y. Hasegawa and Ph. Avouris, Phys. Rev. Lett. **71**, 1071 (1993).

[25] Ph. Hofmann, B. G. Briner, M. Doering, H.-P. Rust, E. W. Plummer, and A. M. Bradshaw , Phys. Rev. Lett. **79**, 265 (1997).

[26] L. Petersen, P. T. Sprunger, Ph. Hofmann, E. Lægsgaard, B. G. Briner, M. Doering, H.-P. Rust, A. M. Bradshaw, F. Besenbacher, and E. W. Plumer, Phys. Rev. B **57**, R6858 (1998).

[27] J. I. Pascual, A. Dick, M. Hansmann, H.-P. Rust, J. Neugebauer, and K. Horn, Phys. Rev. Lett. **96**, 046801 (2006).

[28] L. Limot, T. Maroutian, P. Johansson, and R. Berndt, Phys. Rev. Lett. **91**, 196801 (2003).

[29] G. Binnig, K. H. Frank, H. Fuchs, N. Garcia, B. Reihl, H. Rohrer, F. Salvan, and A. R. Williams, Phys. Rev. Lett. **55**, 991 (1985).

[30] R. S. Becker, J. A. Golovchenko, and B. S. Swartzentruber, Phys. Rev. Lett. **55**, 987 (1985).

[31] T. Jung, Y.W. Mo, and F.J. Himpsel, , Phys. Rev. Lett. **74**, 1641-1644 (1995).

[32] M. Pivetta, F. Patthey, M. Stengel, A. Baldereschi, and W.-D. Schneider, Phys. Rev. B **72**, 115404-1-6 (2005).

[33] Hans-Christoph Ploigt, Christophe Brun, Marina Pivetta, François Patthey, and Wolf-Dieter Schneider, Phys. Rev. B **76**, 195404-1-5 (2007).

[34] C. L. Lin, S. M. Lu, W. B. Su, H. T. Shih, B. F. Wu, Y. D. Yao, C. S. Chang, and Tien T. Tsong, Phys. Rev. Lett. **99**, 216103 (2007).

[35] P. Ruffieux, K. Aït-Mansour, A. Bendounan, R. Fasel, L. Patthey, P. Gröning, and O. Gröning, Phys. Rev. Lett. **102**, 086807 (2009).

[36] E. V. Chulkov, V. M. Silkin, and P. M. Echenique, Surf. Sci. **437**, 330 (1999).

[37] J. B. Pendry, Low Energy Electron Difraction, (Academic Press, London, 1974).

[38] R. García, J. J. Sáenz, J. M. Soler and N. García , Surf. Sci. **181**, 69 (1986).

[39] T. Hakala, M. J. Puska, A. G. Borisov, V. M. Silkin, N. Zabala, and E. V. Chulkov, Phys. Rev. B **75**, 165419 (2007).

[40] A. G. Borisov, T. Hakala, M. J. Puska, V. M. Silkin, N. Zabala, and E. V. Chulkov, P. M. Echenique, Phys. Rev. B **76**, 121402(R) (2007).

[41] J. M. Pitarke, F. Flores, and P. M. Echenique, Surf. Sci. **234**, 1 (1990).

[42] J. I. Pascual, C. Corriol, G. Ceballos, I. Aldazabal, H.-P. Rust, K. Horn, J. M. Pitarke, P. M. Echenique, and A. Arnau,, Phys. Rev. B**75** 165326 (2007).

[43] A. G. Borisov, A. K. Kazansky, and J. P. Gauyacq, Phys. Rev. Lett. **80**, 1996 (1998); Phys. Rev. B **59**, 10 935 (1999); Surf. Sci. **430**, 165 (1999).

[44] E. V. Chulkov, A. G. Borisov, J. P. Gauyacq, D. Sánchez-Portal, V. M. Silkin, V. P. Zhukov, and P. M. Echenique, Chem. Rev. **106**, 4160 (2006).

[45] M. D. Feit, J. A. Fleck Jr., A. Steiger, J. Comput. Phys. **47**, 412 (1982).

[46] C. Leforestier, R. H. Bisseling, C. Cerjan, M. D. Feit, R. Friesner, A. Guldberg, A. Hammerich, G. Jolicard, W. Karrlein, H. D. Meyer, N. Lipkin, O. Roncero, R. Kosloff, J. Comput. Phys. **94**, 59 (1991).

[47] J. Sjakste, A. G. Borisov, J. P. Gauyacq, and A. K. Kazansky, J. Phys. B: At. Mol. Opt. Phys. **37**, 1593 (2004).

[48] M. Alducin, V. M. Silkin, J.I. Juaristi and E. V. Chulkov, Phys. Rev A **67**, 032903 (2003).

[49] M. S. Gravielle, Phys. Rev. A **58**, 4622 (1998).

[50] W. H. Press, S. A. Teukolsky, W.T. Vetterling and B.P. Flannery, *Numerical Recipes* (Cambridge University Press, New York, 1992).

[51] M. N. Faraggi, M. S. Gravielle and D. M. Mitnik, Phys. Rev. A **76**, 012903 (2007).

Part I

Electron emission in grazing collisions of protons with insulator surfaces

Chapter 1

Grazing incidence collisions of fast protons with insulators: electron emission around the convoy peak

Published as I. Aldazabal, V.H. Ponce and A. Arnau in phys. stat. sol. (b) **241** (10), 2374 (2004).

Abstract

A general model to calculate electron spectra in grazing incidence ion-surface collisions is presented. It is based on the use of atomic form factors for projectile ionization and incoherent scattering functions for the target. The model is applicable for arbitrary systems whose electrons can be described by localized atomic orbitals, like ionic crystals. For 100 keV protons on LiF surfaces we find that the projectile electron contribution to the convoy peak is larger than the contribution from target ionization.

PACS 34.50.Dy, 34.50. Fa, 79.20.Rf, 78.90.+t

DOI: 110.1002/pssb.200404881

1.1 Introduction

Electron spectra produced in ion-surface collisions give information about the electronic structure of the target and projectile electrons, as well as on the interaction process itself. Most of the electrons that are detected are low energy electrons. The shape of the electron spectra in the low energy region reflects the structure of the density of final states, the target electronic structure and the residual interaction charges of the combined projectile-target system. This latter means, for example, that there is a significant difference between ionization of neutral atoms or negative ions due to the presence or absence of residual charges of the target in the final state. However, in the high energy part of the spectra two different structures appear, convoy and binary peak electrons, that are not so much influenced by the details of the target electronic structure. These two structures are well known in atomic collision physics. In particular, the structure of the convoy electrons spectra around a sharp cusp has been widely studied in the past 25 years [1.1–1.3]. In the case of solid targets, both transmission and grazing incidence experiments have been done using different kind of targets [1.4–1.8]. In solids, the electron spectra around the convoy peak are much wider and sometimes shifted with respect to the pure cusp value at the relative velocity of the collision due to a number of effects: elastic and inelastic scattering of electrons with the target, screening by other electrons, polarization forces of different origin, like image forces, and track potential induced forces. In this work we focus on the production of convoy electrons in grazing incidence collisions of fast protons with insulating surfaces. In particular we consider LiF surface as a model insulator that has been also used in the experiments [1.9, 1.10]. More precisely, we consider the contribution to the convoy electron peak from projectile ionization, or electron loss to the continuum (ELC). The other contribution due to target ionization, or electron capture to the continuum (ECC), has been considered by Gravielle et al. [1.11]. The inclusion of charge states in the beam will be considered elsewhere [1.12].

1.2 Theoretical model

Our way to model the target surface electrons is very simple: they are considered to be localized in atomic orbitals [1.13] at the anion site. In

this way, i.e., binary collision approximation, we neglect collective effects, like plasmon excitations, which are not expected to play an important role in neutral atom scattering on surfaces. The initial and final projectile electron states are hydrogenic orbitals [1.14]. The interaction of the hydrogen projectile with the target surface is described as follows:

(i) we calculate the doubly differential ionization cross section (DDCS) of H by fast electrons at different impact parameters in first Born approximation [1.15]. The impact parameter dependent transition amplitude from initial state $\left|\psi_0^H\right\rangle$ to final state $\left|\psi_k^H\right\rangle$ is given by [atomic units are used in this paper except where explicitly stated]:

$$a_{0k}(\vec{\rho}) = \left(\frac{-i}{\pi v}\right) \int \frac{d^2\vec{Q}\exp(-i\vec{Q}\cdot\vec{\rho})}{Q^2 + (\Delta E_{0k}/v)^2} F_{0k}(\vec{q}), \tag{1.1}$$

where

$$\begin{aligned} q^2 &= Q^2 + (\Delta E_{0k}/v)^2 \\ \Delta E_{0k} &= \frac{k^2}{2} + \frac{1}{2} \\ F_{0k}(\vec{q}) &= \left\langle \psi_k^H \right| \exp(i\vec{q}\cdot\vec{r}) \left|\psi_0^H\right\rangle \end{aligned}$$

(ii) we perform a Galilean shift of the frame of reference from the projectile to the laboratory system: $\vec{k'} = \vec{k} + \vec{v}$, where $\vec{k'}$ and $\vec{k}$ refer to the final state electron momentum in the laboratory and projectile system, respectively, and $\vec{v}$ denotes the collision velocity. In this description the low energy electrons in all directions in the projectile frame are electrons with energies around the cusp peak in the forward direction in the laboratory frame.

(iii) we include a momentum distribution for the F electrons of the target by using the incoherent scattering function $S(\vec{q})$ that accounts for the target electronic structure and its excitations [1.16]. In this case the transition amplitude from initial state $\left|\psi_0^H\right\rangle \left|\psi_i^F\right\rangle$ to final state $\left|\psi_k^H\right\rangle \left|\psi_f^F\right\rangle$ is given by:

$$a_{0k}^{if}(\vec{\rho}) = \left(\frac{-i}{\pi v}\right) \int \frac{d^2\vec{Q}\,\exp(-i\vec{Q}\cdot\vec{\rho})}{Q^2 + \left(\Delta E_{0k}^{if}/v\right)^2} F_{0k}(\vec{q}) G_{if}(\vec{q}) \tag{1.2}$$

where

$$G_{if}(\vec{q}) = \sum_{j=1}^{Z_T} \left\langle \psi_f^F \right| \exp(-i\vec{q}\vec{r_j}) \left| \psi_i^F \right\rangle$$
$$\Delta E_{0k}^{if} = \Delta E_{0k} + \Delta E_{if}^F$$

Z_T is the number of target electrons and ΔE_{if}^F is the target electron transition energy. If we neglect the final state energy dependence of the denominator in Eq.(2), i.e., $\Delta E_{0k}^{if} \simeq \Delta E_{0k} + \left\langle \Delta E^F \right\rangle$, and invoke closure relation [1.17] we can use the incoherent scattering function of the target atom $S(\vec{q})$ to calculate the DDCS and approximate $\sum_f \left| a_{0k}^{if}(\vec{\rho}) \right|^2$ by $\left| \left\langle a_{0k}^F(\vec{\rho}) \right\rangle \right|^2$, where $\left\langle a_{0k}^F(\vec{\rho}) \right\rangle$ and $S(\vec{q})$ are given by:

$$\left\langle a_{0k}^F(\vec{\rho}) \right\rangle = \left(\frac{-i}{\pi v} \right) \int \frac{d^2\vec{Q} \exp(-i\vec{Q}\cdot\vec{\rho})}{Q^2 + \left(\Delta E_{0k}^{if}/v \right)^2} F_{ok}(\vec{q}) \sqrt{S(\vec{q})} \qquad (1.3)$$

$$S(\vec{q}) = \sum_{f \neq i} |G_{if}(\vec{q})|^2 \qquad (1.4)$$

The inclusion of the target form factors allows to consider arbitrary targets other than LiF, as long as they can be approximated by atomic orbitals.

(iv) We use a planar potential approach to describe the ion trajectory in grazing collisions and define a probability of ionization to a given final state per unit surface area from the probability of ionization per atom multiplied by the surface atomic density. In this way we approximate the square array of atoms at the surface by a continuum that allows to calculate the probability of ionization per unit path length (X-direction) by integration along the Y-direction (see reference [1.18] for details). Finally, integration along the trajectory gives the electron spectra. Other effects like inelastic and elastic scattering of electrons at the surface, i.e., transport, are not considered. Our aim is to focus on the high energy convoy electron peak, which are those less affected by transport and post-collisional effects.

1.3 Results

In Fig. 1.1 we show the impact parameter dependent doubly differential cross section for ionization of hydrogen by electron impact at a collision velocity $v = 2$ in the low energy range (0 to 20 eV) and in the forward direction (0 degrees) at three different impact parameters. At large impact parameters the DDCS is rather small, as the probability of ionization decays almost exponentially with impact parameter. The DDCS at fixed impact parameter is rather smooth as a function of final electron energy, showing a typical behaviour well-known in atomic physics [1.19]. In the energy range [0 eV, 20 eV] the DDCS decreases about an order of magnitude.

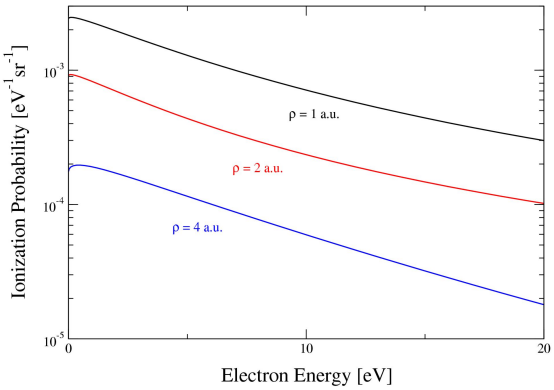

Figure 1.1: Doubly differential cross section for ionization of H by fast electrons ($v = 2a.u.$) as a function of final electron energy at different impact parameters and in the forward direction.

These low energy electrons in the projectile frame are transformed into forwardly emitted electrons in the laboratory frame around $\vec{k} = \vec{v}$, i.e., the convoy peak. In Fig. 1.2 we show the DDCS in the laboratory frame for hydrogen-electron collisions. A typical symmetric structure centred at the relative velocity appears similar to the ELC peaks found in atomic collisions. In the laboratory frame the DDCS are much higher than in the projectile frame as all the emitted low energy electrons in the whole solid angle are now focused in a narrow cone around the forward direction. After integration over all final states the total number of ionized electrons is, of course, the same in the two frames.

The inclusion of the momentum distribution of the target F electrons via the use of the incoherent scattering function described above enhances

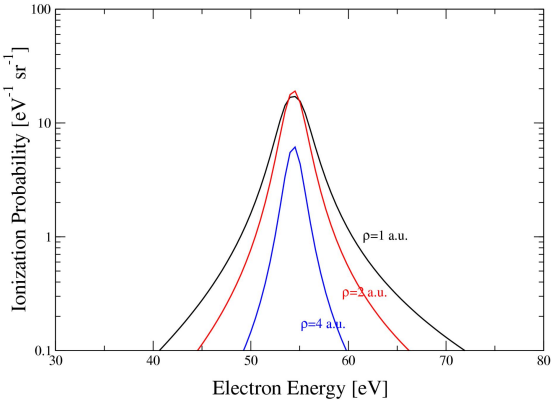

Figure 1.2: Same as Fig. 1.1 but in the laboratory frame and emission angle 0.7 degrees.

the value of the DDCS as compared to the free electron case by a factor of around 3 at small impact parameters and much smaller (1-2) at large impact parameters. This can be seen in Fig. 1.3, where we plot the DDCS for H-F collisions.

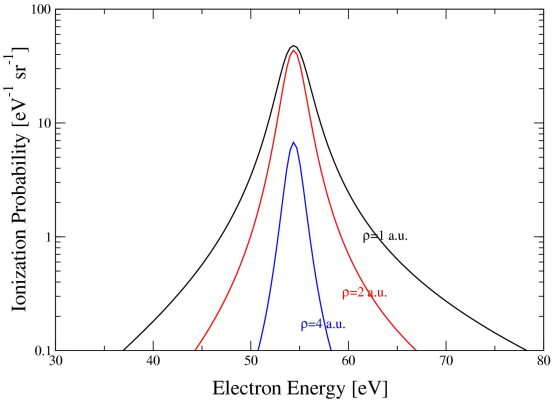

Figure 1.3: Same as Fig. 1.2 but including the incoherent scattering function of the F anion.

In order to compare with any experimental spectra it is necessary to integrate along the ion trajectory and have some knowledge about the capture and loss cross sections that will determine the ion fractions. In Fig. 1.4 we show the total electron emission probability from ELC at three different emission angles. It is interesting to note that the convoy peak broadens and shows a maximum at lower values of the electron energy as

the emission angle increases, as measured in the experiments [1.20]. A comparison of ELC and ECC [1.11] contributions at 0.7 degrees emission angle is shown in Fig. 1.5. The ELC contribution is about an order of magnitude larger. However, inclusion of charge states would reduce significantly this difference giving similar contributions from ELC and ECC, except at the peak position. This estimate is based on the fact that capture cross sections are about ten times lower than loss cross sections and, therefore, the fraction of protons in the beam is expected to be about ten times larger than that of neutral hydrogen.

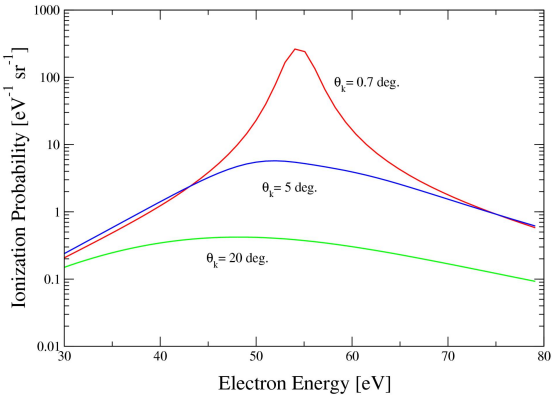

Figure 1.4: Total electron emission probability from projectile ionization (ELC) as a function of final electron energy at three different emission angles.

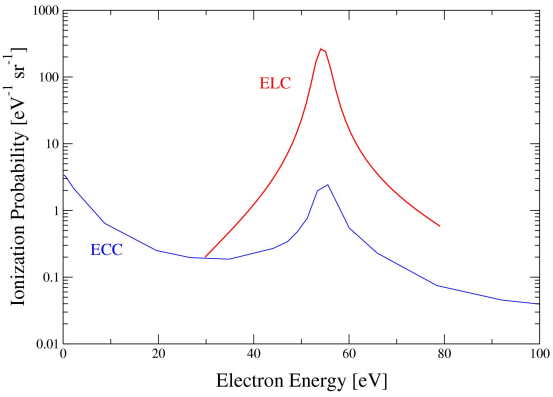

Figure 1.5: Total electron emission probability from projectile ionization (ELC) and target ionization (ECC) as a function of final electron energy. The angle of emission is 0.7 degrees.

1.4 Conclusion

Our model allows to study electron emission from arbitrary surfaces by fast proton impact at grazing incidence, as long as the target electron states can be described by localized atomic orbitals, by using the proper form factor. The convoy electron spectra that we calculate show the correct qualitative behavior as a function of electron emission angle. The contribution of ELC to the convoy electron peak is larger than the ECC contribution for 100 keV protons on LiF surfaces. The inclusion of the charge state population of protons and hydrogen atoms in the beam would reduce significantly the difference between the ELC and ECC contributions.

1.5 Acknowledgements

We thank M.S. Gravielle, J.E. Miraglia, M.L. Martiarena and E.A. Sanchez for helpful discussions. We gratefully acknowledge financial support by Eusko Jaurlaritza, Euskal Herriko Unibertsitatia, Donostia International Physics Center and the Spanish M.C.Y.T. (under contract BFM2001-0076).

1.6 References

[1.1] K.O. Groeneveld, W. Meckbach, I.A. Sellin and J. Burgdörfer, Comments At. Mol. Phys. **4**, 187 (1984).

[1.2] J. Burgdörfer, M. Breining, S.B. Elston and I.A. Sellin, Phys. Rev. **A28**, 3277 (1983).

[1.3] J.S. Briggs and F. Drepper, J. Phys. **B23**, 4033 (1978).

[1.4] L.F. de Ferraris and R.A. Baragiola, Phys. Rev. **A33**, 4449 (1986).

[1.5] H. Winter, P. Strohmeier and J. Burgdörfer, Phys. Rev. **A39**, 3895 (1989).

[1.6] K. Kimura, M. Tsuji and M. Mannami, Nucl. Instrum. Methods **B79**, 33 (1993).

[1.7] G. Xiao et al., Phys. Rev. Lett. **79**, 1821 (1997).

[1.8] E.A. Sanchez, O. Grizzi, M.L. Martiarena and V.H. Ponce, Phys. Rev. Lett. **71**, 801 (1993).

[1.9] G.R. Gomez, O. Grizzi, E.A. Sanchez and V.H. Ponce, Phys. Rev. **B58**, 7403 (1998).

[1.10] K. Kimura, G. Andou and K. Nakajima, Nucl. Instrum. Methods **B164/165**, 933 (2000).

[1.11] M.S. Gravielle and J.E. Miraglia, Phys. Rev. **A67**, 04291 (2003).

[1.12] I. Aldazabal, M.S. Gravielle, J.E. Miraglia, V.H. Ponce and A. Arnau (to be published)[1]

[1.13] E. Clementti and C. Roetti, Atomic Data and Nuclear Data Tables **14**, 177 (1974).

[1.14] L.D. Landau and E.M. Lifschitz, Quantum Mechanics (Pergamon, Oxford, 1977).

[1.15] M.R.C. Mc Dowell and J.P. Coleman, Introduction to the theory of ion-atom collisions (North-Holland, Amsterdam, 1970).

[1.16] J.H. Hubbell et al., J. Phys. Chem. Ref. Data **3**, 471 (1975).

[1.17] V.H. Ponce and R.A. Baragiola, J. Phys. **B17**, 2467 (1984).

[1.18] A. Arnau, M.S. Gravielle, J.E. Miraglia and V.H. Ponce, Phys. Rev. **A67**, 062902 (2003).

[1.19] P.D. Fainstein, L. Gulyás and A. Salin, J. Phys. **B29**, 1225 (1996).

[1.20] E.A. Sanchez et al., Nucl. Instrum. Methods **B90**, 261 (1994).

[1]Later published as I. Aldazabal, M.S. Gravielle, J.E. Miraglia, A. Arnau and V.H. Ponce, *Nucl. Instr. and Meth. in Phys. Res. B **232**, 53 (2005). doi: 10.1016/j.nimb.2005.03.024*, and included as Chapter 2 of this manuscript.

Chapter 2

Role of projectile charge state in convoy electron emission by fast protons colliding with LiF(001)

Published as I.Aldazabal, M.S. Gravielle, J.E. Miraglia, A. Arnau and V.H. Ponce in Nucl. Instr. and Meth. in Phys. Res. B **232**, 53 (2005).

Abstract

Target ionization and projectile ionization differential cross sections are used to calculate the electron emission spectra by fast proton impact on ionic crystal surfaces under grazing incidence conditions. Both bare protons and neutral hydrogen species are considered. We use a planar potential approach to determine the projectile trajectory that later on allows us to calculate the charge state fractions. We show that, although the fraction of protons is significantly higher, the contribution from neutral hydrogen ionization has to be considered. The energy and angular dependence of the spectra is analyzed.

PACS: 34.50.Dy, 34.50.Fa, 79.20.Hx, 79.20.Rf, 34.20.-b

DOI: 10.1016/j.nimb.2005.03.024

2.1 Introduction

The spectrum of electrons emitted in ion surface collision gives information about the electronic and atomic structure of the surface topmost atomic layer and has lately been object of study [2.1–2.5]. At high emission energies two structures appear, the so called *convoy* and *binary* peaks, already known from atomic collisions [2.6–2.8].

We study the projectile (*electron loss to the continuum* or *ELC*) and surface (*electron capture to the continuum* or *ECC*) electron contributions to the convoy peak. Low energy electrons emitted in all directions from projectile ionization are expected to play a role comparable to high energy forwardly emitted electrons from target ionization.

The projectile trajectory is treated classically and for the electron emission we use a binary collision model within the impact parameter formalism [2.9–2.11] in first Born approximation for ELC electrons [2.12, 2.13] and the continuum-distorted-wave-eikonal-initial-state (CDW-EIS) approximation for ECC electrons [2.14–2.16].

2.2 Theoretical Model

We consider a heavy projectile P of charge q and mass M_p in grazing incidence on a surface with a velocity $\vec{v} = (v_s, v_z)$, v_s and v_z being the velocity components parallel and perpendicular to the surface, respectively. The triple differential cross section (TDCS) for electron emission is obtained considering binary collisions between the projectile and the surface atoms. The surface is thus treated as a collection of atoms, each of them contributing in its own to the total emission cross section.

Being a grazing collision, we can approximate the trajectory as a succession of differential trajectories Δx in which the projectile velocity component perpendicular to the surface is considered negligible, i.e. the projectile moves at a constant distance from the surface $z(x)$ (see Fig. 2.1).

Under these assumptions we can study the collision with the straight-line version of the impact parameter approximation to get both the projectile and surface ionization cross sections.

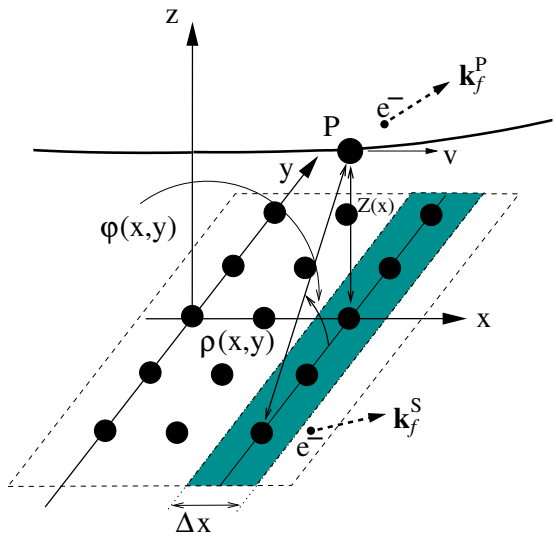

Figure 2.1: Collision scheme.

Since target electrons are localized around atoms, only electrons of atoms situated in the top most layer contribute effectively to the electron emission proccess.

Then for a given height z over the surface, the emission probability per unit path length for the transition from the initial state i to the final state f with momentum $\vec{k}$ is given by [2.16] (atomic units are used in this paper unless otherwise stated):

$$\frac{dP_i^{(\mathrm{m})}(\vec{k}, z(x))}{d\vec{k}dx} = \delta_S \int_{-\infty}^{+\infty} dy \; P_{i\,\vec{k}}^{(\mathrm{m})(\mathrm{at})}(\vec{\rho}(x,y)), \tag{2.1}$$

where we denote with the upper index $m = P, S$ the electrons ionized from the projectile and from the surface, respectively, $P_{i\,\vec{k}}^{(\mathrm{m})(\mathrm{at})}(\vec{\rho})$ is the probability of atomic ionization depending on the impact-parameter $\vec{\rho}$ and δ_S is the surface atomic density which is considered as constant.

Thus, to obtain the final TDCS we first compute the ionization probability for both the projectile and the surface electrons for a given final state and then we integrate them over the classical trajectory taking into account the charge state of the projectile.

2.2.1 Projectile Electrons

We assume that the projectile collides with the localized surface electrons. The differential cross section for H ionization by fast electrons in the projectile frame of reference is calculated in the impact parameter first Born approximation, being later referred to the laboratory system [2.6, 2.17]. The hydrogenic electrons go from the Hydrogen fundamental state $|0\rangle$ to a Hydrogen continuum state with momentum $\vec{k}$ [2.13] and the surface electrons go from an initial state $|i\rangle$ to a final state $|f\rangle$. The transition amplitude for the binary collision under this assumptions is [2.11]:

$$A_{0\vec{k}}^{if}(\vec{\rho}) = \left(\frac{-i}{\pi v}\right) \int \frac{d\vec{\eta}\, \exp(-i\vec{\eta}\cdot\vec{\rho})}{\eta^2 + \left(\Delta E_{0k}^{if}/v\right)} F_{0\vec{k}}(\vec{q}) G_{if}(\vec{q}) \tag{2.2}$$

where $\vec{\rho}$ is the collision impact parameter, $\vec{\eta}$ is the component of the transferred momentum $\vec{q}$ perpendicular to $\vec{v}_s$, ΔE_{0k}^{if} is the target electron transition energy and $F_{0\vec{k}}(\vec{q})$ and $G_{if}(\vec{q})$ are respectively the projectile and the target form factors [2.17].

Using closure approximation [2.7, 2.8] we can take $\sum_f \left|A_{0\vec{k}}^{if}(\vec{\rho})\right|^2$ by $\left|\left\langle A_{0\vec{k}}(\vec{\rho})\right\rangle\right|^2$ and the target transition energy as:

$$\Delta E_{0k}^{if} \cong k^2/2 + 1/2 + q^2/2S(\vec{q}) \tag{2.3}$$

where $S(q)$ is the incoherent scattering function of the target atom [2.18].

Thus, for the transition probability of a projectile electron we have the expression:

$$P_{0\vec{k}}^{(\mathrm{P})(\mathrm{at})}(\vec{\rho}) = \left|\left\langle A_{0\vec{k}}(\vec{\rho})\right\rangle\right|^2$$
$$= \left| \left(\frac{-i}{\pi v}\right) \int \frac{d\vec{\eta}\, \exp(-i\vec{\eta}\cdot\vec{\rho})}{\eta^2 + \left(\Delta E_{0k}^{if}/v\right)} F_{0\vec{k}}(\vec{q}) \sqrt{S(\vec{q})} \right|^2 . \tag{2.4}$$

2.2.2 Surface Electrons

To obtain the surface electron contribution we employ the CDW - EIS approximation to evaluate the atomic probabilities $P_{i\ \vec{k}_f}^{(\mathrm{S})(\mathrm{at})}(\vec{\rho})$. The CDW-EIS T-matrix element reads:

$$T_{i\vec{k}_f}^{\mathrm{CDW-EIS}} = \left\langle \chi_f^{\ \mathrm{CDW}} | W_f^{\dagger} | \chi_i^{\ \mathrm{E}} \right\rangle , \tag{2.5}$$

where χ_f^{CDW} is the final CDW wave function, which contains a product of two continuum states, one around the target and the other around the projectile, χ_i^{E} is the eikonal wave function, and W_f is the final perturbative potential. In the CDW-EIS approximation the T-matrix element has a closed expression [2.14], and the atomic probability can be derived from Eq (2.5) by using the well-known eikonal transformation $P_{i\vec{k}_f}^{(\mathrm{S})(\mathrm{at})}(\vec{\rho}) = \left| A_{i\vec{k}_f}^{\mathrm{CDW-EIS}}(\vec{\rho}) \right|^2$ [2.11], where

$$A_{i\vec{k}_f}^{\mathrm{CDW-EIS}}(\vec{\rho}) = \frac{2\pi}{v_s} \int d\vec{\eta}\; T_{i\vec{k}_f}^{\mathrm{CDW-EIS}} \exp(i\vec{\eta}.\vec{\rho}) \tag{2.6}$$

is the CDW-EIS transition amplitude.

2.2.3 Projectile Charge State

We are also interested in the projectile charge state, i.e. the projectile probability of being in either the ionized or the neutral state as a function of the height over the surface, $\phi_+(z)$ and $\phi_0(z)$ respectively.

In order to compute these we need to know, as a function of the height and per unit path, the probability of *i*) the projectile being ionized from its neutral state, $P_{\mathrm{loss}}(z)$, and *ii*) the projectile being neutralized from its ionized state, $P_{\mathrm{capt}}(z)$.

$P_{\mathrm{loss}}(z)$ is obtained just integrating the transition probability as a function of the impact parameter first over the strip normal to the projectile speed (Eq. 2.1) and then over the ionized electron final momentum $\vec{k}$:

$$P_{\mathrm{loss}}(z) = \int d\vec{k}\; \delta_S \int_{-\infty}^{+\infty} dy\; P_{0\vec{k}}^{(\mathrm{P})(\mathrm{at})}(\vec{\rho}(x,y)). \tag{2.7}$$

To evaluate $P_{\mathrm{capt}}(z)$ we employ the prior version of the eikonal-impulse approximation, which is a distorted wave method making use of the exact impulse and eikonal wave functions in the final and initial channels respectively [2.19, 2.20].

Fig. 2.2 shows the results obtained for a LiF surface (see section 2.3 for a complete description of the system). The projectile loss probability is, for every distance to the surface, at least one order or magnitude greater than the capture probability. Accordingly we will find that the projectile is in its ionized state along most of the collision path.

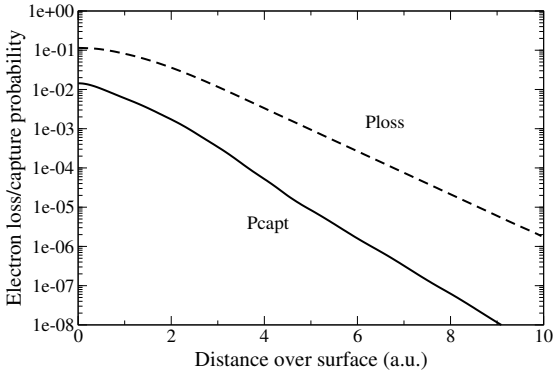

Figure 2.2: $P_{\rm loss}$ and $P_{\rm capt}$ for LiF surface.

To account for the projectile trajectory we use the relation $dx/dz = v_s/v_z(z)$:

$$\frac{dP_{if}}{dz} = \frac{v_s}{v_z(z)} \frac{dP_{if}}{dx}. \tag{2.8}$$

with $z(x)$ being the parametrized trajectory, obtained assuming a ZBL [2.21] planar potential for the surface-proton interaction.

The probabilities for the projectile to be in its neutral or ionized states are given by the set of differential equations

$$\begin{aligned} \frac{d\phi_+(z)}{dz} &= \phi_0(z)\frac{v_s}{v_z(z)}P_{\rm loss}(z) \\ &- \phi_+(z)\frac{v_s}{v_z(z)}P_{\rm capt}(z) \end{aligned} \tag{2.9}$$

and

$$\begin{aligned} \frac{d\phi_0(z)}{dz} &= \phi_+(z)\frac{v_s}{v_z(z)}P_{\rm capt}(z) \\ &- \phi_0(z)\frac{v_s}{v_z(z)}P_{\rm loss}(z) \end{aligned} \tag{2.10}$$

where both probabilities satisfy the equation

$$\phi_0(z) + \phi_+(z) = 1. \tag{2.11}$$

and the boundary condition is $\phi_0(-\infty) = 0$ as the surface is impinged with a proton beam.

In Fig. 2.3 we can see that up to 5 a.u. from the surface the projectile maintains its initial ionized state from where it gets a higher chance of

being in the neutral state up to a maximum probability of about 9% at the trajectory turning point at 0.54 a.u.

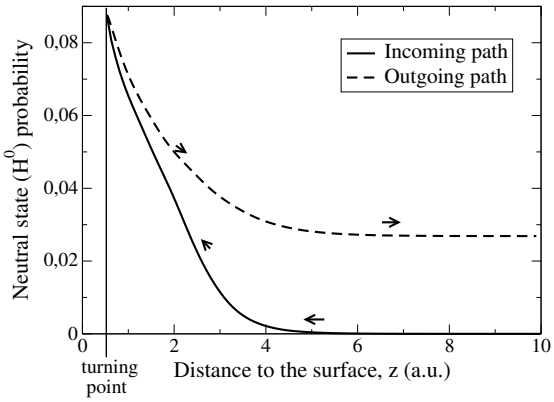

Figure 2.3: Probability of the projectile being in the neutral state as a function of the height over the LiF surface.

2.2.4 Final Emission

For a given height over the surface and a final electron momentum, we compute both the surface and projectile emission probabilities and the charge state for the projectile. By weighting the former with the latter we obtain the electron emission probability

$$\begin{aligned} \frac{dP^4(\vec{k}_f,z)}{d\vec{k}dz} &= \phi_0(z)\frac{v_s}{v_z(z)}\frac{dP_i^{(\mathrm{P})}(\vec{k}_f,z)}{d\vec{k}dx} \\ &+ \phi_+(z)\frac{v_s}{v_z(z)}\frac{dP_i^{(\mathrm{S})}(\vec{k}_f,z)}{d\vec{k}dx} \end{aligned} \tag{2.12}$$

Integrating over the projectile trajectory we obtain the triple differential cross section for the electron emission

$$\frac{d^3P(\vec{k}_f)}{d\vec{k}} = \int_{z\in trajectory} dz \frac{d^4P(\vec{k}_f,z)}{d\vec{k}dz} \tag{2.13}$$

2.3 Results

The system considered consists of a proton moving with an initial trajectory of 0.7° against a LiF(001) surface. The proton velocity is 2 atomic

units and the trajectory it follows is given by a ZBL surface-proton planar potential.

For this system we compute the electron emission cross section for different polar angles in the scattering plane as a function of the emitted electron energy, the polar angle being referred to the surface. The results obtained for polar angles of 0.7, 5.0, 10.0 and 20.0 degrees are shown in Fig. 2.4.

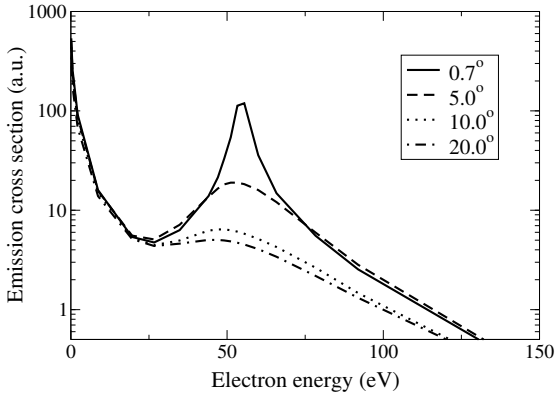

Figure 2.4: Electron emission cross section for different polar angles.

As we increase the polar angle from 0.7 to 20 degrees the convoy peak decreases its magnitude by almost two orders of magnitude and shifts by about 10eV towards lower energy while its width increases. At 20° the peak can still be discerned, although quite softened.

The ELC electrons, which are mainly emitted isotropically around the ionization threshold in the projectile frame of reference, become highly localized at low polar angles when changing to the laboratory frame of reference. The peak position, E_p, for a given polar angle θ_i, is approximately given by $E_p \simeq k_p^2/2$, with $k_p = k\cos\theta_i$.

This shift is in agreement with experimental observation [2.2]. However, the intensity of the peak as a function of the angle of emission decreases much faster in our model than in the experiments as we have not only used a perturbative approach but also a simple model for the target electrons.

The individual contribution from the ELC and ECC electrons is shown in Figs. 2.5 and 2.6 for emission angles of 0.7° and 20° respectively. At low electron energies only the surface electrons contribute to the TDCS,

while at the convoy peak energies a different behavior occurs. For the lower angle of emission we see that both contributions to the convoy electrons are quite similar, not being so at the higher angle, where the ECC electrons do not show any structure at convoy energies.

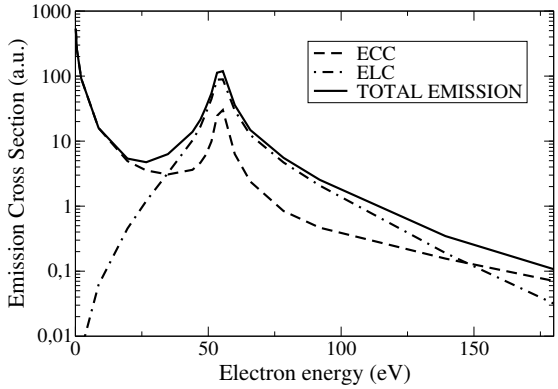

Figure 2.5: H^+-LiF electron emission at 0.7° polar angle; projectile (dashed line) and surface (dash-dotted line) electron contributions.

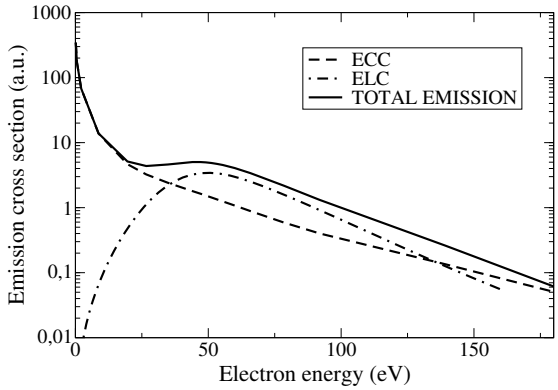

Figure 2.6: H^+-LiF electron emission at 20° polar angle; projectile (dashed line) and surface (dash-dotted line) electron contributions.

2.4 Conclusions

The model described for the H^+-LiF grazing collision electron emission shows that the projectile electron contribution to the total emission is of the order, or even greater than, the surface electrons, at convoy peak energies. At polar angles of emission $\gtrsim 15°$ in the scattering plane the

contribution of the surface electrons to the convoy electrons becomes negligible, being the peak formed mostly by projectile electrons.

2.5 Acknowledgments

This work was in part supported by Eusko Jaurlaritza, Euskal Herriko Unibertsitatia, Donostia International Physics Center and the Spanish M.C.Y.T. (under contract BFM2001-0076)

2.6 References

[2.1] K. Kimura, M. Tsuji, M. hiko Mannami, Phys. Rev. A 46 (5) (1992) 2618.

[2.2] E. Sanchez, O. Grizzi, G. Nadal, G. Gómez, M. Martiarena, V. Ponce, Nucl. Instrum. Methods Phys. Res. B 90 (1994) 261.

[2.3] M. Martiarena, E. Sánchez, O. Grizzi, V. Ponce, Phys. Rev. A 53 (2) (1996) 895.

[2.4] K. Kimura, G. Andou, K. Nakajima, Nucl. Instrum. Methods Phys. Res. B 164-165 (2000) 933.

[2.5] H. Winter, Physics Reports 367 (2002) 387.

[2.6] J. Briggs, F. Drepper, J. Phys. B 23 (23) (1978) 4033.

[2.7] Y. T. Lee, J. C. Chen, Phys. Rev. A 19 (2) (1979) 526.

[2.8] V. Ponce, R. Baragiola, J. Phys. B 17 (1984) 2467.

[2.9] A. Salin, JPB 22 (1989) 3901.

[2.10] R. McCarroll, A. Salin, J. Phys. B 1 (1968) 163.

[2.11] M. McDowell, J.P.Coleman, Introduction to the Theory of Ion-Atom Collisions, North-Holland, Amsterdam, 1970.

[2.12] M. L. Martiarena, V. H. Ponce, Nucl. Instrum. Methods Phys. Res. B 203 (2003) 62.

[2.13] L. Landau, E. Lifschitz, Quantum Mechanics, Pergamon, Oxford, 1977.

[2.14] P. Fainstein, V. Ponce, R. Rivarola, J. Phys. B 22 (1989) 1207.

[2.15] P. Fainstein, V. Ponce, R. Rivarola, J. Phys. B 24 (1991) 3091.

[2.16] M. Gravielle, Phys. Rev. A 62 (2000) 062903.

[2.17] I. Aldazabal, V. Ponce, A. Arnau, Phys. Stat. Sol. (b) 241 (10) (2004) 2374.

[2.18] J. Hubbell, et al., J. Phys. Chem. Ref. Data 4 (3) (1975) 471.

[2.19] M. Gravielle, J. Miraglia, Phys. Rev. A 44 (1991) 7299.

[2.20] M. Gravielle, J. Miraglia, Phys. Rev. A 51 (1995) 2131.

[2.21] J. Ziegler, J. Biersack, U. Littmark, The Stopping and Range of Ions in Matter, Vol. 1, Pergamon, New York, 1985.

Chapter 3

Electron emission and energy loss in grazing collisions of protons with insulator surfaces

Published as M.S. Gravielle, I.Aldazabal, A. Arnau, V.H. Ponce, J.E. Miraglia, F. Aumayr, S. Lederer and H. Winter in Phys. Rev. A **76**, 012904 (2007).

Abstract

Electron emission from LiF, KCl and KI crystal surfaces during grazing collisions of swift protons is studied using a first order distorted-wave formalism. Owing to the localized character of the electronic structure of these surfaces we propose a model that allows us to describe the process as a sequence of atomic transitions from different target ions. Experimental results are presented for electron emission from LiF and KI and energy loss from KI surfaces. Calculations show reasonable agreement with these experimental data. The role played by the charge of the incident particle is also investigated.

PACS: 34.50.Dy, 34.50.Fa, 34.50.Bw

DOI: 10.1103/PhysRevA.76.012904

3.1 Introduction

The interaction during grazing scattering of fast ions from insulator surfaces comprises two interesting features: the localized character of the electronic structure of the surface and the geometry of the collision that favors large electron yields [3.1, 3.2]. In this work we investigate electron emission produced during grazing collisions of fast protons with ionic crystals such as LiF, KCl and KI. These materials are typical broad band-gap insulators with a narrow valence band, which indicates that valence electrons retain essential parts of their atomic character.

At high impact energies, protons move along the trajectory mainly as bare ions. Therefore, ejected electrons essentially originate from direct ionization of the surface. To describe this process we employ a theoretical model that makes use of the local character kept by valence electrons, representing the electronic transitions induced by the projectile along its path as a succession of single collisions with the surface ions [3.3]. In this model, target ionization probabilities associated with binary encounters are evaluated with the continuum-distorted-wave eikonal-initial-state (CDW-EIS) approximation, which is a distorted-wave method successfully used in the field of ion-atom collisions [3.4]. The classical trajectory of the incident ion is described by means of a punctual model [3.5] that considers the individual interactions of the projectile with the solid ions placed at the sites of the crystal lattice.

For the different targets we present calculations of the electron emission probability as a function of the incidence angle and discuss the influence of the electronic structure of the medium. In the case of LiF and KI, theoretical results are compared with measurements of electron emission yields for grazing scattering of hydrogen atoms.

In addition, we study the energy loss of projectiles during grazing scattering. Experimental data for the energy loss of H^0 colliding with a KI(001) surface are shown and compared with values obtained from the theoretical model. The role played by the charge state of the projectile is analyzed. A small fraction of H^0 gives an important contribution around the convoy peak that appears in electron emission spectra measured in forward direction [3.6], but this mechanism of projectile ionization is negligible compared to the total electron emission yield and energy loss.

The theoretical formalism is summarized in Sec. 3.2, and the experimental method and setup are described in Sec. 3.3. In Sec. 3.4 we discuss

results for electron emission and energy loss, and outline in Sec. 3.5 our conclusions. Atomic units are used unless otherwise stated.

3.2 Theoretical model

When a heavy projectile impinges grazingly on an solid surface, it interacts mainly with valence electrons belonging to the first atomic plane. For ionic crystals, as a consequence of the localized character of the valence orbitals [3.7], we can assume that electron emission from the surface is essentially caused by a sequence of binary collisions between the projectile and surface ions. Then the emission probability per unit path length from the initial state i bound to the surface is expressed as [3.3]

$$\frac{dP_i}{dx} = \delta_s \int_{-\infty}^{+\infty} dy P_i^{(at)}(\rho(\vec{r})), \tag{3.1}$$

where $P_i^{(at)}(\rho)$ is the probability of atomic ionization from the state i, as a function of the impact parameter ρ, and δ_s is the surface atomic density, which is considered a constant. In Eq.(3.1) the impact parameter ρ depends on the position $\vec{r} = (x, y)$ of the considered surface ion, with

$$\rho(\vec{r}) = \sqrt{y^2 + Z(x)^2}, \tag{3.2}$$

$Z(x)$ being the distance of the projectile to the surface, and x (y) the coordinate parallel (perpendicular) to the scattering plane within the surface (see Fig. 3.1). Note that, unlike the differential atomic ionization probability, which describes the angular distribution of emitted electrons, the total probability of atomic ionization from the state i, $P_i^{(at)}$, does not depend on the azimuthal angle of the impact parameter, as results from Eq. (3.1).

In order to produce a consistent description of continuum electronic states in the fields of both the passing projectile and the effective charge left in the surface after ionization, we employ for the calculation of $P_i^{(at)}$ the CDW-EIS approximation. Within this theory the T-matrix element reads

$$T_{if} = \left\langle \chi_f^{CDW-} \left| W_f^{\dagger} \right| \chi_i^{E+} \right\rangle, \tag{3.3}$$

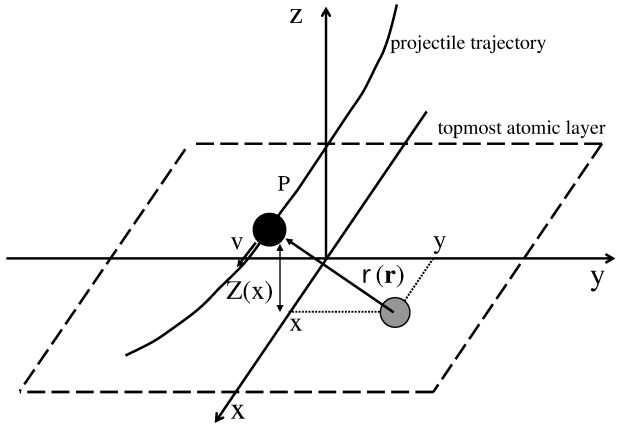

Figure 3.1: Sketch of the coordinate system.

where χ_f^{CDW-} and χ_i^{E+} are the CDW and eikonal wave functions, with the proper asymptotic conditions in the final and initial channels, respectively, and W_f is the final perturbative potential. Details on the calculations can been found in previous papers [3.3, 3.8].

In these collisions, apart from direct electron emission from the surface, there is another contribution from H^0 ionization (electron loss), which is at least one order of magnitude smaller. We have checked this by explicitly including electron capture and loss by the projectile. For the capture process we use the eikonal-impulse approximation, which is a distorted wave method making use of the exact impulse and eikonal wave functions in the final and initial channels, respectively [3.9, 3.10]. The projectile emission probability is calculated [3.6, 3.11] in the impact-parameter first-Born approximation [3.12]. In this manner the charge state of the projectile along the trajectory is evaluated [3.6].

3.3 Experimental method

The experiments are performed with a small ion accelerator at Humboldt University Berlin. Neutral hydrogen atoms with energies from 100 to 300 keV are scattered under grazing angles of incidence ranging from Φ_{in} = 0.5° to 1° from clean and flat LiF(001) and KI(001) surfaces. The target surface was kept under UHV condition at a pressure of typically

some 10^{-11} mbar and prepared by frequent cycles of sputtering with 50 keV Ar ions under $\Phi_{in} = 2°$ and subsequent annealing at 400°C. The state of preparation of the target was checked via angular distributions for scattered projectiles which allows one to obtain information on the defect structure of the surface [3.13]. In the final state of preparation of the target we observed well-defined angular distributions with negligible sub- and supraspecular tails which can be attributed to a mean width of terraces formed by topmost layer atoms larger than 1000 a.u. In order to avoid macroscopic charging up of the target surface, the crystal was kept at a temperature between 100°C and 300°C, where alkali halide crystals show sufficient conductivity. By sets of horizontal and vertical slits the incoming proton beam was collimated to a divergence in the submilliradia domain and chopped by a pair of electric plates biased with voltage pulses with a rise time of a few nanoseconds. The pulsed ion beam was then neutralized via near-resonant charge exchange in a gas target operated with Kr atoms.

Since grazing scattering of atomic particles from the surface proceeds in the regime of surface channeling [3.13, 3.14], the kinetic energy for the motion normal to the surface plane scales according to $E_\perp = E\ sin^2\Phi_{in}$. Then, for projectile energies of typically 100 keV, $E_\perp$ is in the eV range, so that projectiles cannot penetrate the bulk of the crystal and are specularly reflected from the topmost layer of surface atoms. The scattered beam is detected 1.38 m behind the target by means of a multichannel plate detector where the output pulse serves as start signal of a time-of-flight (TOF) setup for measurements of the projectile energy loss. The overall time resolution of our TOF system is about 5 ns, which amounts to an energy width of the scattered beam of about 1 keV at 100 KeV impact energy.

The number of emitted electrons during the impact of a projectile is measured using a surface barrier detector (SBD) biased to a voltage of about 25 keV. The detector pulse height is proportional to the electron number ejected per projectile impact on the surface [3.15]. Emitted electrons are collected by a bias of some 10 V applied to a highly transparent grid, which also shields the target region from the high electric field owing to the high voltage on the SBD. As detailed elsewhere [3.16], coincident detection of projectile energy loss with the number of emitted electrons is achieved by relating the TOF signals to the pulse heights of the SBD. From intensities of the SBD spectra for emission of a number of i electrons, W_i, we obtain the total electron yield $\gamma = \sum iW_i / \sum W_i$. Since

the collection efficiency of our setup for emitted electrons is about 98%, accurate total electron yields are obtained by this method which can be compared to the calculations on an absolute scale.

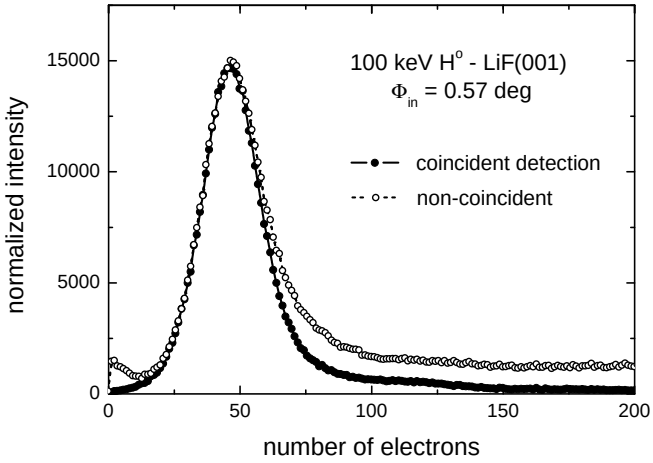

Figure 3.2: Pulse height distributions of the amplified SBD signal for coincident (full circles) and noncoincident (open circles) detection with 100 keV H^0 projectiles specularly reflected from a LiF(001) surface under $\Phi_{in} = 0.57°$.

As an example for our experimental data we show in Fig. 3.2 the pulse height distributions of the amplified SBD signal for coincident (full circles) and noncoincident (open circles) detection with 100 keV H^0 projectiles specularly reflected from a LiF(001) surface under $\Phi_{in} = 0.57°$. The pulse height scale of the SBD is converted to number of emitted electrons, where the conversion factor is derived from previous experiments at lower projectile energies. Compared to the detection of low electron numbers, peaks owing to the emission of specific numbers of electrons are no longer resolved. The data show a Gaussian type of distribution peaking at about 50 emitted electrons. For the noncoincident detection of electrons we note additional signals owing to detector noise for low pulse heights and owing to subsurface scattering for higher pulse heights. The latter contribution to the noncoincident electron spectrum can be attributed to the penetration of projectiles into the subsurface regime, where electron densities are higher and, in particular, projectile trajectories for the interaction with the solid are much longer than for reflection in front of the surface plane [3.1]. The two spectra in Fig. 3.2 indicate

that the present experimental method allows us to separate the two mechanisms for the kinetic emission of electrons from the target. We note that the frequently used technique based on measurements of target currents cannot be applied here because of these specific problems. Furthermore, charging-up effects present with insulators can be neglected here, since at a slightly elevated temperature (about 100°C) the conductivity of LiF and KI is sufficiently high and the primary neutral beams consist of some 1000 atoms per second only (equivalent to ion currents of subfemtoamperes).

3.4 Results

In the present work we studied grazing collisions of protons with LiF(001), KCl(001) and KI(001) surfaces in the intermediate- and high-velocity regime, i.e., impact energies ranging from 100 to 300 keV. For the different collision systems, we evaluated the charge state of the incident projectile along its trajectory and found that, even for the lowest energy, the fraction of protons is more than one order of magnitude greater than that of neutral hydrogen atoms [3.6]. This holds also for impact of neutral atoms, as follows from the calculations displayed in the lower panel of Fig. 3.3. Furthermore, the electron emission yield and energy loss due to projectile ionization for H^0-surface collisions are typically about one order of magnitude smaller than the contributions for the H^+-surface system. Therefore, direct ionization from the surface induced by bare ions is the dominating mechanism for the electron emission and energy loss of the projectile.

Owing to the geometry of the collision, associated with grazing trajectories, most emitted electrons come from outer shells of target ions. We consider the ionization from the L, M, and O shells of the F^-, Cl^-, and I^- anions, and from the K and M shells of the Li^+ and K^+ cations, respectively. In the evaluation of the atomic transition probability we used the Hartree-Fock wave functions of Ref. [3.17] to represent the initial atomic bound states, while the final continuum states, associated with electrons ejected from surface ions, were described as Coulomb wave functions with effective charges satisfying the corresponding initial binding energies.

The electron emission probability, which coincides with the average number of emitted electrons per incident ion, is obtained from Eq. (3.1) by integrating dP_i/dx along the projectile trajectory. To represent the

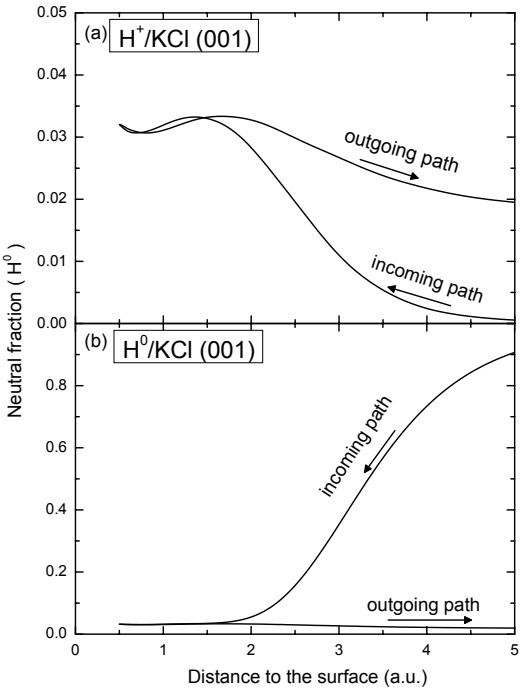

Figure 3.3: H^0 fraction as a function of the the distance of the projectile to the KCl(001) surface for incidence of 100 keV (a) protons; (b) neutral hydrogen atoms.

classical path of the proton we employ the punctual model of Ref. [3.5], in which the projectile-surface potential is expressed as a sum of individual potentials that describe the static interaction between the projectile and the crystal ions placed at the lattice sites [3.18]. The projectile trajectory was derived from classical dynamic by employing the Runge-Kutta method, taking into account four atomic layers of the solid. The polar angle of the incident velocity was chosen far from low-index crystallographic directions ($\theta_i = 30°$) and for every angle Φ_{in} approximately 50 specularly reflected trajectories with random initial positions were considered. Note that, at the present impact energies, the long lifetime of the charge imbalance left on the surface by successive ionization produces a track of positive effective charges that might affect the proton trajectory [3.8]. However, this interaction is partially compensated by the dynamic polarization of the surface [3.18], which is weaker than for metal surfaces but

acts for a long time in a grazing collision, so it may reduce the effect of the track potential.

3.4.1 Electron emission

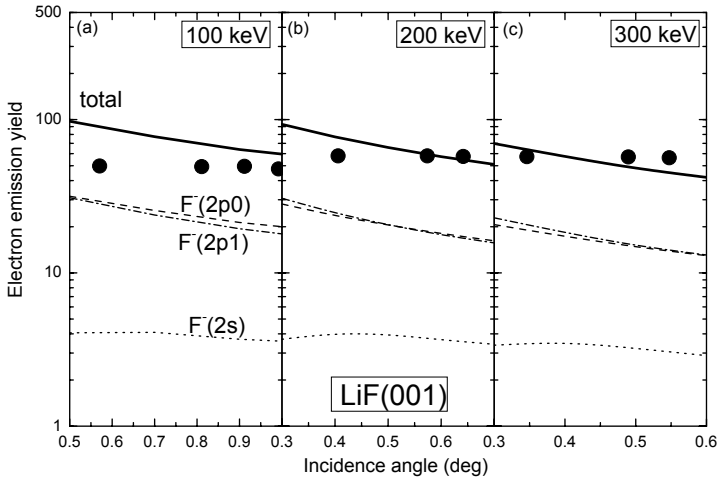

Figure 3.4: Electron emission yields for grazing protons colliding with LiF(001) surfaces, as a function of the incidence angle, measured with respect to the surface plane. Three different impact energies are considered: (a) 100 keV; (b) 200 keV; (c) 300 keV. Full dots, present experimental data; solid lines, theoretical values derived as explained in the text.

We start the analysis by a discussion of electron emission from a LiF surface and a comparison of our calculations with the experimental data. In Fig. 3.4 we display total electron emission yields, which are identical with total electron emission probabilities, as a function of the incidence angle for three different impact energies: 100 (left panel), 200 (middle panel), and 300 keV (right panel). The theoretical results are compared with measurements where via a bias potential of some 10 V electrons are collected with a detection efficiency close to 1. Our calculations show an overall accord with the experiments; as expected for a first-order distorted-wave theory, the agreement improves when the impact velocity increases. Note, however, that in spite of the general concordance between theory and experiment, measurements do not vary appreciably with the incidence angle and energy, while theoretical values show a slight decrease as these parameters increase. In our calculations the dominant process

corresponds to emission from $F^-(2p)$ orbitals and the contribution from Li^+ (not displayed in Fig. 3.4) is around two orders of magnitude lower than that from F^- due to the small radius of the alkali-metal ion. With respect to the projectile path, note that the critical angle at which the projectile penetrates in the solid is very sensitive to the projectile-surface potential. As an example, for 100 keV proton impact with an incidence angle $\Phi_{in} = 1°$, within the punctual model only 0.4% of the trajectories are specularly reflected at the topmost atomic layer. For such reflected trajectories the projectile moves very close to the surface plane, producing a large electron emission yield. We have also investigated the effect of the polarization potential proposed in Ref. [3.18]. Even though at large incidence angles the polarization considerably affects the penetration of ions, under specular reflection conditions its effect on our theoretical results was found to be small.

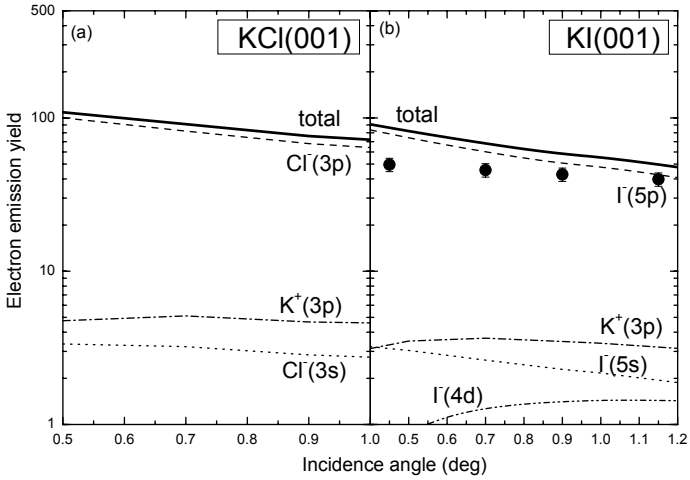

Figure 3.5: Similar to Fig. 4 for 100 keV protons impinging on (a) KCl(001); (b) KI(001) surfaces.

In Fig. 3.5 we show electron emission probabilities for 100 keV protons impinging on two different targets, KCl(001) (left panel) and KI(001) (right panel). Again the outer p orbitals of the target anions give the most important contribution to electron emission, while contributions to electron yields from K^+ cations are substantially smaller. Measurements of electron emission yields for a KI(001) surface are displayed in Fig. 3.5(b). As also observed in Fig. 3.4(a), at 100 keV the present distorted-wave theory overestimates the experimental data for small in-

cidence angles, tending to the measured values as Φ_{in} increases. By comparing Figs. 3.4(a) and 3.5 we reveal that the electron emission probability varies only slightly with the crystal surface. For a given glancing incidence angle the electron emission yields are comparable for the three targets considered. This can be associated with the fact that two related effects almost compensate each other: a larger surface ion radius gives rise to a higher probability of atomic ionization for surface atoms, but also to a lower surface atomic density, which leads to a lower emission probability from the surface.

In all cases, our results show a high efficiency of light projectiles like H^+ in ionizing the surface of ionic crystals, producing more than 50 ionizations on the average for 100–300 keV. This yield is clearly larger than the number of emitted electrons from, e.g., a Cu surface for similar impact velocities [3.20]. In general, total electron emission yields from insulator surfaces are substantially higher than those from metal or semiconductor surfaces [3.1, 3.21].

3.4.2 Energy loss

The loss of kinetic energy suffered by the projectile during the collision with the surface is associated with the energy transferred in electronic transitions. We evaluate the energy lost by the projectile from Eq. (3.1) by replacing the atomic transition probability by the energy loss corresponding to the atomic ionization process [3.8].

Theoretical energy losses for 100 keV protons impinging on LiF (left panel), KCl (middle panel), and KI surfaces (right panel) are displayed in Fig. 3.6 as a function of the incidence angle. Measurements for KI are also included in Fig. 3.6(c). Again, at 100 keV impact energy the theoretical values agree with the experiment for large incidence angles, running above measured data for $\Phi_{in} \lessapprox 0.7°$. For KCl and KI, in contrast to electron emission, contributions to energy loss from $K^+(3p)$ orbitals become relevant, and the importance decreases only as the incidence angle is reduced. For LiF, instead, the energy lost by the projectile in collisions with alkali-metal ions is more than one order of magnitude lower than the anion contribution. This holds also for large incidence angles for which the projectile probes the region close to the surface.

In Fig. 3.7 we display the energy loss of neutral hydrogen atoms impinging on a KI(001) surface with a glancing angle ($\theta_i = 0.5°$). Mea-

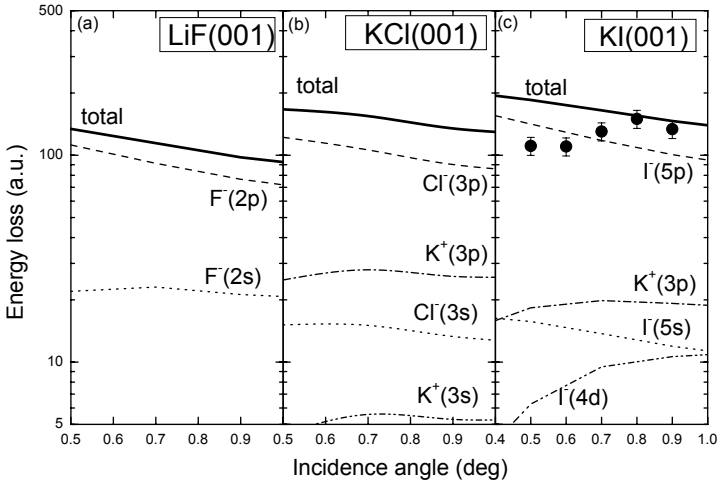

Figure 3.6: Energy loss for grazing scattering of 100 keV protons from insulator surfaces, as a function of the incidence angle. The target surfaces are (a) LiF(001); (b) KCl(001); (c) KI(001). Solid lines, theoretical results; full dots, present experimental data.

surements of the energy loss as a function of the incidence energy are compared with theoretical results derived from our model by considering proton impact. At high energies the projectile moves close to the surface mostly as a bare ion. This holds also for incidence of H^0 projectiles (cf. Fig. 3.3). Theoretical and experimental values are in a good agreement, showing only a slight overestimation of the experimental data at lower energies. As pointed out before, this discrepancy might be based on the first-order perturbative approach used here [3.22].

3.5 Conclusions

We have presented calculations for the emission of electrons from LiF, KCl, and KI crystal surfaces by grazing incidence of H^+, and measurements for electron emission from LiF and KI surfaces by impact of H^0 projectiles. We showed that the main mechanism of electron emission is the direct ionization of the surface induced by protons. Contributions to electron emission from the H^0 charge state of the projectile were found negligible since this charge fraction is an order of magnitude smaller than the H^+ fraction at the energies considered here. For the different crystals,

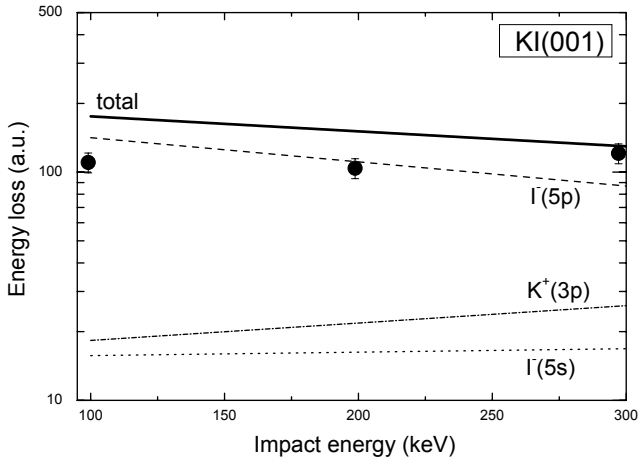

Figure 3.7: Energy loss for grazing scattering of H^0 from KI(001) surfaces, as a function of the impact energy. Full dots, present experimental data; solid line, theoretical results for proton impact.

theoretical predictions show a weak dependence on the surface density because the effect of a smaller surface density for a larger halogen ion radius is compensated by a larger ionization cross section.

Reasonable agreement between theoretical and experimental data was found. The theory reproduces well measured values for high impact energies, departing from the experimental results when both incidence energy and angle decrease. Total electron emission yields amount to about 50 electrons for 100–300 keV protons impinging on a LiF surface. These values are larger than those observed for metal or semiconductor surfaces [3.1, 3.20].

The energy loss of projectiles along the grazing trajectory was also investigated, analyzing the contributions from different subshells of the target ions. Theoretical values were compared with experimental data for H^0 projectiles colliding with KI surfaces, and a fairly good concordance between them was found. As in the case of electron emission, measurements are almost independent of the impact velocity, while calculations smoothly decrease with the increase of this parameter, showing a better accord with the experiment for high velocities.

3.6 Acknowledgment

This work was supported by CONICET, UBA, and ANPCyT of Argentine and by the DFG under contract Wi1336. M.S.G. thanks the High-Performance Opteron Parallel Ensemble Cluster (Institute of Astronomy and Space Science) for providing computational support for this work. I.A. and A.A. are grateful to the Basque Departamento de Educación, Universidades e Investigación, the University of the Basque Country UPV/EHU, the Spanish Ministerio de Educación y Ciencia, and the EU Network of Excellence NANOQUANTA (Grant No. NMP4-CT-2004-500198) for financial support.

3.7 References

[3.1] K. Kimura, G. Andou, and K. Nakajima, Phys. Rev. Lett. **81**, 5438 (1998).

[3.2] H. Winter, Prog. Surf. Sci. **63**, 177 (2000).

[3.3] M. S. Gravielle, Phys. Rev. A **62**, 062903 (2000).

[3.4] P. D. Fainstein, V. H. Ponce and R. D. Rivarola, J. Phys. B **24**, 3091 (1991).

[3.5] A.J. García and J.E. Miraglia, Phys. Rev. A **74**, 12902 (2006).

[3.6] I. Aldazabal, M. S. Gravielle, J. E. Miraglia, A. Arnau, and V. H. Ponce, Nucl. Instrum. Methods Phys. Res. B **232**, 53 (2005).

[3.7] A. Zunger and A. J. Freeman, Phys. Rev. B **16**, 2901 (1977).

[3.8] A. Arnau, M. S. Gravielle, J. E. Miraglia, and V. H. Ponce, Phys. Rev. A **67**, 062902 (2003).

[3.9] M. S. Gravielle and J.E. Miraglia, Phys. Rev. A **44**, 7299 (1991) .

[3.10] M. S. Gravielle and J. E. Miraglia, Phys. Rev. A **51**, 2131 (1995).

[3.11] I. Aldazabal, V.H. Ponce and A. Arnau, Phys. Stat. Sol. (b) 241 (10) (2004) 2374.

[3.12] M.R.C. McDowell and J.P.Coleman, *Introduction to the Theory of Ion-Atom Collisions*, North-Holland, Amsterdam, 1970.

[3.13] H. Winter, Phys. Rep. **367**, 387 (2002).

[3.14] D. S. Gemmell, Rev.Mod.Phys. **46**, 129 (1974).

[3.15] F. Aumayr, G. Lakits, and HP. Winter, Appl. Surf. Sci. **63**, 177 (1999).

[3.16] A. Mertens et al., Nucl. Instr. Meth. Phys. Res. B **182**, 23 (2001).

[3.17] E. Clementi and C. Roetti, At. Data Nucl. Data Tables **14**, 177 (1974), Tables 2 and 44.

[3.18] A.J. García and J.E. Miraglia, Phys. Rev. A **75**, to be published (2007).

[3.19] J.F. Ziegler, J.P. Biersack and U. Littmark, *The Stopping and Range of Ions in Solids*, Vol. 1, Pergamon Press, New York, 1985.

[3.20] S. Lederer and H. Winter, Phys. Rev. A **73**, 054901 (2006).

[3.21] M. Vana, F. Aumayr, P. Varga, HP. Winter, Europhys. Lett. **29**, 55 (1995).

[3.22] P. D. Fainstein, V. H. Ponce, and A. E. Martinez, Phys. Rev. A **47**, 3055 (1993).

Part II

Field emission resonances in Cu(100) surfaces

Chapter 4

Role of electric field in surface electron dynamics above the vacuum level

Published as J. I. Pascual, C. Corriol, G. Ceballos, I. Aldazabal, H.-P. Rust, K. Horn, J. M. Pitarke, P. M. Echenique and A. Arnau in Phys. Rev. B **75**, 165326 (2007).

Abstract

Scanning tunneling spectroscopy (STS) is used to study the dynamics of hot electrons trapped on a Cu(100) surface in field emission resonances (FER) above the vacuum level. Differential conductance maps show isotropic electron interference wave patterns around defects whenever their energy lies within a surface projected band gap. Their Fourier analysis reveals a broad wave vector distribution, interpreted as due to the lateral acceleration of hot electrons in the inhomogeneous tip-induced potential. A line-shape analysis of the characteristic constant-current conductance spectra permits to establish the relation between apparent width of peaks and intrinsic line-width of FERs, as well as the identification of the different broadening mechanisms.

PACS: 73.20.At, 68.37.Ef, 71.20.Be

DOI: 10.1103/PhysRevB.75.165326

4.1 Introduction

A detailed knowledge of the electron dynamics at surfaces is crucial for an understanding of a large variety of processes, ranging from electron scattering at surfaces to charge transport dynamics across interfaces, relevant to design electronic devices [4.1, 4.2]. Electrons trapped in unoccupied long-lived resonances represent an interesting workbench. They favour the localization of photo-injected electrons at molecular resonances, thus enhancing the catalytic activity of metals [4.3]. They also represent a valuable probe to investigate the rich phenomenology behind charge injection and hot-electron quenching. Experimental techniques such as inverse photoemission [4.4], two-photon photoemission [4.5], or ballistic electron scattering [4.6] have been traditionally used to study hot electron dynamics at surfaces.

Recently, scanning tunneling spectroscopy (STS) has proved to be a useful tool to provide quantitative information about the electronic structure [4.7–4.12] and also the electron and hole dynamics at metal surfaces [4.13–4.17]. In most cases, these studies have been restricted to low applied bias voltages, where the applied electric field does not play an important role [4.18]. A renewed interest has emerged in using the STM in the field-emission regime, i.e., at bias voltages larger than the tip work function. In this regime, the applied electric field lifts up the potential barrier above the vacuum level of the sample, introducing a new class of resonances that are absent at low bias voltages, the so-called field-emission resonances (FERs) [4.19, 4.20]. In previous studies, FERs have been used to explore local changes of the surface work function [4.21,4.22] and scattering properties of surfaces and interfaces [4.23, 4.24] and to achieve atomic-scale imaging of diamond [4.25]. A promising application of FERs is to provide information about the dynamics of electrons in image states at surfaces [4.15]. This is intriguing since FERs are a characteristic of the tip-induced potential barrier itself and, therefore, they would exist even in the absence of an image potential. Hence, a model is needed which describes the dependence of field emitted electrons dynamics along the surface on the topology of the surface potential and accounts for STS spectra in a wide sample bias range.

In this paper we demonstrate that electrons trapped in long-lived FERs are sensitive to the potential gradient induced by the STM tip along the surface. Scattering of quasifree FER electrons with surface defects gives rise to isotropic two-dimensional (2-D) wave patterns, whose wave vector components in reciprocal space reflect the local perturbation of the surface image potential induced by the STM tip. A combined theoretical and experimental analysis of the FERs peaks in dI/dV spectra reveals that their line shape carries information about the scattering properties of the surface, and hence, about their band structure. Our calculations permit the identification of the different intrinsic and extrinsic broadening mechanisms of peaks associated with FERs in conductance spectra in a wide energy range. The organization of the paper is as follows. Section 4.2 describes the way the experiments were done. In Sec. 4.3 we present the results and discussion of them in two subsections: Sec. 4.3.1 is devoted to the analysis of wave patterns that appear in dI/dV maps, while Sec. 4.3.2 presents a line-shape analysis of dI/dV spectra. Finally, in Sec. 4.4 the conclusions of our work are presented.

4.2 Experiment

The experiments were performed in a custom made ultra-high-vacuum scanning tunneling microscope in thermal equilibrium with a liquid-helium bath [4.26]. All spectroscopy data presented in this work were acquired at 4 K. The Cu(100) sample surfaces were cleaned by repetitive cycles of Ar^+ sputtering (1 keV) and annealing at 900 K. The differential conductance (dI/dV) was measured using a lock-in amplifier above the low-pass frequency of the feed back loop (f_{ac} ∼3 kHz). The dI/dV spectra shown here are taken in constant-current mode (feed back loop closed) [4.19, 4.20].

4.3 Results and discussion

4.3.1 Wave patterns

The electron dynamics of FER states is essentially quasi-free in the plane parallel to the sample surface, since the corresponding wave functions lie mainly on the vacuum side of the surface. Therefore, these electron

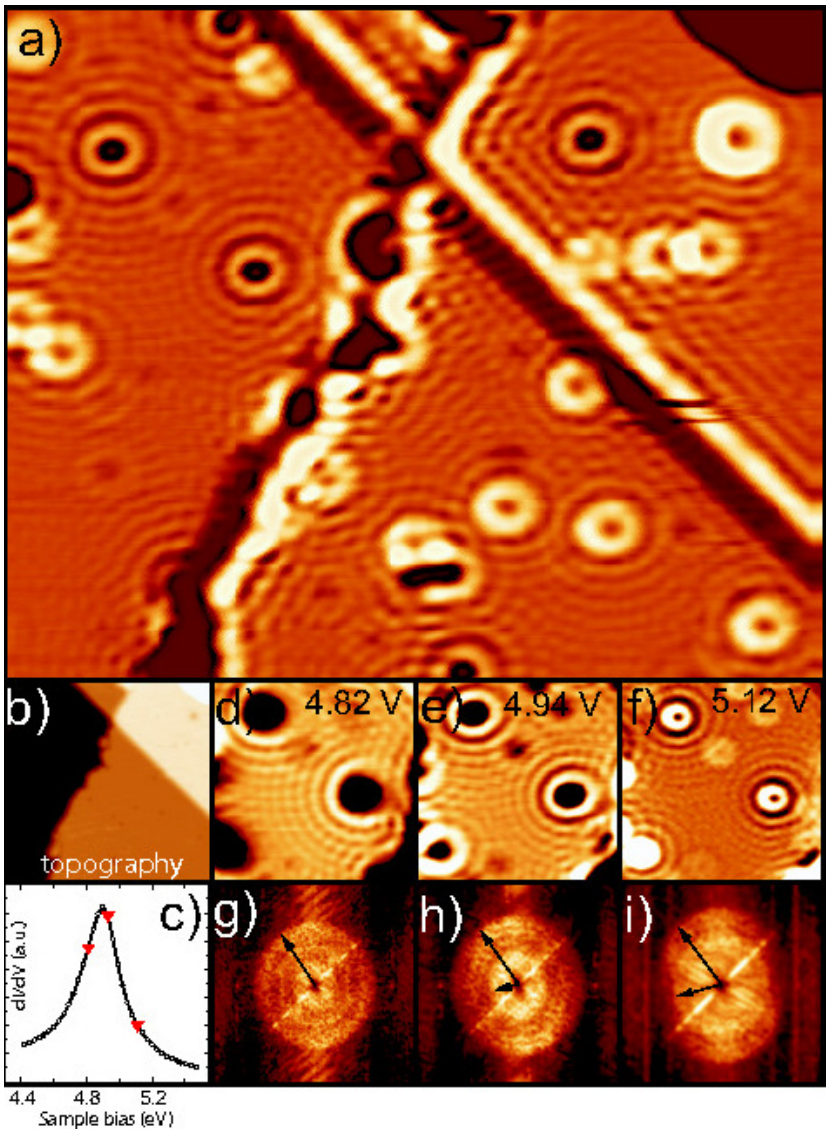

Figure 4.1: (a) dI/dV map of the Cu(100) surface shown in (b) (I=10 nA; V_S=4.9 V). Standing waves are clearly seen around steps, surface and subsurface defects. (c) Constant current dI/dV spectra around the first field emission resonance. [(d)–(f)] dI/dV maps of a smaller region taken at the bias values indicated in the figure. [(g)–(i)] 2D Fourier transform of (d)–(f). The arrows indicate the inner and outside radii of the disk appearing in K space (see the text).

states, similar to image-states, are not affected by the corrugation of the surface. As for the case of low-lying surface states, hot electrons in field emission resonances are expected to have a lifetime long enough to be scattered by steps and defects at the surface, giving rise to a characteristic standing-wave patterns. In Fig. 4.1(a), a constant current dI/dV map shows clear 2-D wave patterns around steps and point defects on the Cu(100) surface [Fig. 4.1(b)]. The image is measured with an applied bias voltage V_s of 4.9 V, corresponding to the position of the 1st FER peak [Fig. 4.1(c)]. A monotonic change to shorter wavelengths with the applied bias [Figs. 4.1(d)– 4.1(f)] reflects the energy dispersion of these states. At a first glance the dI/dV maps seem similar to those taken on the (111) faces of noble metals at lower bias. However, an important difference becomes apparent when looking at their 2D Fourier Transformation (FT) [Figs. 4.1(g)– 4.1(i)]: here the electron wave vector is not constrained to one single $k(E)$ value but shows a broad distribution, causing that the 2D FT maps resemble a disk instead of a ring [4.10].

We exclude that a surface-projected bulk band, instead of a two-dimensional state, is responsible of this broad distribution of k values in the 2D FT maps. Projected bulk bands' interference patterns might appear only at close distances to the sample and with oscillations corresponding only to wave vectors at the band edge [4.12]. Instead, the broad distribution of parallel momentum has its origin in the spatial variation of the electric field along the surface due to the finite curvature of the tip. The local shift of the surface potential induced by the STM tip vanishes gradually with the distance away from the tip position [Fig. 4.2(a)]. Accordingly, for a given electron energy E, the kinetic component along the surface directions ($E_k = E - E_{FER}$, where E_{FER} is the FER binding energy) increases continuously as the electron is accelerated away from the tip. Interference patterns carry information of such inhomogeneous potential by showing oscillations with shorter wavelength as the tip moves away from the scattering potential, and a FT map with nonconstant wave-vector distribution. Deviations from a perfect spherical shape of the tip apex structure are probably responsible for the elliptical shape of the contours.

The evolution of dI/dV maps of Figs. 4.1(d)–4.1(f) and their FT images show some interesting behavior. First, Fig. 4.1(d) shows clear dI/dV oscillations with relatively short wavelength although the image is taken with $eV_s < E_{FER}$, i.e. below the FER onset [as shall be shown later in subsection 4.3.2, the peak position in constant current dI/dV

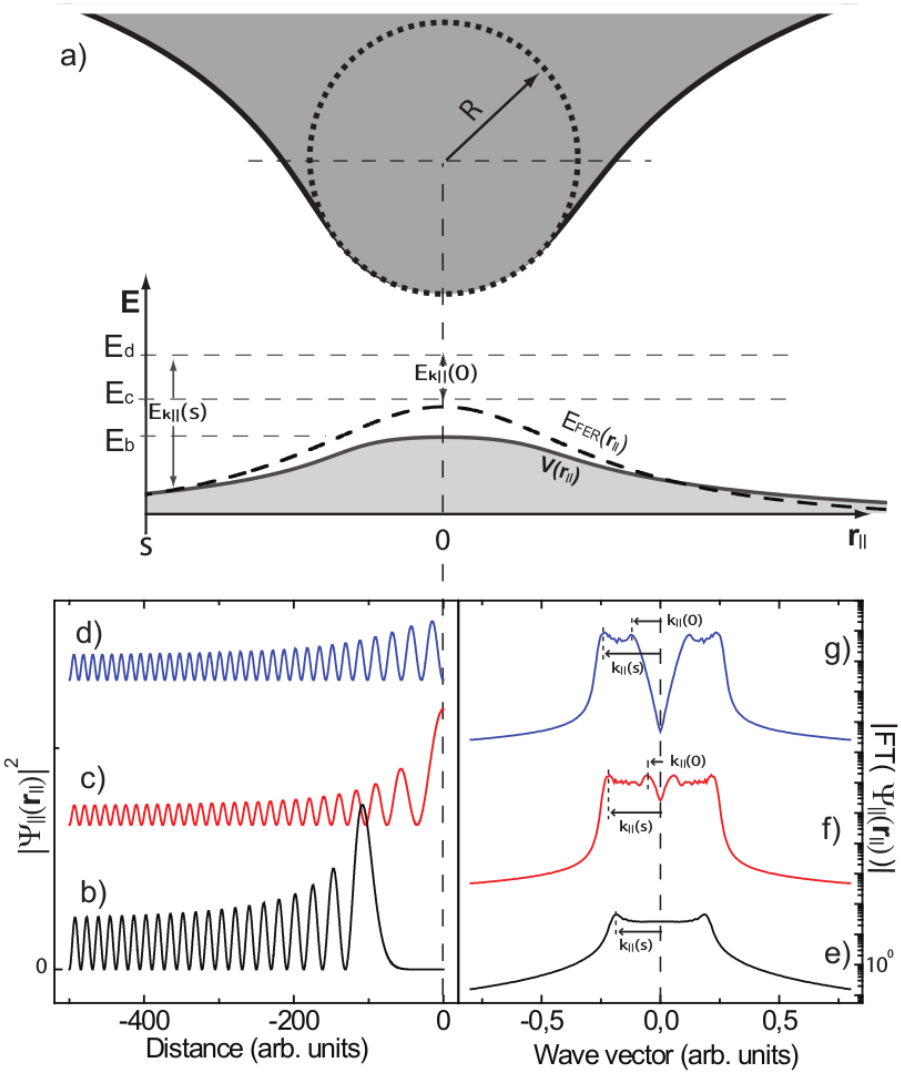

Figure 4.2: (a) Schematic representation of the non-conservation of parallel momentum due to the applied field by a tip of finite radius R. At a given value of electron energy $E = eV_s - \phi$ the kinetic energy for parallel motion $E_{k_{||}}$ increases from the tip position $r_{||} = 0$ to distant sites at the surface $r_{||} = s$. (b), (c), and (d) show the charge density of electron states confined in a large box with a potential $V(x) = V_0/[1 + (x/x_0)^2]$ with energy below, slightly above and above V_0, respectively [$V_0 = 0.03$ (arb. units) and $x_0 = 200$ (arb. units)]. (e), (f), and (g) show the corresponding FT. Curves (c), (d), (f), and (g) are shifted vertically for clarity. The arrows indicate the range of wave vectors with significant weight in the FT and, thus, confirm the measured behavior in Figs. 4.1(g)–4.1(i).

spectra like in Fig. 4.1(c) fits closely with the energy E_{FER}]. Second, for eV_s values above E_{FER} the FT maps show an internal circle with a radius k_{min} increasing with the energy [Figs. 4.1(h) and 4.1(i)]. The origin of these phenomena can be understood by plotting the electron states of a one dimensional quantum box with a decaying potential as in Fig. 4.2(a). In Fig. 4.2(b) we consider the case of an electronic state with energy lower than E_{FER}. In this case, no allowed state exists locally under the STM tip. Only at distances beyond the point where the energy $E = E_{FER}$ traveling states can exist. In the STM data [Fig. 4.1(d)], this translates into large dark circles at scattering points, and the onset of standing waves-patterns beyond a certain distance from the defects. In reciprocal space [Fig. 4.2(e)], a continuous window of wave-vector values from $k_{||}(0) = 0$ to $k_{||}(s)$ reflects the continuous acceleration of the electron waves from the tip position $r_{||} = 0$ to the scattering point $r_{||} = s$ at the surface. Following the same one-dimensional (1D) model, we expect that for electron energy above the resonance onset E_{FER} [Figs. 4.2(c) and 4.2(d)], a minimum wave vector $k_{||}(0) = 2m_e^*/\hbar^2(E - E_{FER})^{1/2}$ appears in the 1D plots [Figs. 4.2(f) and 4.2(g)], corresponding to the internal circle in Figs. 4.1(h) and 4.1(i).

Therefore, the width of the wave vector distribution will reflect the spatial change of the local (tip-induced) potential shift. Ideally, for a given value of the tip radius, the critical angle determined by the exponential decay of the Fowler-Nordheim transmittivity [4.27], permits the estimation of the maximum parallel component of the electric field at the tip and, therefore, the change of parallel momentum, based on simple classical trajectory considerations. Assuming a radius of curvature of the tip R=10 nm and a tip-sample distance Z=15 Å, we estimate a change in parallel momentum of 2 nm^{-1} at 5 V, in agreement with our previous analysis shown in figures 4.1(g)– 4.1(i). Results similar to those shown in Fig. 4.1 are observed for other FERs that appear below 8 eV. However, no wave patterns are seen above this value, indicating a significant decrease of the electron lifetime.

4.3.2 Line shape of dI/dV spectra

To understand the role of the surface electronic structure in the dynamics of FERs, next we explore the information contained in dI/dV spectra about the energy width of FERs by analyzing their line shape and

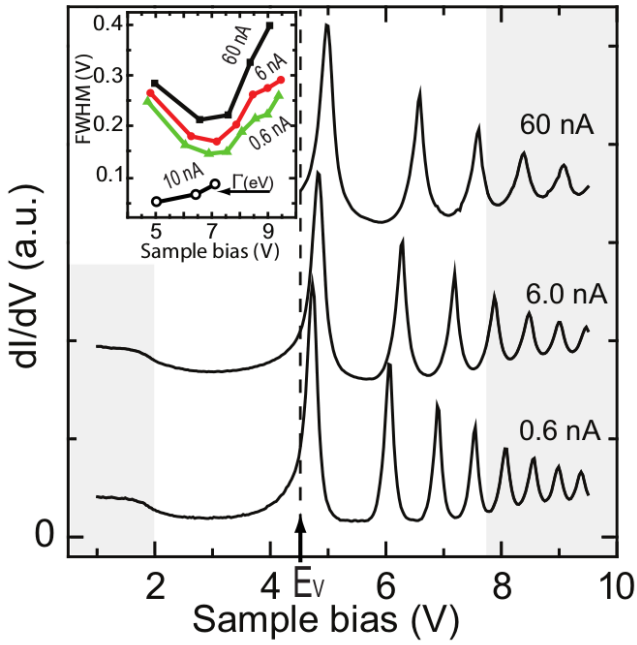

Figure 4.3: dI/dV spectra taken for several current set points ranging from 0.6 nA to 60 nA (V_{ac}=10 mV rms). The inset shows the width of the peaks from a Lorentzian fit, as well as values obtained from a phase coherence length analysis (Ref. [4.28]). Shaded areas correspond to the energy location in $\overline{\Gamma}$ of copper bulk bands projected on the (100) surface (Ref. [4.29]).

comparing with lifetime estimations based on a phase coherence length analysis of interference wave patterns [4.28].

In Fig. 4.3 we show a series of constant current dI/dV spectra at different set point current values. Sharp peaks appear in a wide sample bias range covering the energy range of the projected Cu bulk gap and above [4.29]. Each peak corresponds to the onset of a 2D resonance state. In field-emission regime, the tunnel transmittivity $T(E,V)$ is sharply peaked at the tip Fermi level ($E = E_F$); most of the current comes from a narrow energy window of about 100 meV below E_F [4.27], causing FERs to appear as peaks in dI/dV spectra. On the contrary, in case of surface states close to E_F, dI/dV spectra show a line shape close to a step [4.14]. Interestingly, we find that the apparent width of the dI/dV peaks exhibits a nonmonotonic behavior (shown in the inset). Resonances lying inside the gap are narrower than those appearing above

approximately 8 eV, whose width increases in agreement with the steep decrease of surface reflectivity as the top edge of the projected bulk band gap is crossed [4.6, 4.29].

The finite linewidth of resonance states in the gap is expected to be dominated by intrinsic factors like the electron reflectivity of the surface, spatial extension of the wave function [4.31], and electric field strength at the tip-sample region [4.30]. However, as it is shown in the inset of Fig. 4.3, the apparent width of the first three peaks in constant-current dI/dV spectra is considerably larger than the intrinsic line-width estimates based on a phase coherence length analysis [4.28], which for the first FER agree with previous *ab initio* calculations [4.30] and estimations [4.15] for the same system. Therefore, an additional broadening mechanism must exist to explain the apparent width values in these dI/dV plots, which, presumably, is related with the method of measurement.

During the acquisition of *dynamic* (constant-current) dI/dV spectra, the distance (Z) vs. bias voltage (V) characteristics [$Z(V)$] exhibit a pronounced steplike behavior as the resonance is crossed for electron energies lying in the projected gap. The resonant electron transmitivity in this close feedback loop spectroscopy is expected to be affected by the continuous change of the tunneling barrier shape with bias voltage and tip-sample distance. It is reasonable to assume that this dynamic mode will introduce some distortion in the resonance's line shape respect to the ideal *static* situation, in which the tunneling barrier shape is kept fixed at $Z(V)$ peak values. It is only in this latter case that one could relate the width of peaks in the transmitivity $T(E)$ to the intrinsic width of resonances. We have performed a model calculation to establish a link between intrinsic energy line-width of resonances in the static tunneling transmitivity $T(E)$ and the corresponding apparent width in constant-current dI/dV spectra, which is related to the auxiliary dynamic transmitivity $T(E_F, V)$ at the tip of the Fermi level.

Our calculations are based on 1D model potentials for the tip and sample including the work function and the Fermi energy that defines the bottom of the surface potential. For the surface, a periodic sinusoidal modulation that determines the magnitude and position of the energy gap at the $\overline{\Gamma}$ point of the surface Brillouin zone [4.32] is included. Parallel wavevector components are considered in the full three-dimensional calculations assuming a free-electron-like (parabolic) dispersion. To model

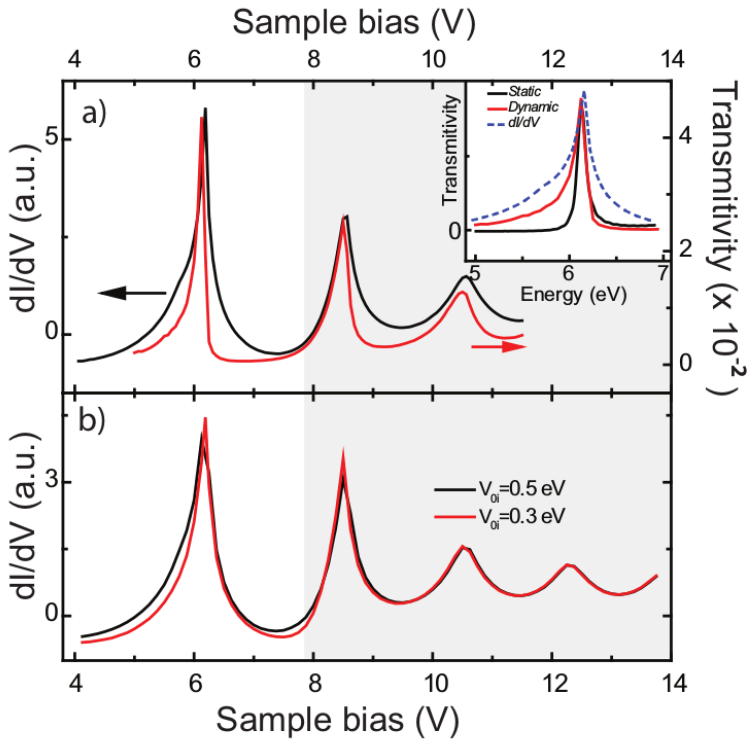

Figure 4.4: (color online) (a) Comparison between a calculated dI/dV spectrum (black curve) and the transmission coefficient (red curve) at the tip Fermi level $T(E_F; V)$. The inset shows a comparison between a static calculation (black) of $T(E)$ at $Z(V)$ values of the first resonance (thus reflecting the intrinsic FER line shape), $T(E_F; V)$ (red), and $dI/dV(V)$ (blue). (b)dI/dV spectra for two V_{0i} values (see the text).

electron transmission inside the gap, inelastic scattering at the surface is included by using a complex potential, similar to previous loew-energy electron-diffraction studies [4.33, 4.34]. Its imaginary part (V_{0i}) introduces a decay of the electron flux due to absorption. A smooth matching between the tip and sample potentials, which includes multiple images, is used [4.35]. The calculation of the tunneling current for a given tip-sample distance (Z) and bias voltage requires the knowledge of the energy dependence of the barrier transmission coefficient $T(E, V)$ below the tip's Fermi level E_F [4.36]. A quantitative agreement between the measured and calculated dI/dV spectra is not persecuted in this model approach, mostly due to the lack of knowledge of effective tunneling areas, tip-sample distance, or tip work function. Instead, we can provide a qualitative picture of the effect of the dynamic measurements on the peaks' width. The constant-current dI/dV spectra are calculated by numerical differentiation of the current $I(V, Z)$ along the constant current $Z(V)$ characteristic.

In Fig. 4.4(a) we show a comparison between calculated $dI/dV(V)$ spectra and the corresponding dynamic transmitivity $T(E_F; V)$. Both curves exhibit a similar shape and a characteristic increase of their linewidth with applied bias. This confirms the high collimation of field emitted electrons in a narrow energy window below E_F. The inset compares the conductance $dI/dV(V)$ around the first peak, the dynamic transmitivity $T(E_F, V)$, and the intrinsic line shape of the corresponding FER obtained in a static calculation at $Z(V)$ peak values. Lorentzian fits to $T(E_F, V)$ and $dI/dV(V)$ give width values of ∼150 meV and ∼350 meV, respectively, while the intrinsic width of the resonance in $T(E)$ is ∼100 meV. Therefore, the broader line shape in dI/dV spectra must be related both to the above-mentioned finite-energy collimation and the variation of the tunneling barrier shape with applied bias. For FERs in the gap, the increase in electric-field strength with bias shifts the resonances to higher energy, appearing as broader peaks in $dI/dV(V)$. The increase of tip-sample distance in the dynamic method of measurement partially compensates for this broadening effect. The best conditions for a quantitative line-shape analysis can be achieved at constant field strength conditions ($\sim V/Z$) and low set point current values (low applied field).

By comparing (Fig. 4.4(b) the shape of dI/dV curves calculated for two different values of V_{0i}, we find that only the first peak in the gap broadens as a response to the increase in absorption (inelastic scattering). This confirms that inelastic scattering is the broadening mechanism of

FERs lying inside the projected band gap. At energies above the gap, inelastic effects play a minor role [4.37] and the FER intrinsic linewidth is dominated by elastic coupling to the bulk continuum (shaded area). In this region, the intrinsic resonances' linewidth is considerably larger (hence, no wave patterns in dI/dV maps could be seen for this energy) and, also, V/Z is almost constant. It is then expected that the effect of the dynamic broadening will be smaller, and the experimental dI/dV peaks' apparent linewidth will be close to the intrinsic value.

4.4 Conclusions

We find that the scattering of electrons in field-emission states with defects in a Cu(100) surface gives rise to isotropic standing-wave patterns, which reflect their dynamics in response to the electric-field gradients induced by the STM tip at the tip-sample interface. Through a combined theoretical and experimental study we have identified: (i) the origin of characteristic peaks width in constant current dI/dV spectra above the vacuum level as a combination of both their FER intrinsic line shape and the extrinsic distortion due to the measuring process, and (ii) for FERs in the gap this distortion introduces an additional broadening, leading to a nonmonotonic behavior of the width with sample bias. Our results show that STS in the field-emission regime can be used to gain information about the electron dynamics and surface electronic properties at energies well above the vacuum level.

4.5 Acknowledgments

We gratefully acknowledge Lucia Aballe, Andrei Borisov, Martin Hansmann, Daniel Sánchez Portal and Wolf Widdra for very helpful discussions. This work was supported in part by the Basque Departamento de Educacion, Universidades e Investigacion, the University of the Basque Country UPV/EHU, the Spanish Ministerio de Educacion y Ciencia, the EU Network of Excellence NANOQUANTA (Grant No. NMP4-CT-2004-500198), and the EUROCORES project MOL-VIC.

4.6 References

[4.1] H. Nienhaus, Surf. Sci. Rep. **45**, 1 (2002).

[4.2] P. M. Echenique, R. Berndt, E.V. Chulkov, Th. Fauster, A. Goldmann, and U. Höfer, Surf. Sci. Rep. **52**, 219 (2004).

[4.3] U. Bovensiepen, Prog. Surf. Sci. **78**, 87 (2005).

[4.4] F. J. Himpsel and J. E. Ortega, Phys. Rev. B **46**, 9719 (1992).

[4.5] K. Boger, M. Weinelt, and Th. Fauster, Phys. Rev. Lett. **92**, 126803 (2004).

[4.6] S. Andersson and B. Kasemo, Solid State Commun. **8**, 961 (1970)

[4.7] M. F. Crommie, C. P. Lutz, and D. M. Eigler, Nature **363**, 524 (1993).

[4.8] Y. Hasegawa and Ph. Avouris, Phys. Rev. Lett. **71**, 1071 (1993).

[4.9] Ph. Hofmann, B. G. Briner, M. Doering, H.-P. Rust, E. W. Plummer, and A. M. Bradshaw , Phys. Rev. Lett. **79**, 265 (1997).

[4.10] L. Petersen, P. T. Sprunger, Ph. Hofmann, E. Lægsgaard, B. G. Briner, M. Doering, H.-P. Rust, A. M. Bradshaw, F. Besenbacher, and E. W. Plumer, Phys. Rev. B **57**, R6858 (1998).

[4.11] J. I. Pascual, Z. Song, J. J. Jackiw, K. Horn, and H.-P. Rust, Phys. Rev. B **63**, R241103 (2001).

[4.12] J. I. Pascual, A. Dick, M. Hansmann, H.-P. Rust, J. Neugebauer, and K. Horn, Phys. Rev. Lett. **96**, 046801 (2006).

[4.13] L. Bürgi, O. Jeandupeux, H. Brune, and K. Kern, Phys. Rev. Lett. **82**, 4516 (1999).

[4.14] J. Kliewer, R. Berndt, E. V. Chulkov, V. M. Silkin, P. M. Echenique and S. Crampin, , Science **288**, 1399 (2000).

[4.15] P. Wahl, M. A. Schneider, L. Diekhöner, R. Vogelgesang, and K. Kern, Phys. Rev. Lett. **91**, 106802 (2003).

[4.16] J.I. Pascual, G. Bihlmayer, Yu. M. Koroteev, H.-P. Rust, G. Ceballos, M. Hansmann, K. Horn, E. V. Chulkov, S. Blügel, P. M. Echenique, and Ph. Hofmann, Phys. Rev. Lett. **93**, 196802 (2004).

[4.17] C. Corriol, V. M. Silkin, D. Sánchez-Portal, A. Arnau, E. V. Chulkov, P. M. Echenique, T. von Hofe, J. Kliewer, J. Kröger, and R. Berndt, Phys. Rev. Lett. **95**, 176802 (2005).

[4.18] L. Limot, T. Maroutian, P. Johansson, and R. Berndt, Phys. Rev. Lett. **91**, 196801 (2003).

[4.19] G. Binnig, K. H. Frank, H. Fuchs, N. Garcia, B. Reihl, H. Rohrer, F. Salvan, and A. R. Williams, Phys. Rev. Lett. **55**, 991 (1985).

[4.20] R. S. Becker, J. A. Golovchenko, and B. S. Swartzentruber, Phys. Rev. Lett. **55**, 987 (1985).

[4.21] T. Jung, Y. M. Mo, and F. J. Himpsel, Phys. Rev. Lett. **74**, 1641 (1995).

[4.22] M. Pivetta, François Patthey, Massimiliano Stengel, Alfonso Baldereschi, and Wolf-Dieter Schneider, Phys. Rev. B **72**, 115404 (2005).

[4.23] J. A. Kubby, Y. R. Wang, and W. J. Green, Phys. Rev. Lett. **65**, 2165 (1990).

[4.24] A.J. Caamaño, Y. Pogorelov, O. Custance, J. Mendez, A.M. Baró, J.Y. Veuillen, J.M. Gómez-Rodríguez, J.J. Sáenz, Surf. Sci. **426**, L420 (1999).

[4.25] K. Bobrov, A. J. Mayne and G. Dujardin, Nature **413**, 616 (2001).

[4.26] H.-P. Rust, J. Buisset, E.K. Schweizer and L. Cramer, Rev. Sci. Instrum. 68, 129 (1997).

[4.27] J. W. Gadzuk, Phys. Rev. B **47**, 12832 (1993).

[4.28] We can estimate a phase coherence length following the analysis in Refs. [4.13, 4.15] neglecting the effect of the electric field on the wave patterns profile along the surface. It is implicitly assumed that when extracting the intrinsic lifetime $\tau = 1/\Gamma$ from the measured phase coherence length $L_\phi = v_\phi \tau$, a mean value of $k_{||}$ exists such that $mv_\phi = hk_{||}$, where m is the free electron mass. The mean value of $k_{||}$ is extracted from the wave length of the real space wave patterns and L_ϕ from the exponential decay of the amplitude of the oscillations that appear close to a straight step shown in Fig. 4.1. Although this mean value of $k_{||}$ is not well defined, it

would correspond to a value between the minimum and maximum values shown as arrows in Figs.4.2g. This "rough" estimation is heuristically justified since the result obtained is similar to the one obtained in Ref. [4.15] and since the wave vector dependence of the electron lifetime is not too pronounced [4.30].

[4.29] A. Goldmann, V. Dose and G. Borstel, Phys. Rev. B **32**, 1971 (1985).

[4.30] S. Crampin, Phys. Rev. Lett. **95**, 046801 (2005).

[4.31] P. M. Echenique and J. B. Pendry, Progress in Surface Science **32**, 111 (1989).

[4.32] E. V. Chulkov, V. M. Silkin, and P. M. Echenique, Surf. Sci. **437**, 330 (1999).

[4.33] J. B. Pendry, Low Energy Electron Difraction, (Academic Press, London, 1974).

[4.34] R. García, J. J. Sáenz, J. M. Soler and N. García , Surf. Sci. **181**, 69 (1986).

[4.35] J.M. Pitarke, F. Flores, and P.M. Echenique, Surf. Sci. **234**, 1 (1990).

[4.36] C. B. Duke, in "Tunneling in Solids" edited by F. Seitz, D. Turnbull and H. Ehrenreich (Academic Press, New York, 1969).

[4.37] A. Borisov, E. V. Chulkov, and P. M. Echenique, Phys. Rev. B **73**, 073402 (2006).

Chapter 5

Localization, splitting, and mixing of field emission resonances induced by alkali metal clusters on Cu(100)

Published as S. Stepanow, A. Mugarza, G. Ceballos and P. Gambardella (experimental team) and I. Aldazabal, A. G. Borisov and A. Arnau (theoretical team) in Phys. Rev. B **83**, 115101 (2011).

Abstract

We report on a joint scanning tunnelling microscopy (STM) and theoretical wave packet propagation study of field emission resonances (FERs) of nanosized alkali metal clusters deposited on a Cu(100) surface. In addition to FERs of the pristine Cu(100) surface, we observe the appearance of island-induced resonances that are particularly well resolved for STM bias voltage values corresponding to electron energies inside the projected band gap of the substrate. The corresponding dI/dV maps reveal island-induced resonances of different nature. Their electronic densities are localized either inside the alkali cluster or on its boundaries. Our model calculations allow to explain the experimental results as due to the co-existence and mixing of two kinds of island-induced states. On the one side, since the al-

kali work function is lower than that of the substrate, the nano-sized alkali metal clusters introduce intrinsic localized electronic states pinned to the vacuum level above the cluster. These states can be seen as the FERs of the complete alkali overlayer quantized by the cluster boundaries. On the other side, the attractive potential well due to the alkali metal cluster leads to two dimensional (2D) localization of the FERs of the Cu(100) surface, the corresponding split component of the resonances appearing below the bottom of the parent continuum. Our main conclusions are based on the attractive nature of the alkali ad-island potential. They are of general validity and, therefore, significant to understand electron confinement in 2D.

PACS: 73.20.At, 73.20.Hb, 73.22.Dj, 68.37.Ef

DOI: 10.1103/PhysRevB.83.1151011

5.1 Introduction

Scanning Tunneling Spectroscopy (STS) can be used to investigate unoccupied states at surfaces well above the Fermi level. In the field emission regime, the applied bias is larger than the surface work function and these unoccupied states are strongly distorted by the applied electric field. In this way, image potential states (ISs) are stark-shifted and actually become field emission resonances (FERs) as observed on different metal [5.1] and semiconductor surfaces [5.2]. FERs can be used to chemically identify different surface terminations from a study of the local changes in the work function [5.3–5.7] as well as to probe the effects of electron confinement in metallic [5.8, 5.9] and molecular [5.10] nanostructures. Since the energetics of FERs is to a large extent determined by the electric field at the junction, the interpretation of the data is relatively simple. This can be done using one dimensional models [5.11, 5.12], as long as both the tip radius of curvature and lateral extension of the surface area under interest are large compared to the tip-surface distances (a few nanometers when operating the STM at high bias voltages).

However, when the size of the nanostructures on the surface is not too large, the lateral confinement gives rise to a series of nanostructure-localized resonances [5.13, 5.14]. A priori, these are also modified by the electric field. In this case, the interpretation of dI/dV maps and point

spectra requires the use of three dimensional models that explicitly include the applied field. In this work, we present high resolution low temperature Scanning Tunneling Spectroscopy data of alkali (Li) nanoislands grown on Cu(100), as well as model calculations explaining the observed trends in both point spectra and dI/dV maps.

We find that the presence of the alkali clusters of nm size (nanoislands) on the metal surface induces: (i) new types of resonances with different azimuthal symmetry (m quantum number) [5.15,5.16] that originate from the island-localized image potential-like states pinned (for low quantum numbers) to the local vacuum level above the island, and (ii) the splitting of the original field emission resonances spatially extended all over the metal surface. Depending on their spatial distribution and relative energy positions, the island-localized resonances can mix with the localized split component of the conventional FERs of the supporting metal surface giving rise to multiple structures observed in dI/dV maps and spectra.

This paper is organized as follows. Section 5.2 contains a brief explanation of the experimental system and, as a main result, the STS data including both dI/dV maps and spectra of Li clusters on Cu(100). Section 5.3 presents the theoretical approach based on the wave packet propagation method, a discussion of the relevant approximations, and the interpretation of the experimental data. Finally, section 5.4 reports a summary of the most relevant findings and general conclusions.

5.2 Experiment

5.2.1 Methods

The experiments were carried out with a low-temperature STM (Createc) under ultra-high vacuum conditions. The STM chamber is equipped with standard tools for surface preparation and a combined low energy electron diffraction/Auger system to check the surface cleanliness. The base pressure is better than 2×10^{-10} mbar during preparation and lower than 1×10^{-11} mbar in the STM. The Cu(100) substrate was cleaned by repeated cycles of Ar^+ ion sputtering and annealing to 750 K. Lithium atoms were deposited onto the clean Cu(100) surface held at 300 K using a Li getter source (SAES Getters). The substrate was subsequently transferred to the low-temperature STM and cooled to 5 K.

We focus our investigation on small Li clusters of apparent diameter of about 1.1 nm and height of about 180 pm, when imaged at standard bias and current conditions (0.8 V, 0.3 nA), as shown in Fig. 5.1. These small clusters are mobile at room temperature, immobile at 5 K, and stable under imaging and spectroscopy conditions. The comparison with manipulation experiments of isolated Li atoms suggests that clusters of this size consist of four to five Li atoms. However, the actual chemical composition of the clusters remains unknown as it is possible for Cu atoms to intercalate with Li adatoms and form Li-Cu alloy superstructures [5.17, 5.18]. Experimentally, it was not possible to obtain atomic resolution within the Li clusters.

Field emission resonances (FER) were investigated by taking differential conductance (dI/dV) spectra in constant current mode (feedback loop closed). At the same time the relative tip-sample displacement $z(V)$ was recorded. The dI/dV spectra were obtained using a lock-in amplifier modulating the bias voltage at a frequency of 2.5 kHz above the cut-off frequency of the feedback loop with an amplitude V_{rms} = 14 mV. The typical acquisition time for a single spectrum is about 10 s. To obtain information on the lateral extension of the resonances, dI/dV maps at a fixed bias voltage were acquired in the constant current mode.

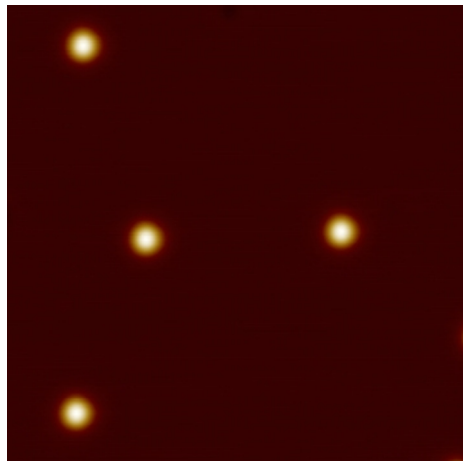

Figure 5.1: STM topograph of the Li clusters on Cu(100) investigated in the present study. Image size: 18×18 nm^2, V=0.8 V, I=0.3 nA.

5.2.2 Scanning Tunnelling Spectroscopy

dI/dV spectra were recorded on the bare Cu surface and on single Li clusters with no other cluster within a radius of at least 10 nm. The stability (position and shape) of the cluster and tip configuration was checked by taking topographs before and after acquisition of the dI/dV spectrum, as well as by repeatedly acquiring dI/dV spectra of the bare Cu surface. The cluster sometimes moved or hopped while ramping the bias voltage but never fragmented. Typical dI/dV spectra together with z(V) curves for the bare substrate and on the center of the Li clusters are presented in Figure 5.2.

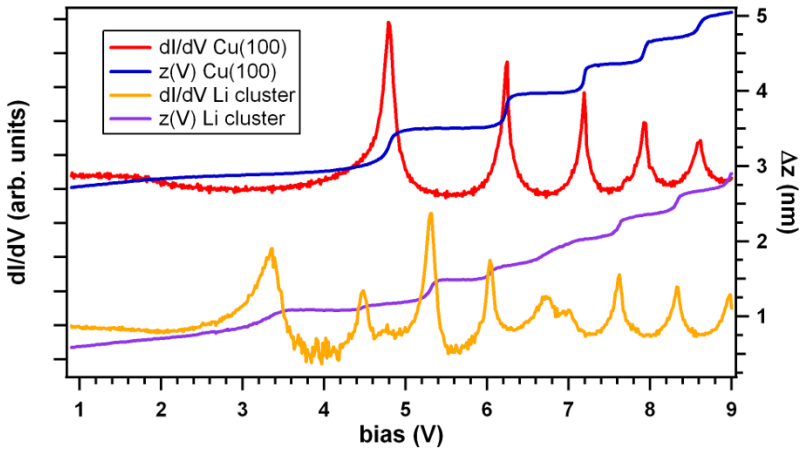

Figure 5.2: dI/dV spectra and corresponding z(V) curves obtained on the bare Cu(100) surface and on the center of the Li cluster in constant current mode. The spectra are shifted for clarity. Setpoint parameters are 0.8 V, 0.3 nA.

On the bare Cu(100) surface a series of resonances is observed (upper spectrum in Figure 5.2) that have been previously described as Stark shifted image state resonances [5.1]. Due to the presence of the STM tip and the associated strong electric field, these states are often referred to as field emission resonances (FERs). For each peak in the dI/dV spectrum there exist a corresponding step in the $z(V)$ characteristic. Depending on the tip conditions four to eight resonances are observed up to a bias of 9 V. The lowest resonance at about 4.8 V is less sensitive to the tip shape and has been considered as a measure for the local work function variations [5.3, 5.4, 5.7]. The lower spectra in Figure 5.2 were taken on top of a single Li cluster. The spectrum differs strongly from the bare

Cu(100) surface. Besides the apparent variations in the peak positions and spacing also the relative intensities differ from the flat metal surface. Above 7.5 V the series of resonances on top of the cluster resembles the spectrum on the bare surface, although significantly shifted in energy. The position of the resonances also depends on the tip conditions. On the Li cluster the lowest, and relatively broad, resonance is located at about 3.3 V followed by a noisy low conductance area at about 4 V. A small and sharp resonance is found at 4.5 V while the former first FER of the bare surface is only faintly observed at 4.8 V. At somewhat below 7 V the dI/dV spectrum shows a doublet with apparent lower peak intensities and broader linewidth.

To gain more insight into the origin and lateral extension of the FERs a series of dI/dV spectra was acquired along a line 3 nm long from the center of the Li cluster towards the bare Cu surface [see Figure 5.3]. Several essential features can be distinguished. New resonances (blue lines in Figure 5.3) appear separated from the FERs of the pristine Cu(100) surface (red lines). These resonances are most prominent on the top of the cluster and disappear gradually when moving away from the cluster, thus showing that the underlying electronic states are localized on the cluster that will be called island localized FERs (ILFERs). Below 7.5 V, when approaching the Li cluster, a shoulder develops a few tenths of Volts below the "parent" FER of the pristine Cu(100) (purple lines). This is more clearly seen for the lowest one at 4.5 V. Upon further approaching the cluster the former shoulder evolves into a narrow well resolved resonance particulary intense at the border of the cluster, as shown in the corresponding dI/dV maps [see Figure 5.4]. However, the original FERs of the pristine Cu(100) surface loose intensity and eventually vanish when approaching the center of the Li cluster. Above 7.5 V the larger width of the FERs does not allow to resolve the shoulder peak from the original FER of the pristine Cu(100) surface, but a shift in the peak position indicates the appearance of the shoulder and disappearance of the original FER, meaning that the behavior is similar as in the lower energy region. The interpretation of the origin of these resonances is given in the next section, once the model used in the theoretical calculations is described [see Figs. 5.9 and 5.10 below].

The spatial extension of the resonances is best seen in dI/dV maps acquired at the peak positions of the resonances on top of the clusters. The dI/dV maps are presented together with the corresponding STM topographs in Figure 5.4. Two main features are observed. There are

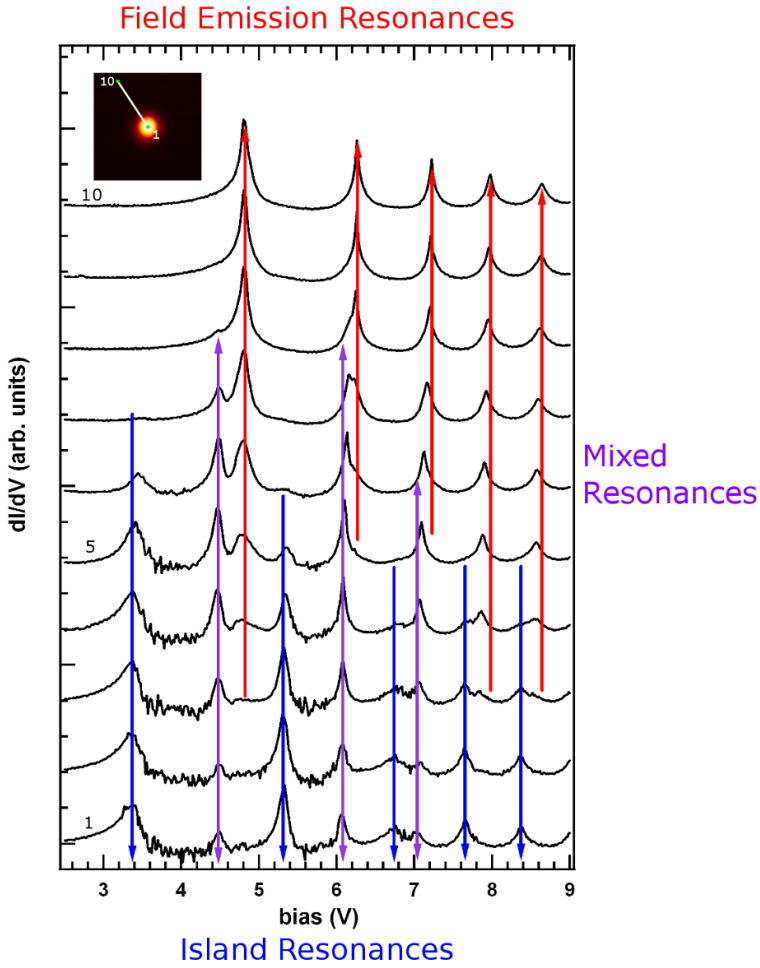

Figure 5.3: dI/dV spectra acquired along a line from the center of the Li cluster (bottom spectrum, labelled 1) to a point of the the Cu surface 3 nm away from the cluster (top spectrum, labelled 10). The evolution from island resonances (in blue) and mixed resonances (in purple) localized on the Li cluster to the original FERs delocalized on the Cu(100) metal surface(in red) can be directly followed in this graph when going from spectrum 1 (higher signal from island resonances) to spectrum 10 (higher signal from field emission resonances) through spectrum 5 (higher signal from mix resonances).

resonances exhibiting a ring shape at 4.4, 6.04 and 6.98 V (purple lines in Figure 5.3), while resonances at 3.34, 5.3 and 6.73 V (blue lines in Figure 5.3) are well localized inside the cluster area. The spatial extension is

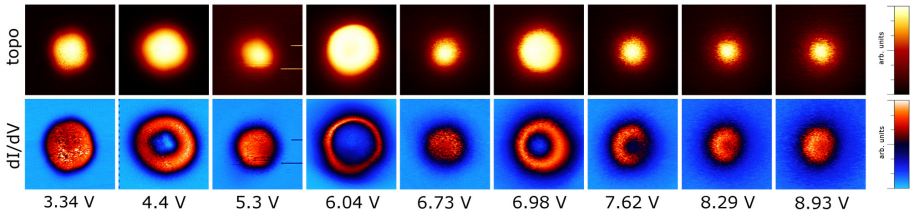

Figure 5.4: STM topographs and corresponding dI/dV maps of an individual Li cluster acquired at the peak positions of the FER observed in spectrum #1 of Fig. 5.3 taken on top of the cluster. Image size: 4.8×4.8 nm^2.

largest for the ring shaped resonances. These states also show the largest topographical features, which differ strongly for the given bias voltages. It is interesting to note, that the rim of the resonances and topographical features is not perfectly circular but rather distorted towards a square structure, in particular for the lower resonances at 3.34 and 4.4 V. The square distortion follows the surface square symmetry. Note, that although the tip-sample distance changes significantly in the dI/dV maps (e.g. $\Delta z = 0.4$ nm at 4.4 V) the position of the FER is rather robust, i.e. the ring shape is not an artifact of the measurement, and it is confirmed in the model calculations [see the central panel in Fig. 5.11]

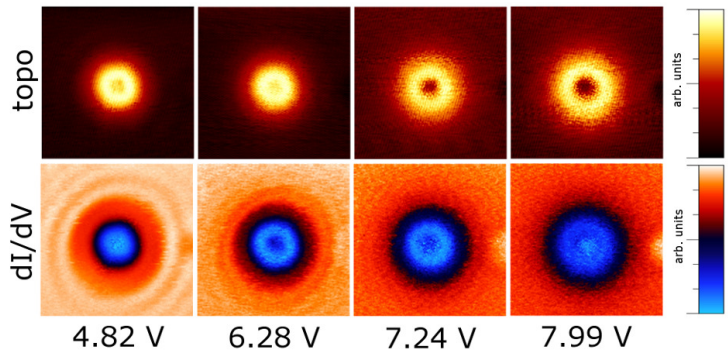

Figure 5.5: dI/dV maps and topographs of a single Li cluster acquired at the peak positions of the unperturbed FER of the bare Cu(100) surface. Image size: 9×9 nm^2.

dI/dV maps at the peak positions of the orignal FERs were also acquired for a single Li cluster and are presented together with their corresponding topographs in Figure 5.5. In the topographs the cluster is imaged with a central depression, i.e., the original FERs are also modified by the presence of the cluster. The dI/dV maps at 4.82 and 6.28 V show

an oscillatory ring pattern around the cluster. This pattern is ascribed to the density modulation created by the scattering of FER electrons at the cluster [5.12].

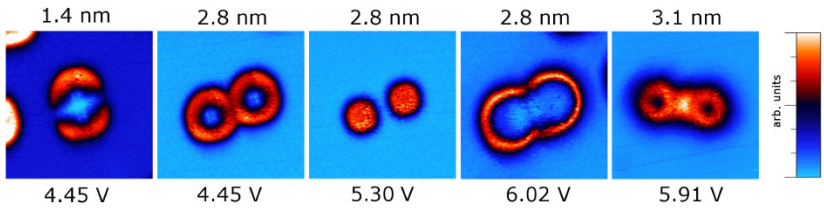

Figure 5.6: dI/dV maps of Li cluster dimers. The distance between the clusters and the bias voltage is given above and below each image, respectively. Image size: 9×9 nm^2.

Besides the localization of FERs at single Li clusters, we have also studied FERs of closely spaced Li clusters. Some examples of dI/dV maps are presented in Figure 5.6. We find that if the clusters are closer than the lateral confinement distance of the resonance on the alkali nanoislands their wavefunctions start to interact, the difference being particularly significant between ring shape resonances and ILFERs (circular patterns). More precisely, the first two dI/dV maps at 4.45 V were acquired for two clusters at a distance of 1.4 and 2.8 nm. The next two were acquired at the same separation 2.8 nm but at two different bias voltage values, 5.3 V and 6.02 V, respectively. The last dI/dV map was taken at a somewhat larger separation distance 3.1 nm and 5.91 V. It is clear that this lateral confinement distance is appreciable larger for the two ring shape resonances at 4.45 V and 6.02 V as compared to the localized ILFER at 5.3 V, no matter whether this latter appears at a higher bias voltage value (5.3 V) than the first one (4.45 V). Therefore, resonances localized on the island (ILFERs) could be seen as "core" states of the cluster, while those at the perimeter as "valence" states, in the sense that these latter start to interact earlier as the two clusters forming the dimer get closer. This could be already anticipated by looking at the dI/dV maps shown in Figure 5.4.

5.3 Theoretical Methods

The main objective of the present theoretical contribution is to explain the physics behind the experimental observations and to draw some conclusions common to all the alkali ad-island structures deposited on the nobel metal surfaces with a projected band gap that, furthermore, can be applied to other kind of nanostructures deposited on metal surfaces. We do not seek to achieve full quantitative agreement with the experiment, since a 3D calculation is required to reproduce the measured dI/dV maps. We, therefore, restrict our study to the cylindrically symmetric case with the tip apex positioned right above the center of an alkali island represented within the cylindrical jellium model. Such an approach strongly reduces the calculation time and, more importantly, allows an unambiguous assignment of the origin of the different resonant structures appearing within each m-symmetry subspace. Here, m is the projection of the angular momentum on the symmetry axis, z. Moreover, as we will show below, only the $m = 0$ intrinsic cluster resonances have a dominant contribution to the experimentally measured spectra. However, the values of the parameters that define the cylindrical jellium model in the present case have to be considered as effective values. Thus, strictly speaking, they do not correspond to measurable quantities. For example, a direct comparison between the observed apparent diameter and local work function change with the ones used in the jellium model is elusive, as the lack of a precise knowledge of the chemical composition mentioned above introduces some uncertainties in the values of these quantities. All in all, we are able to explain the basic trends observed in the experiments using the model system that is described in what follows.

For the description of the system we use the model potential for Na ad-atom islands on Cu(111) developed in Refs. [5.15, 5.16] on the basis of Density Functional Theory (DFT) calculations and adapt it to the present case of Cu(100). To take advantage of our previous work, we consider Na instead of Li islands; note that the most important features of the model are independent of the alkali metal species. With the Cu(111) surface represented by an unscreened model potential [5.19], the DFT calculations performed in Ref. [5.16] yield the island-induced one-electron potential defined as $\Delta U = U^{DFT}_{Na+Cu(111)} - U^{DFT}_{Cu(111)}$. Here $U_{Na+Cu(111)}$ and $U_{Cu(111)}$ are the full (Hartree + exchange-correlation) DFT potentials for the Na nanoisland on Cu(111) and bare Cu(111), respectively. We then construct the model one-electron potential U representative for the alkali-

island on the Cu(100) surface in the presence of the STM-tip as:

$$U(\rho, z) = \Delta U(\rho, z) + U_{Cu(100)}(z) + U_{Tip}(V, z) + U_{abs}(z), \qquad (5.1)$$

where (ρ, φ, z) are the cylindrical coordinates with $z - axis$ perpendicular to the metal surface, going through the center of the island, and corresponding to the axis of the STM tip.

$U_{Cu(100)}(z)$ is the periodic one-dimensional model potential that reproduces the essential features of the projected band structure of the Cu(100) surface at the $\bar{\Gamma}$ point, including the image states [5.19]. The most important one is the projected band gap from about +1.6 eV to +7.8 eV with respect to the Fermi level, that approximately corresponds to - 3 to + 3 eV with respect to the Cu(100) surface vacuum level.

$U_{Tip}(V, z)$ in Eq. 5.1 is the potential due to the presence of the STM-tip, where the dependence on the bias V is explicitly introduced. Since the field emission resonances under study correspond to the high bias case, an electron tunnels not only from the last group of atoms at the tip apex but from its mesoscopic surface. As the lateral extension of the alkali island is typically 1 nm only, the finite radius of curvature of the tip (in the 10 nm range) can be neglected. U_{Tip} is then calculated within the flat tip approximation on the basis of well-tested models [5.11, 5.12]. This allows inclusion of the applied electric field in the tunneling junction and an efficient treatment of the varying tip-sample distance, mandatory to compare with the STS data taken at high bias voltages. Finally, U_{abs} is the imaginary potential introduced inside the metal to account for the inelastic electron-electron scattering events [5.20, 5.21].

Using ΔU obtained for the Cu(111) surface to construct the total potential $U(\rho, z)$ for the present Cu(100) surface case is certainly an approximation; nonetheless, ΔU includes the essential characteristics of the ad-island induced potential: (i) The potential well leading to the ad-island localized electronic states; (ii) Change of the electrostatic potential above the ad-island surface (often referred to as a local work function). As we will see below these are the main ingredients allowing to explain the experimental observations.

Given the potential $U(\rho, z)$, the wave packet propagation technique (WPP) has been applied for the calculation of the energy dependence of the electron transmission coefficients across the tunneling barrier. This allows to obtain the different tunneling characteristics, like current-voltage, conductance-voltage or distance-voltage. In addition, the real space maps

of the electronic wave function at a given energy, as well as the projected density of electronic states (PDOS), can be obtained greatly simplifying the assignment of the resonant states in the metal-nanoisland-tip junction. The details of the WPP method can be found elsewhere [5.22, 5.23]. Here we only give the aspects specific for the present study. In brief, the one-electron wave packet incident from the STM-tip is propagated through the junction by solving the time dependent Schrödinger equation (TDSE). The electronic wave function is represented on a (ρ, z) grid in cylindrical coordinates:

$$\Psi(\rho, \varphi, z, t) = \sum_m \psi_m(\rho, z, t) e^{im\varphi}. \tag{5.2}$$

For the case of cylindrical symmetry considered here m is a good quantum number, so that different m-subspaces are treated independently. Provided the initial conditions $\psi_m(\rho, z, t = 0)$, the time-evolution of $\psi_m(\rho, z, t)$ is given by:

$$\psi_m(\rho, z, t) = e^{-iH_m t} \psi_m(\rho, z, t = 0), \tag{5.3}$$

with an effective Hamiltonian:

$$H_m = -\frac{1}{2}\frac{\partial^2}{\partial z^2} - \frac{1}{2\rho}\frac{\partial}{\partial \rho}\rho\frac{\partial}{\partial \rho} + \frac{m^2}{2\rho^2} + U(\rho, z). \tag{5.4}$$

Equation 5.3 is solved via the short-time propagation with the split-operator technique [5.24, 5.25] as detailed in Refs. [5.22, 5.23]. For a cylindrical tip of radius R_{tip} (typically values $R_{tip} = 6nm$ were used in the cylindrical shape simulation box) the electronic states propagating in forward/backward directions are given by:

$$\chi_{mj}(\rho, z) = \frac{1}{\sqrt{2\pi}} e^{\pm ikz} J_m(\rho X_j^m / R_{tip}) e^{im\varphi}, \tag{5.5}$$

where $J_m(x)$ is the Bessel function of order m and X_j^m is the $j-th$ zero of $J_m(x)$ (different from $x = 0$ for $|m| \neq 0$). The couple (m, j) therefore defines a given asymptotic channel for electron motion inside the tip. The corresponding energy is given by (the $\pm m$ states are degenerate):

$$E_j^m(k) = \left(X_j^m / R_{tip}\right)^2 / 2 + k^2/2. \tag{5.6}$$

We then set the initial wave packet incident from the tip onto the junction (in the negative direction of the z-axis) as follows:

$$\psi_{mj}(\rho, z, t = 0) = \mathrm{e}^{-ik_0 z - (z - z_0^2)/\sigma^2} \; J_m(\rho X_j^m / R_{tip}), \tag{5.7}$$

where the parameters k_0 and σ are chosen in such a way that: (i) The initial wave packet has no overlap with the STM junction, and (ii) The energy spectrum of the initial wave packet covers the energy range of interest.

The tunneling current is determined by the electron transmission matrix from the tip into the substrate. Because of the absorbing potential introduced inside the Cu(100) metal the direct calculation of the transmission coefficient from the WPP is, strictly speaking, not possible, as the flux transferred into the Cu(100) is not preserved. We then proceed as follows. With $\psi_{mj}(\rho, z, t = 0)$ defined by Eq. 5.7 the electron-energy resolved reflection matrix of the junction $\mathbb{R}^m_{j'j}(V, E)$ is obtained within each m-symmetry subspace inside the tip via the "virtual detector method" [5.27] associated to non-reflecting boundary conditions [5.28]. The $\mathbb{R}^m_{j'j}(V, E)$ matrix element gives the probability for an electron incident within the (m, j) channel to be reflected back into the tip within the (m, j') channel. Here we underline the dependence of the scattering properties of the junction on the bias V. From the flux conservation principle the total transmitted flux J^m_j is given by the difference between incident and total reflected flux:

$$J^m_j(E, V) = 1 - \sum_{j'} \mathbb{R}^m_{j'j}(E, V), \tag{5.8}$$

where the summation runs only over the open channels $E \geq \left(X^m_{j'}/R_{tip}\right)^2/2$. Then, the total tunneling flux through the junction at a given energy E is given by:

$$J(E, V) = 2 \sum_{mj} \left(1 - \sum_{j'} \mathbb{R}^m_{j'j}(E, V) \right) , \tag{5.9}$$

where the summation runs only over the open channels and factor 2 stands for the spin statistics. From $J(V, E)$ one obtains the total current $I(V) = \int_{E_F}^{E_F+eV} J(E, V)\, dE$ and so the current-voltage, conductance-voltage or distance-voltage characteristics. E_F is the Fermi level of the Cu(100) so that $E_F + eV$ is the tip Fermi level. Note that we do not account for the modification of the alkali island because of the bias field in the junction. Provided R_{tip} is large enough, i.e., the spectrum of j-states is sufficiently dense, the energy of the different resonant features in the tunneling current converges with respect to R_{tip}. A typical calculation

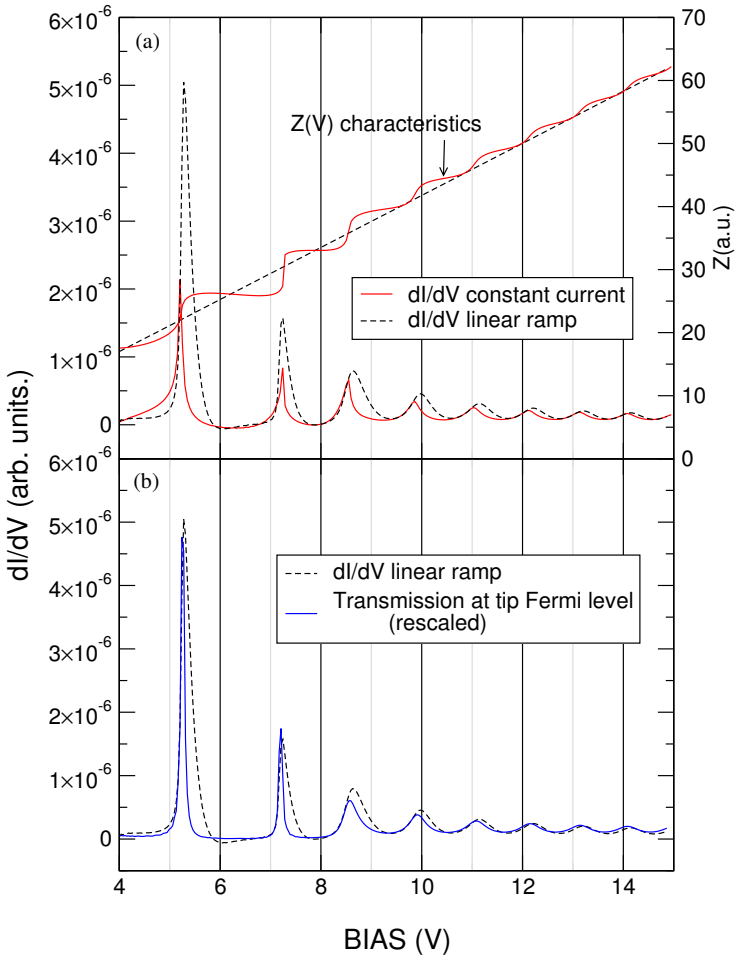

Figure 5.7: (a) Comparison between constant current and linear Z(V) ramp dI/dV spectra for the Cu(100) surface. (b) Comparison between dI/dV(V) and transmission of the junction at the tip Fermi level for the same linear Z(V) ramp. See the text for details.

mesh comprises 500 knots in ρ- and 1024 knots in z- coordinate. The typical propagation time is 4000 a.u. covered in 40000 time steps.

As mentioned in the experimental section, the observed peaks that appear in the differential conductance (dI/dV) point spectra at energies between 3 and 9 eV above the Fermi level correspond to field emission resonances (FER) with different character, i.e., metal- or island-like. In order to identify them in our model calculations, we use the same strategy as in the experiment: compare the point spectra taken on top of the

clean metal surface with the spectra on top of the alkali island. For the clean metal surface the one-dimensional 1D version of the WPP procedure [5.12] has been used.

The calculated constant current distance-voltage characteristic $Z(V)$ shows sharper (energies in the projected band gap) or smoother (energies outside the gap) steps at values V_i that essentially correspond to the different resonance energies $E_i = eV_i$ [see Fig. 5.7 (a)]. To make the computation of the nanoisland dI/dV tractable numerically, we approximate the constant current $Z(V)$ by a linear ramp. The validity of this approximation is assessed in Figure 5.7 where we present the calculated tunneling characteristics for the clean Cu(100) surface. A comparison of the corresponding dI/dV curves, shown in Figure 5.7 (a), permits to conclude that only minor changes in peak positions with some broadening of the peaks (mostly for resonances in the gap) appear. Indeed, this approximation is not only convenient to speed up the calculations, as there is no needed to find the constant current $Z(V)$ characteristic, but also to permit using the same $Z(V)$ to simulate dI/dV curves on top of both the clean metal surface and alkali island. In this way, it is straightforward to identify the character of resonances simply from the peak positions in the spectra, something that cannot be done so accurately in the experiment due to artificial energy shift introduced by the constant current dynamic method of data acquisition.

As one would expect [see Figure 5.7 (b)], the field emission resonances appear equally well in the (dI/dV) curves and in the total transmission at the tip Fermi level [5.12] for a given $Z(V)$. In fact, the presence of resonances in the latter is the reason for the appearance of peaks in the corresponding dI/dV spectrum. We thus end up with several possible ways of doing the resonance analysis: (i) dI/dV curves; (ii) m- resolved transmission at the tip Fermi level: $\mathbb{T}^m(E_F + eV, V) = \sum_j \left(1 - \sum_{j'} \mathbb{R}^m_{j'j}(E_F + eV, V)\right)$; (iii) m- and energy-resolved transmission for the given fixed bias V, and tip-sample distance Z: $\mathbb{T}^m(E, V) = \sum_j \left(1 - \sum_{j'} \mathbb{R}^m_{j'j}(E, V)\right)$; and (iv) Projected Density of States (PDOS) analysis where the resonances (quasi-stationary states) of the junction appear as lorentzian peaks in the energy dependence of PDOS for the given V, Z parameters. Approaches (i) and (ii) are linked with dynamical experimental method, where changing the bias (the energy at which the electronic states of the junction are probed) introduces the energy shift of these very states. Approaches (iii) and (iv) are aimed at finding

all existing resonance states for the given experimental condition i.e. for the given potential of the junction. Observe that, strictly speaking, the quasi-stationary states are the decaying solutions for the given Hamiltonian and, therefore, they are rigorously defined only in these last two cases.

As far as the resonance assignment is concerned, the symmetry considerations appear particularly handy in the present case. The metal-like resonances are delocalized along the surface and have contributions from all m channels, while the (cylindrical) island-localized resonances have well defined m-character. It is worth noting that because of the $m^2/2\rho^2$ centrifugal barrier the number of island-localized states decreases with increasing m and their energy rises [5.16]. The transmission through the island is then fully determined by a limited number of m channels (in practice $m = 0, \pm 1, \pm 2$), as shown in Figure 5.9 [see below].

In Figure 5.8 we show the energy and bias voltage dependence of the density of states PDOS(E, V) along a given linear $Z(V)$ characteristic for the $m = 0$ symmetry subspace. The three panels (a), (b), and (c) correspond to the clean metal Cu(100) surface, the case of d= 1.07 nm and d=1.77 nm alkali nano-islands deposited on Cu(100), respectively, where d is the diameter of the island. The energy position and the widths of the peaks in PDOS(E, V) reflect the energies and widths of the underlying quasi-stationary states which are independent of the choice of the initial state used in the WPP for the PDOS calculation. The intensity of the peaks, on the other hand, is given by the overlap between the resonance wave function and the initial state used in the WPP [5.23].

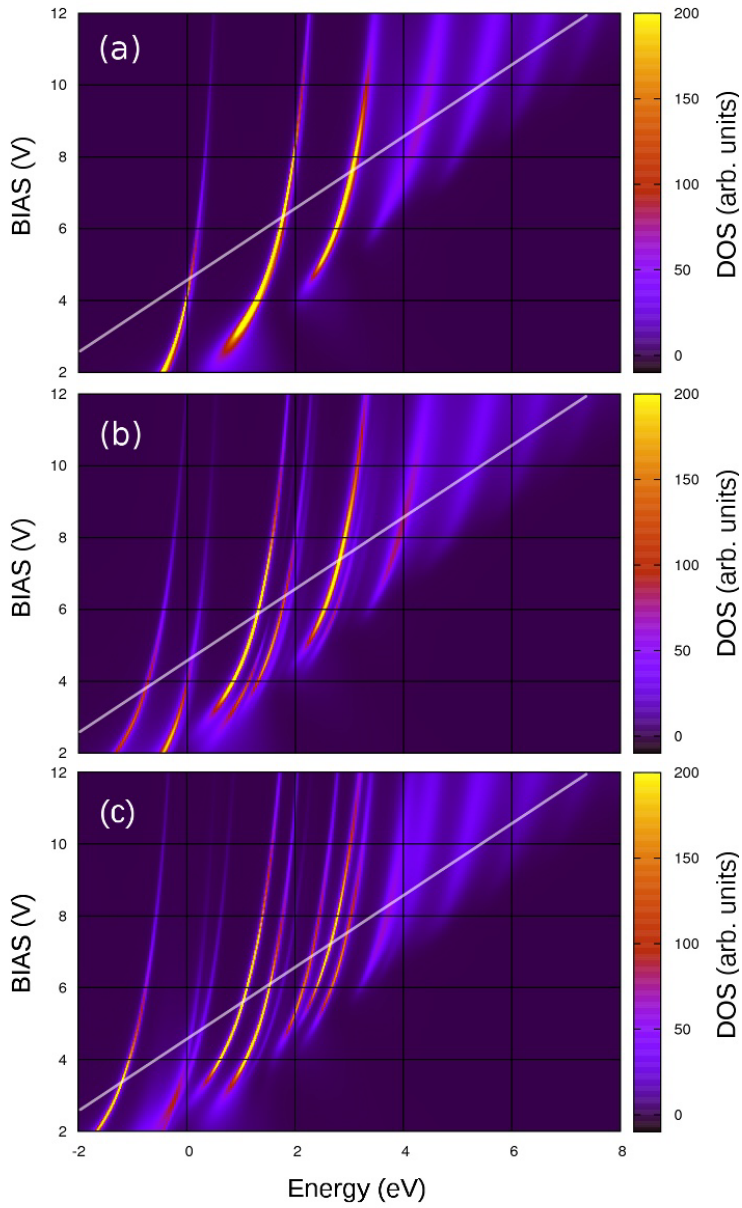

Figure 5.8: Contour plots of the energy (E) and bias voltage V dependence of the m=0 component of the density of states PDOS(E,V) for the clean Cu(100) metal surface (a), and two different diameter (d) alkali islands with d=1.07 nm (b) and d=1.77 nm (c). The energy is measured with respect to the vacuum level of the Cu(100) surface. The use of the same linear Z(V) characteristic in both cases permits a direct identification of the first island-like resonances as additional lines to the clean metal FERs. The white oblique straight lines are defined by the linear E(V)= eV - W relation, where W is the Cu(100) work function (4.6 eV).

A simple comparison between the clean surface [panel (a)] and ad-island results [panels (b) and (c)] allows one to assign the different resonances (in particular to reveal the island-localized states) and their evolution upon the change of the experimental conditions. Thus, the additional bright lines that appear in the calculated PDOS(E, V) for the island on top of the metal surface [panels (b) and (c)] correspond to island induced states whose energies are not very close to the other FERs, as compared to their width. These well resolved sharp resonances are then located approximately between -3 to +3 eV with respect to the Cu(100) surface vacuum level (+1.6 and +7.8 eV above the Cu(100) Fermi level), i.e., in the projected band gap at $\bar{\Gamma}$. As the energy is raised above the projected band gap the lifetimes of the resonances are appreciably reduced because of the efficient decay via an electron escape into the metal. Only broad overlapping features are then observed in agreement with experimental data.

Before entering a detailed discussion that includes the assignment of the different resonant states, let us first present some basic considerations relying on the general properties of nano-size alkali adislands. Indeed, the complex resonance pattern observed in this study calls for a guiding line allowing one to have a better understanding of the data. As follows from previous works [5.15, 5.16], in the absence of the STM tip the attractive potential associated with alkali ad-island is sufficiently strong to lead to a series of island-induced quasi-stationary electronic states. The finite lifetime of these states is due to the coupling with the substrate which enables population decay. The lowest energy resonances are well localized inside the island and correspond to the quantum well state (QWS) of the complete alkali overlayer quantized by the island boundaries. Within the $m = 0$ symmetry, each following ℓ state develops an additional zero in the wave function structure along the island, i.e., in the ρ direction. Because of their large binding energies the QWSs do not appear in the energy range relevant for the present study of the FERs. In addition to the QWS, the image-potential-like (ISs) states localized in front of the island were reported [5.16]. The lowest n ISs are pinned to the local vacuum level in front of the island. Here n is the quantum number of the IS linked with the nodal structure perpendicular to the island surface. As n grows an electron moves far enough from the island to "probe" the finite size of the latter and the finite range of the associated attractive dipole. The high n states then merge into the series of the ISs of the substrate. The same as for the QWS, for fixed symmetry and quantum number n a series

of states is formed. Each next state develops an additional zero in the ρ-direction because of the quantization by reflection at island boundaries. Thus, the image-potential-like states localized in front of the island are characterized by the two, n and ℓ , quantum numbers. n corresponds to the quantization of the electron motion perpendicular to the surface in the z-direction, similarly to the conventional ISs of the pristine metal surface, while ℓ reflects the nodal structure in the ρ-direction parallel to the surface. Importantly, the lifetime of the resonances with given n rapidly decreases with increasing energy (ℓ quantum number). This is linked with an energy dependence of the electron escape through the island boundaries [5.13–5.16], and it also explains why only a limited number of states could be observed.

When the bias is applied to the STM junction, the corresponding electric field overrides the image potential so that the ISs evolve into the states of the linear ramp potential, i.e., FERs. They can be considered as Stark-shifted ISs. We thus expect several types of resonances to be formed in the present system:

(i) The modified FERs of the pristine Cu(100) surface with energies equal to that of the island-free case, and wave-function structure in the ρ direction modified by the scattering at the island boundaries. Since these states are delocalized along the surface they form a 2D continuum characterized by the quantum number n and parabolic energy dispersion $E_n(V, k_{||}) = E_n(V) + k_{||}^2/2m^*$. $E_n(V)$ is the energy of the FER at $\bar{\Gamma}$, and $k_{||}$ is the electron momentum parallel to the surface. Within the model potential for Cu(100) [5.19] that we use, the effective mass is $m^* = 1$.

(ii) Non-dispersing FERs bound by the attractive potential well in front of the island and evolving from the island localized ISs. These states are characterized by the two quantum numbers n and ℓ reflecting the nodal structure perpendicular and parallel to the island surface, respectively. By analogy with island-localized image states one can expect that the energies of the island localized FERs can be approximated by [5.16]:

$$E_{n\ell}^m(V) = E_n(V) + \left(X_\ell^m/R\right)^2/2, \tag{5.10}$$

where R is the radius of the island and X_ℓ^m is the zero of the corresponding Bessel function. $E_n(V)$ accounts for the local change of the work function above the island, and the second term corresponds to the quantization by scattering at island boundaries. It is noteworthy that for large enough

island radius ($R \to \infty$) $E_n(V)$ converges to the $\bar{\Gamma}$ energies of the FERs of the Cu(100) surface with a complete alkali overlayer.

(iii) Finally, the attractive potential of the alkali island should lead to the localization of the 2D Cu(100) FERs. Similar to the surface state or image state localization by an attractive adatom potential [5.29–5.32], we expect the non-dispersive component of these resonances to appear below the bottom of the 2D continuum for each split Cu(100) field-emission resonance. When close in energy, states (ii) and (iii) can experience an avoided crossing with mixing of their character.

We are now in a position to assign the character of the different resonant structures appearing in Figure 5.8. We will focus on the large alkali nano-islands [panel (c)] for which the energy position of the different resonances matches rather well the observed ones. The radial size of the ad-island is an important parameter since, as follows from Eq. 5.10, it determines the characteristic energy scale for the ρ quantization, i.e., the energy separation and the number of the island-localized FERs characterized by the same quantum number n and varying ℓ.

In order to directly connect between the calculated data and the experimentally measured dI/dV spectra we show in Figure 5.9 the m- resolved transmission at the tip Fermi level:

$$\mathbb{T}^m(E_F + eV, V) = \sum_j \left(1 - \sum_{j'} \mathbb{R}^m_{j'j}(E_F + eV, V) \right) \tag{5.11}$$

for the $m = 0$ and $m = 1$ symmetry subspaces. The results for the clean Cu(100) surface are compared with the alkali nano-island case along the same distance-voltage characteristic $Z(V)$. Basically, the peak positions reported in Figure 5.9 correspond to the cut of the 2D plots of the energy and bias voltage dependence of the projected density of states (Fig. 5.8) along the straight lines shown in white color in Figure 5.8.

Consistent with the delocalized character of the FERs of the Cu(100) surface, their energies at $\bar{\Gamma}$ are independent of m (see grey vertical lines in Figure 5.9). We label these resonances as FER$_n$ according to their quantum number (n=1,2, ...). Because of the flat tip approximation and the same distance-voltage characteristic $Z(V)$ used both for the clean surface and ad-island, the FERs of the Cu(100) surface are also present in ad-island case. They correspond to the electron tunneling from the tip into the surface area outside the alkali-island, and provide a good

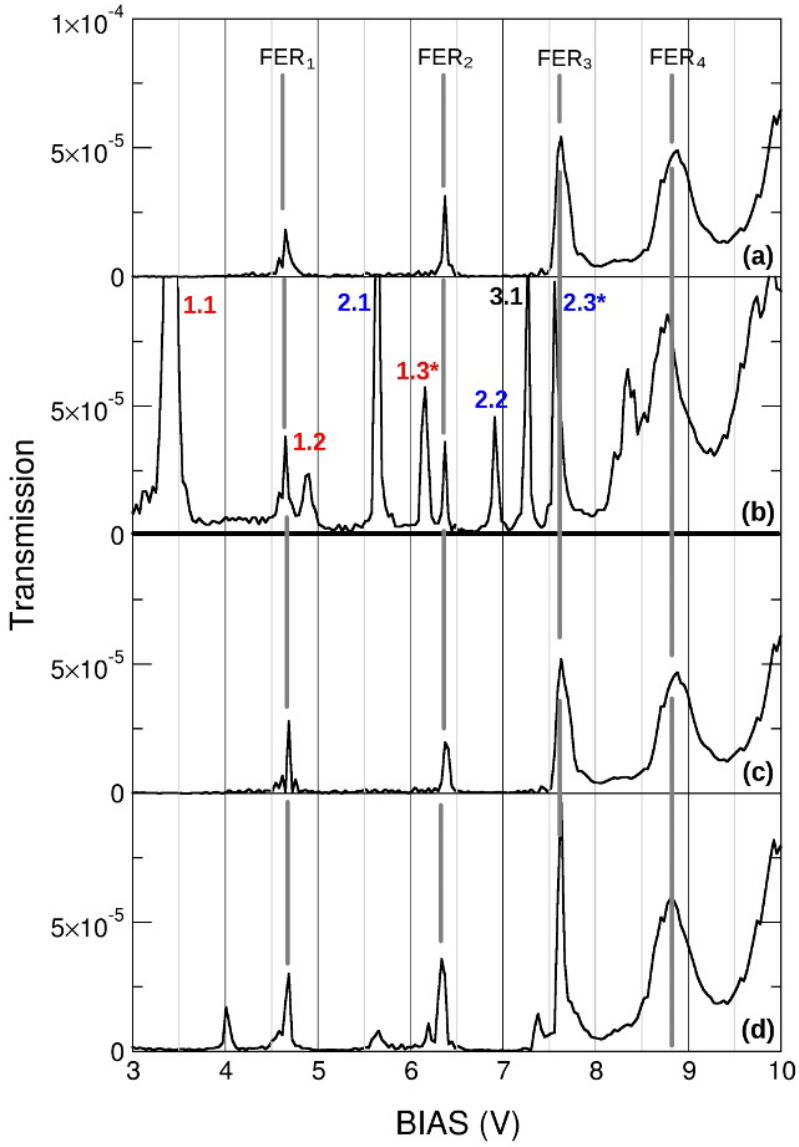

Figure 5.9: Calculated bias voltage dependence of the transmission at the tip Fermi level $\mathbb{T}^m(E_F + eV, V)$ decomposed in its $m = 0$ [panels a) and b)] and $m = 1$ [panels c) and d)] components. Results for d= 1.77 nm diameter alkali island on Cu(100)[panels b) and d)] are presented together with results obtained for the pristine Cu(100) surface [panels a) and c)]. The island resonances are labeled using the (n, ℓ) quantum numbers that refer to the number of nodes in the wave function along the perpendicular $(n-1)$ z-axis or the radial $(\ell - 1)$ ρ-axis

reference for observation of the island-specific features. The emergence of the island-localized states is particularly apparent within the 2 to 8 V bias range when the resonances fall into the projected band gap of Cu(100) and thus posses a long lifetime, i.e., they are sharp and well resolved. For higher bias, only broad structures can be observed because of the strong coupling with projected bulk bands [5.33]. The island induced resonances are labeled according to their n (principal) and ℓ (radial) quantum numbers, where the assignment of the states is explained below.

The calculated transmission curves allow us to draw an important conclusion: not all the resonances will contribute to the experimentally observed signal. As far as the island states are concerned, the transmission is significant for the $m = 0$ subspace only. An electron in this case tunnels from the tip into the surface along the surface normal going through the center of the ad-island, i.e. along the lowest potential energy path. For $|m| = 1$, the centrifugal barrier prevents the electrons to approach the quantization $z-axis$. The overall decrease of $\mathbb{T}^m(E_F+eV, V)$ with increasing m is even more pronounced for $|m| \geq 2$ subspaces (not shown). The $m = 0$ resonances will then mainly determine the tunneling current. Furthermore, within the $m = 0$ subspace, several island-localized states dominate the $\mathbb{T}^m(E_F + eV, V)$ and, in this way, they should give the highest contrast in the experimental dI/dV maps. These are the (n,ℓ=1) resonances located at 3.4, 5.7 and 7.3 Volts below the corresponding FER_n of the pristine Cu(100) surface. They are identified with the observed resonances at 3.3, 5.3 and 6.7 Volts [see Figs. 5.4 and 5.5].

The (n, ℓ) assignment of the resonant structures is done based on the spatial distribution of the corresponding electronic wave functions $\xi^m_{n\ell}$ extracted from the WPP and shown in Figure 5.10. The panels of Figure 5.10 represent the one-electron charge density $|\xi^m_{n\ell}|^2$ in cylindrical (ρ, z) coordinates with z-axis pointing from the Cu(100) surface into the STM tip. The tip corresponds to a region with a high density parallel to the ρ-axis at the top of each panel. The large probability of the electron presence inside the tip results from the choice of the initial conditions with electrons incident at the junction from the flat tip. Observe also the tip retraction for higher energy states. The oscillatory structure of the wave functions inside Cu(100) reflects the periodicity of the Cu(100) planes in z-direction. The states presented in Figure 5.10 have their energies in the projected band gap of the substrate. The electron density is then exponentially damped into the metal, i.e. an electron propagation along the surface normal is impossible.

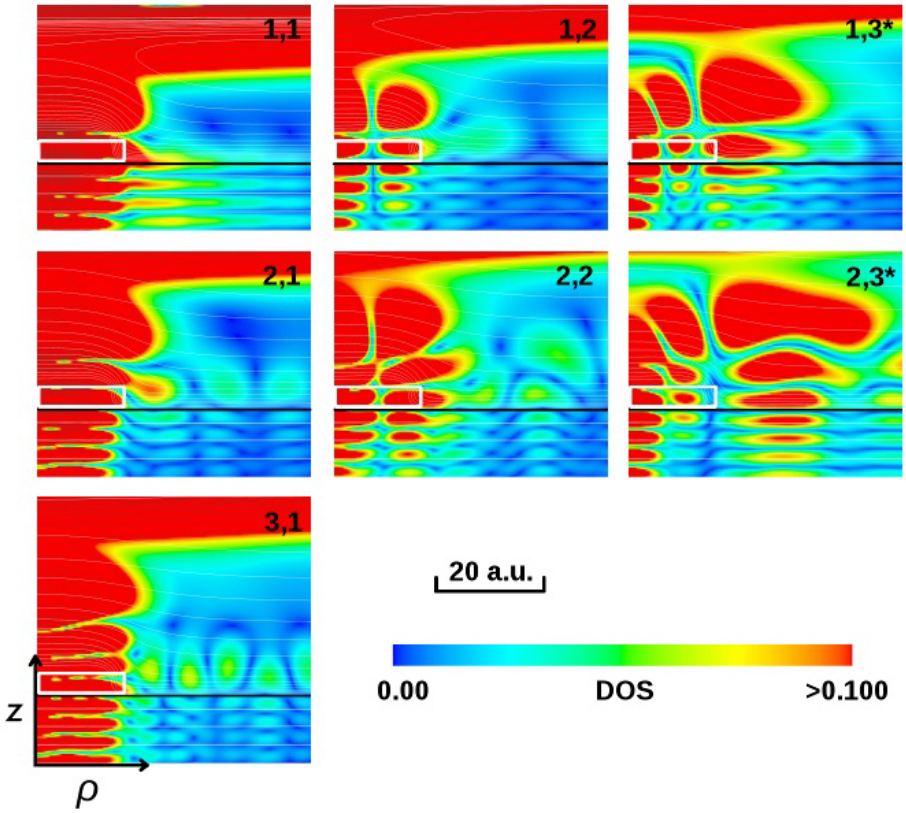

Figure 5.10: Two dimensional plots of the electronic density of the island-localized FERs for 1.77 nm diameter alkali island on Cu(100). Results are presented as a function of the z and ρ cylindrical coordinates. The color code is explained in the insert of the figure. The labeling of resonances according to their n, ℓ quantum numbers is the same as in Figure 5.9. The z axis runs from the Cu(100) surface (negative z) into the tip (positive z). The thin horizontal line gives the position of the Cu(100) image plane. The cluster is schematically sketched by the white rectangle.

The island-induced FERs appear confined to the island area both in ρ and z directions in the vacuum side between the island and the tip. The overlap between the electronic densities of the island localized state and the tip reflects the strength of the island-tip coupling and thus the transmission (tunneling current). As discussed above the n and ℓ quantum numbers define the nodal structure of the island-localized states in the z-direction above the island and in the ρ-direction along the island, respectively. Thus, the lowest energy transmission resonance (1,1) at 3.4 eV as it appears within the $m = 0$ subspace in Figure 5.9 shows no nodes in ρ and a node in z at the island surface. A comparison with the wave functions of the nanosized alkali island localized image states [5.16] allows an assignment as the (n=1, ℓ=1) island-localized field-emission resonance (ILFER) that develops from the (n=1, ℓ=1) island-localized image state. The states with additional nodes appearing in z direction between the tip and the island and no nodes in ρ can be assigned as (n=2, ℓ=1) (one additional node) and (n=3, ℓ=1) (two additional nodes) ILFERs. Increasing n is associated with the spread of the electronic density farther into the vacuum as far as z-behavior is concerned. We observe that the radial shape is very similar for this group of states. The states characterized by additional nodes in radial direction can be assigned as (n=1, ℓ=2) and (n=2, ℓ=2) ILFERs depending on the nodal structure in z. Thus, when far in energy from the FERs of the Cu(100) surface, the alkali-island induced states indeed reflect the confinement properties reported in Ref. [5.16] with energies following the trends given by Eq. 5.10. The $\ell = 1$ states give the most prominent transmission resonances because of their node-less structure along the surface of the island that favors the coupling with the tip as clearly seen in the corresponding panels of Figure 5.10. The $n = 1, 2, 3, \ell = 1$ resonances have energies below the FERs of the Cu(100) surface characterized by the same n. This energy downshift results from the attractive potential of the alkali nanoisland that can be seen as local reduction of the work-function of the surface. The higher the quantum number n of the ILFER is, the larger the distances from the island surface "probed by an electron are. Then, the local effect decreases and the energies of the ILFER approach these of the Cu(100) FERs.

While (n=1,2,3, ℓ=1,2) states are well confined in the radial ρ direction to the area of the island, the (n=1, ℓ=3*) and (n=2, ℓ=3*) resonances show quite different spatial extension in the ρ coordinate. The electron density spreads along the surface well outside the island area.

Moreover, while the inner part within the island area shows the same z-dependence as $\ell = 1$ and $\ell = 2$ resonances, the outer ρ lobe of the wave function has essentially larger extension into the vacuum favoring the coupling with an STM-tip. The ℓ=3* states give then the second highest contribution to the transmission after the $\ell = 1$ resonances. We attribute this particular shape of the ℓ=3* ILFERs to their origin as the mixed states resulting from the coupling between (i) the island-like (n, ℓ=3) states of the given ℓ series defined by the principle quantum number n and (ii) the 2D localized state splitted from the FER_{n+1} of the Cu(100) surface.

As we have discussed earlier in this section the FERs of the Cu(100) surface correspond to the 2D continuum of electronic states propagating along the surface and confined in the direction perpendicular to the surface. According to Simon's theorem [5.34], any attractive potential in 2D has a bound state. This is exactly the case of the alkali adisland since it creates an attractive potential well. Then one might expect to have a bound state below each 2D FER_n continuum with a z dependence of the electron wave function being the same as that of the parent FER_n state, but localized in ρ. The 2D localization by adatoms has been reported for the surface states as well as for the image potential states [5.29–5.32]. A similar effect has been observed in the splitting of bands when an attractive periodic potential with hexagonal symmetry perturbs the originally quasi-free electron like bands in rippled graphene [5.35] or in optical lattices trapping cold atoms [5.36]. The radial extension of the 2D localized states depends on their energy with respect to the bottom of the corresponding parent continuum and usually it is quite large. In Figure 5.9 one observes that at $\bar{\Gamma}$ the (n, ℓ=3*) transmission resonances are located just below the FER_{n+1} of the pristine Cu(100) surface, i.e. exactly in the energy region where one would expect the existence of the 2D localized state splitted from the FER_{n+1} continuum. Thus, the $(n, \ell{=}3)$ field emission resonance of the "pure" island nature corresponding to the ℓ series given by Eq. 5.10 and confined to the island will mix with the 2D localized FER_{n+1} of Cu(100), with larger ρ extension. We use the star in labeling the issuing resonances to underline their "mixed" nature as compared to the "pure" island states. The mixing between the states would also explain the particular shape of the z dependence with electron density more spread into the vacuum outside the island area and reflecting that of the 2D localized FER_{n+1}. Indeed, since the energy of the Cu(100) FER_{n+1} is higher than $E_n^{m=0}(V)$ of the "pure" island series

(see Eq. 5.10) it is more extended in z. Observe that for this reason the coupling between the STM-tip and the (n, ℓ=3*) states is strongest not at the center of the island, but at the ring surrounding the island.

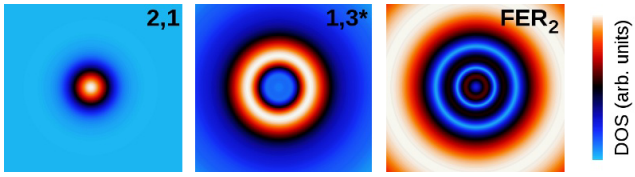

Figure 5.11: Two-dimensional (x, y) cuts in a plane parallel to the surface at about half way between the tip and the sample of the full three dimensional charge densities at three representative selected bias voltage values (V=5.7, 6.1 and 6.4 Volts) corresponding to an island-like (n=2, ℓ=1), mix (n=1, ℓ=3*) and metal-like resonances (FER_2), respectively.

In Figure 5.11 we show the two-dimensional (x, y) cuts of the charge density in a plane parallel to the surface at z corresponding to about half distance between the tip and the sample. The three panels correspond to the bias voltage values at which the island-like ($n = 2, \ell$=1), mix ($n = 1, \ell$=3*) and metal-like FER_2 resonances are observed within the $m = 0$ subspace in Figure 5.9. Provided that the dominant contribution to the transmission comes from the $m = 0$ symmetry, the calculated results can be compared with experimentally measured dI/dV maps [see Figs. 5.4 and 5.5] revealing striking resemblance. It should be understood, however, that there are essential differences between measured dI/dV maps and simulated charge densities: (i) the m-character of intrinsic island resonances is not resolved in the experiments; (ii) the measured dI/dV maps correspond to constant current scans, while the calculated wave patterns simply show the real space charge distribution of the resonances; (iii) the simulations were performed with $Z(V)$ characteristic obtained for the pristine Cu(100) surface and so neglecting the possible change in $Z(V)$ because of the presence of the island; finally (iv) the constant current mode of measurement introduces a rapid variation of the tip sample distance Z at the critical voltage values V_n for resonances with energy $E_n = eV_n$ in the projected gap seen as steps in the $Z(V)$ characteristic, contrary to the constant field case of the linear $Z(V)$ ramp used in model calculations.

Keeping in mind the words of caution above, the calculated results closely match the experimental observations. Consistent with Figure 5.10, the island-induced ($n = 2, \ell$=1) resonance appears as a bright spot confined in the island area. It is followed by the mixed ($n = 1, \ell$=3*) res-

onance appearing as a bright ring surrounding the island and extending outside its area. Finally, for the metal-like FER_2 resonance of the Cu(100) surface, the electrons are repelled from the island area because of the orthogonality constraint with respect to the island-localized states including the mix resonance. The island then appears as depletion which is fully confirmed by the experiment.

5.4 Summary

We have presented a low-temperature scanning tunnelling spectroscopy study of FERs of alkali metal clusters on Cu(100). Isolated clusters present a complex FER spectrum composed of localized resonances intrinsic to the clusters together with resonances arising from 2D localization of the substrate FERs around the clusters, which can mix with each other if sufficiently close in energy. Two-dimensional dI/dV maps reveal the spatial extension of the different type of FERs, showing that cluster-like FERs are localized at the center of the alkali islands whereas substrate related FERs form ring-shaped structures at the island boundaries. dI/dV maps taken on cluster dimers show that localized FERs hybridization occurs for dimers formed by approaching two clusters to each other, as long as the separation distance is short enough. This distance depends on the kind of resonance (mix or ILFER), being shorter for ILFERs as compared to mix resonances.

Based on the comparison between experimental data and results of model calculation we can formulate the following general rule: starting from the lowest $(n = 1, \ell{=}1)$ resonance, the island-induced resonances of island-like $(n, \ell{=}1)$ character give the main peaks in the transmission and experimental dI/dV spectra at the energies comprised between FER_{n-1} and FER_n of Cu(100). The corresponding dI/dV maps show bright spots spatially confined to the island area. Further prominent peaks in the transmission alternating with $(n, \ell{=}1)$-ones correspond to the mixed resonances originating from the composition of (n, ℓ) series of the island-localized image states (here $\ell{=}3^*$) and 2D-localized state split from the FER_{n+1} of the pristine Cu(100) surface. The corresponding dI/dV maps at resonance energies are expected to show a bright ring surrounding the island and extending outside its area. This theoretical prediction is consistent with our experimental data, for bias voltages within the projected band gap of Cu(100). The states observed outside this bias voltage range

are so broadened by the coupling with Cu(100) bulk bands that a clear cut definition of their character is no longer possible. Along the same lines, recent work of K. Schouteden and C. Van Haesendonck [5.37] addressed the island induced resonances for large Co islands on Au(111). The large width of the resonances above the top of the projected band gap (+3.6 eV with respect to the Fermi level) precludes observation of the split-off states so that only pure island-like resonances [the $(n, \ell{=}1)$ - series] and field emission resonances [the FER_n series] of the Au(111) surface could be observed.

How robust are the present results and how representative are the calculations performed for Na nanoislands to interpret the experimental case of Li nanoislands? In order to answer this question let us list the most important ingredients of the present theoretical explanation of the experimental data.

1. The island-localized FERs form a series that can be seen as a quantization of the FERs of the complete alkali overlayer by the island boundaries. For the cylindrical island structure these states are characterized by the magnetic quantum number m, vertical (principal) quantum number n and radial quantum number ℓ as given by Equation 5.10.

2. Because of the centrifugal barrier, $m = 0$ states give dominant contribution to the transmission and thus to the tunneling current.

3. The alkali nanoisland creates an attractive potential well. As a result, for fixed quantum number n, the $E_{n\ell}^{m=0}(V)$ series of the island-localized states starts with $\ell = 1$ well below the FER_n continuum of the substrate metal surface.

4. The attractive potential well due to the alkali nanoisland leads to the 2D localization of the FERs of the substrate metal surface. Thus, the 2D localized state is formed below the bottom of the corresponding continuum of the "parent" FER_n at $\bar{\Gamma}$. Contrary to the "pure" island-like states, the 2D localized FERs have spatial extension along the surface that is essentially larger than the island area.

5. When close in energy, the island-like states (n,$\ell \geq 2$) hybridize with 2D localized FERs with principal quantum number $n' > n$ leading to the formation of mixed states.

6. Because of their spatial extension the island-like (n,$\ell = 1$) states and the mix states give the main contribution to the tunneling current.

7. Consistent with electronic density profiles, the island-like (n,$\ell = 1$) states are predicted to appear in dI/dV maps as bright spots confined to the island area. The mixed states should appear as a ring structures extending outside the island in the direction parallel to the surface.

8. The different character of resonances is well resolved only for the bias values such that the states fall into the projected band gap of the substrate. Outside this range the structures are too broad because of the fast electron escape into the bulk metal.

The points listed above are not specific for a given 2D nanostructure and substrate. Their common underpinning is the fact that the work function of the nanostructure is lower than the work function of the substrate so that it creates an attractive potential well. Thus, the present theoretical conclusions are robust and not specific for the Cu(100) substrate and Na nanoislands modelled within the free-electron (jellium) approximation as here. We argue that similar results should be obtained for a variety of ad-island/substrate systems (including periodic arrays) whenever the spatial variations of the work-function (substrate and adsorbate) are sufficiently large, and when the substrate posses a band gap in the surface projected electronic structure that contains the vacuum level, allowing for the series of FERs to be resolved.

5.5 Acknowledgments

We acknowledge partial financial support from the European Research Council (StG 203239), the Spanish Ministerio de Ciencia e Innovación (MAT2010-15659 and FIS2010-19609-C02-01), the Basque Government-University of the Basque Country G.V.-UPV/EHU (IT-366-07) and the Catalan Agència de Gestió d'Ajuts Universitaris i de Recerca (2009 SGR 695).

5.6 References

[5.1] G. Binnig, K. H. Frank, H. Fuchs, N. Garcia, B. Reihl, H. Rohrer, F. Salvan, and A. R. Williams, Phys. Rev. Lett. 55, 991 (1985); R. S. Becker, J. A. Golovchenko, and B. S. Swartzentruber, Phys. Rev. Lett. **55**, 987 (1985).

[5.2] J. A. Kubby, Y. R. Wang, and W. J. Greene, Phys. Rev. Lett. **65**, 2165 (1990).

[5.3] T. Jung, Y.W. Mo, and F.J. Himpsel, , Phys. Rev. Lett. **74**, 1641-1644 (1995).

[5.4] M. Pivetta, F. Patthey, M. Stengel, A. Baldereschi, and W.-D. Schneider, Phys. Rev. B **72**, 115404-1-6 (2005).

[5.5] Hans-Christoph Ploigt, Christophe Brun, Marina Pivetta, François Patthey, and Wolf-Dieter Schneider, Phys. Rev. B **76**, 195404-1-5 (2007).

[5.6] C. L. Lin, S. M. Lu, W. B. Su, H. T. Shih, B. F. Wu, Y. D. Yao, C. S. Chang, and Tien T. Tsong, Phys. Rev. Lett. **99**, 216103 (2007).

[5.7] P. Ruffieux, K. Aït-Mansour, A. Bendounan, R. Fasel, L. Patthey, P. Gröning, and O. Gröning, Phys. Rev. Lett. **102**, 086807 (2009).

[5.8] J. Li, W. D. Schneider, R. Berndt, and S. Crampin, Phys. Rev. Lett. **80**, 3332 (1998).

[5.9] J. Lagoute, X. Liu, and S. Fölsch, Phys. Rev. Lett. **95**, 136801 (2005).

[5.10] M. Feng, J. Zhao, H. Petek, Science **320**, 359 (2008).

[5.11] J. M. Pitarke, F. Flores, and P. M. Echenique, Surf. Sci. **234**, 1 (1990).

[5.12] J. I. Pascual, C. Corriol, G. Ceballos, I. Aldazabal, H.-P. Rust, K. Horn, J. M. Pitarke, P. M. Echenique, and A. Arnau,, Phys. Rev. B**75** 165326 (2007).

[5.13] S. Crampin, H. Jensen, J. Kröger, L. Limot, R. Berndt, Phys. Rev. B **72**, 035443 (2005).

[5.14] J. Kröger, L. Limot, H. Jensen, R. Berndt, S. Crampin, E. Pehlke, Prog. Surf. Sci. **80**, 26-48 (2005).

[5.15] T. Hakala, M. J. Puska, A. G. Borisov, V. M. Silkin, N. Zabala, and E. V. Chulkov, Phys. Rev. B **75**, 165419 (2007).

[5.16] A. G. Borisov, T. Hakala, M. J. Puska, V. M. Silkin, N. Zabala, and E. V. Chulkov, P. M. Echenique, Phys. Rev. B **76**, 121402(R) (2007).

[5.17] R. D. Diehl and R. McGrath, Surf. Sci. Reports **23**, 43 (1996).

[5.18] I. Ohsaki and T. Oguchi, Surf. Sci. **438**, 26 (1999).

[5.19] E. V. Chulkov, V. M. Silkin, and P. M. Echenique, Surf. Sci. **437** , 330 (1999).

[5.20] J. B. Pendry, Low Energy Electron Diffraction (Academic, London, 1974).

[5.21] R. García, J. J. Sáenz, J. M. Soler, and N. García, Surf. Sci. **181**, 69 (1987).

[5.22] A. G. Borisov, A. K. Kazansky, and J. P. Gauyacq, Phys. Rev. Lett. **80**, 1996 (1998); Phys. Rev. B **59**, 10 935 (1999); Surf. Sci. **430**, 165 (1999).

[5.23] E. V. Chulkov, A. G. Borisov, J. P. Gauyacq, D. Sánchez-Portal, V. M. Silkin, V. P. Zhukov, and P. M. Echenique, Chem. Rev. **106**, 4160 (2006).

[5.24] M. D. Feit, J. A. Fleck Jr., A. Steiger, J. Comput. Phys. **47**, 412 (1982).

[5.25] C. Leforestier, R. H. Bisseling, C. Cerjan, M. D. Feit, R. Friesner, A. Guldberg, A. Hammerich, G. Jolicard, W. Karrlein, H. D. Meyer, N. Lipkin, O. Roncero, R. Kosloff, J. Comput. Phys. **94**, 59 (1991).

[5.26] A. G. Borisov, E. V. Chulkov, and P. M. Echenique, Phys. Rev. B **73**, 073402 (2006).

[5.27] J. Sjakste, A. G. Borisov, J. P. Gauyacq, and A. K. Kazansky, J. Phys. B: At. Mol. Opt. Phys. **37**, 1593 (2004).

[5.28] D. Kosloff, R. Kosloff, J. Comput. Phys. **52**, 35 (1983).

[5.29] F. E. Olsson, M. Persson, A. G. Borisov, J.-P. Gauyacq, J. Lagoute, and S. Fölsch, Phys. Rev. Lett. **93**, 206803 (2004).

[5.30] L. Limot, E. Pehlke, J. Kröger, and R. Berndt, Phys. Rev. Lett. **94**, 036805 (2005).

[5.31] V.S. Stepanyuk, A.N. Klavsyuk, L. Niebergall, P. Bruno, Phys. Rev. B **72**, 153407 (2005).

[5.32] A. G. Borisov, A. K. Kazansky, J. P. Gauyacq, Phys. Rev. B **65**, 205414 (2002).

[5.33] C. Corriol, V. M. Silkin, D. Sánchez-Portal, A. Arnau, E. V. Chulkov, P. M. Echenique, T. von Hofe, J. Kliewer, J. Kröger, and R. Berndt, Phys. Rev. Lett. **95**, 176802 (2005).

[5.34] B. Simon, Ann. Phys. (N.Y.) **97**, 279 (1976).

[5.35] B. Borca, S. Barja, M. Garnica, D. Sánchez-Portal, V.M. Silkin, E.V. Chulkov, F. Hermanns, J.J. Hinarejos, A.L. Vázquez de Parga, A. Arnau, P.M. Echenique, and R. Miranda, Phys. Rev. Lett. **105**, 036804(2010).

[5.36] B. Wunsch, F. Guinea, and F. Sols, New J. Phys. **10**, 103027 (2008).

[5.37] K. Schouteden and C. Van Haesendonck, Phys. Rev. Lett. **103**, 266805 (2009).

Part III

Laser induced electron emissions in metals

Chapter 6

Study of the induced potential produced by ultrashort pulses on metal surfaces

Published as M. N. Faraggi, I. Aldazabal, M. S. Gravielle, A. Arnau and V. M. Silkin in J. Opt.Soc. Am B **26** (12), 2331 (2009).

Abstract

The influence of the induced potential on photoelectron emission from metal surfaces is studied for grazing incidence of ultra short laser pulses. To describe this process we introduce a distorted wave-method, the Surface Jellium-Volkov approach, which includes the perturbation on the emitted electron produced by both the laser and the induced fields. The method is applied to an Al(111) surface contrasting the results with the numerical solution to the time-dependent Schrödinger equation (TDSE). We found that SJV approach reproduces well the main features of emission spectra, accounting properly for effects originated by the induced potential.

PACS: 79.60.-i, 78.70.-g

DOI: 10.1364/JOSAB.26.002331

6.1 Introduction

In the past few years developments in laser technology have made it possible to produce laser pulses with durations in the sub-femtosecond scale [6.1–6.5]. This advance in the experimental area opens up new branches in the research of the matter-radiation system [6.6–6.10]. In particular, the investigation of photoelectron emission from surfaces due to incidence of short laser pulses gives the chance to understand a piece of the complicated puzzle corresponding to electron dynamics at metal surfaces.

In this article we investigate the photoelectron emission produced when an ultrashort laser pulse impinges grazingly on a metal surface, focusing the attention on the role played by the surface induced potential. The induced potential is caused by the rearrangement of valence-band electrons due to the presence of the external electromagnetic field. This potential is expected not to affect appreciably electron emission for high frequencies of the laser pulse, for which surface electrons are not able to follow the fast fluctuations of the field. But for frequencies of the pulse close or lower than the surface plasmon frequency, the induced potential becomes comparable to the laser perturbation and its effect cannot be neglected. With this goal we introduce a simple model, named *Surface Jellium-Volkov* (SJV) approximation, which includes information about the action of the surface induced potential, taking into account the main features of the process.

The SJV approach is a time-dependent distorted wave method that makes use of the well-known Volkov phase [6.11] to describe the interaction of the active electron with the laser and the induced fields, while the surface potential is represented within the jellium model. This kind of one-active electron theories has been recently applied to study different laser-induced electron emission processes from metal surfaces, providing reasonable predictions [6.12–6.15]. To corroborate the validity of the proposed approximation, we compare SJV results with the numerical solution of the time-dependent Schrödinger equation (TDSE), in which the contribution of the surface induced potential is also included. The induced potential is here obtained from a linear response theory by considering a jellium model for a one-dimensional slab.

With both methods - SJV and TDSE - we calculate the probability of electron emission from the valence band of an Al surface, considering

different frequencies and durations of the laser pulse. We analyze in detail the effect of the induced potential on electron distributions by comparing to values derived from the previous *Impulsive Jellium-Volkov* (IJV) approximation [6.13], which does not contain the dynamic response of the surface.

The article is organized as follows. In Section 6.2 we present the theory, in Section 6.3 results are shown and discussed, and finally in Section 6.4 conclusions are summarized. Atomic units are used throughout unless otherwise stated.

6.2 Theory

Let us consider a laser pulse impinging grazingly on a metal surface (S). As a consequence of the interaction, an electron (e) of the valence band of the solid, initially in the state i, is ejected above the vacuum level, ending in a final state f. The frame of reference is placed at the position of the crystal border, with the $\hat{z}$ axis perpendicular to the surface, pointing towards the vacuum region.

For this collision system we can write the Hamiltonian corresponding to the interacting electron as:

$$H = H_0 + V_L + V_{ind}, \tag{6.1}$$

where $H_0 = -\nabla^2_{\mathbf{r}}/2 + V_S$ is the unperturbed Hamiltonian, with V_S the electron-surface potential, and $V_L = \mathbf{r}.\mathbf{F}(t)$ represents the electron interaction with the laser field $\mathbf{F}(t)$ at the time t, expressed in the length gauge. In Eq.(6.1), V_{ind} denotes the surface induced potential, which is originated by electronic density fluctuations produced by the external field.

The electron interaction with the surface, V_S, is here described with the jellium model, being $V_S = -V_c\Theta(-z)$ with $V_c = E_F + E_W$, where E_F is the Fermi energy, E_W is the work function and Θ denotes the unitary Heaviside function. This simple surface model has proved to give an adequate description of the electron-surface interaction for electron excitations from the valence band of metal surfaces [6.13–6.17]. Within the jellium model the unperturbed electronic states, eigenstates of H_0, are written as:

$$\Phi^{\pm}_{\mathbf{k}}(\mathbf{r}, t) = \frac{e^{i\mathbf{k}_s.\mathbf{r}_s}}{2\pi}\phi^{\pm}_{k_z}(z)e^{-iE_{\mathbf{k}}t}, \tag{6.2}$$

where the position vector of the active electron e is expressed as $\mathbf{r} \equiv (\mathbf{r}_s, z)$, with $\mathbf{r}_s$ and z the components parallel and perpendicular to the surface, respectively. The vector $\mathbf{k} = (\mathbf{k}_s, k_z)$ is the momentum measured inside the solid and $E_{\mathbf{k}} = k_s^2/2 + \epsilon_{k_z}$ corresponds to the electron energy. The signs $\pm$ define the outgoing (+) and incoming (-) asymptotic conditions of the collision problem and the eigenfunctions $\phi_{k_z}^{\pm}(z)$ with eigenenergy ϵ_{k_z} are given in the Appendix of Ref. [6.18].

Taking into account the grazing incidence condition, together with the translational invariance of V_S in the direction parallel to the surface, we choose the electric field $\mathbf{F}(t)$ perpendicular to the surface plane, that is, along the $\hat{z}$-axis. The temporal profile of the pulse is defined as:

$$F(t) = F_0 \sin(\omega t + \varphi) \sin^2(\pi t/\tau) \tag{6.3}$$

for $0 < t < \tau$ and 0 elsewhere, where F_0 is the maximum field strength, ω is the carrier frequency, φ represents the carrier envelope phase, and τ determines the duration of the pulse.

The differential probability of electron emission from the surface is expressed in terms of the transition matrix as:

$$\frac{dP}{d\mathbf{k}'_f} = \rho_e \frac{k'_{fz}}{k_{fz}} \int d\mathbf{k}_i \; \Theta(v_F - k_i) \; |T_{if}|^2 \,, \tag{6.4}$$

where T_{if} is T-matrix element corresponding to the inelastic transition $\mathbf{k}_i \rightarrow \mathbf{k}'_f$ and $\mathbf{k}'_f = (\mathbf{k}_{fs}, k'_{fz})$ is the final electron momentum outside the solid, with $k'_{fz} = \left(k_{fz}^2 - 2V_c \right)^{1/2}$. In Eq. (6.4), $\rho_e = 2$ takes into account the spin states and Θ restricts the initial states to those contained within the Fermi sphere, with $v_F = (2E_F)^{1/2}$. The angular distribution of emitted electron can be derived in a straightforward way from Eq. (6.4) as $d^2P/dE_f d\Omega_f = k'_f \, dP/d\mathbf{k}'_f$, where E_f and Ω_f are the final energy and solid angle, respectively, of the ejected electron and $k'_f = \left| \mathbf{k}'_f \right|$.

In this work we evaluate T_{if} by using two different methods: the SJV approximation and the numerical solution of the TDSE. Both of them are summarized below.

6.2.1 Surface Jellium-Volkov approximation

In the SJV theory, the final distorted state is represented by the Surface Jellium Volkov wave function, which includes the actions of the laser field and the induced potential on the emitted electron, both described by means of the Volkov phase. The induced potential is derived from a linear response theory by using a one-dimensional jellium model [6.19]. It can be expressed as $V_{ind}(z,t) = z\ g(t)$ inside the solid, with the function $g(t)$ numerically determined, while outside the solid - in the vacuum region- $V_{ind}(z,t) = 0$. Hence, the final SJV wave function can be written as

$$\chi_f^{(SJV)-}(\mathbf{r},t) = \Phi_{\mathbf{k}_f}^-(\mathbf{r},t) \exp\left[iD_L^-(k_{fz},z,t)\right] \xi_{ind}(z,t), \tag{6.5}$$

where $\Phi_{\mathbf{k}_f}^-(\mathbf{r},t)$ is the unperturbed final state given by Eq.(6.2), which includes the asymptotic condition corresponding to emission towards the vacuum zone (external ionization process [6.18]). In Eq. (6.5), the function D_L^- represents the Volkov phase associated with the laser field, which is expressed as:

$$D_L^-(k_{fz},z,t) = \frac{z}{c}\ A^-(t) - \beta^-(t) - k_{fz}\ \alpha^-(t). \tag{6.6}$$

The temporal functions involved in Eq. (6.6) are related to the vector potential $A^-(t)$, the ponderomotive energy $\beta^-(t)$ and the quiver amplitude $\alpha^-(t)$ of the pulse, being defined as:

$$\begin{aligned} A^-(t) &= -c\int_{+\infty}^{t} dt' F(t'), \\ \beta^-(t) &= (2c^2)^{-1}\int_{+\infty}^{t} dt' [A^-(t')]^2, \\ \alpha^-(t) &= c^{-1}\int_{+\infty}^{t} dt' A^-(t'), \end{aligned} \tag{6.7}$$

with c the speed of light. In a similar way we express the function ξ_{ind}, which considers the action of the induced potential on the active electron, as

$$\xi_{ind}(z,t) = \begin{cases} \exp[i(z/c)A_{ind}^-(t)] & \text{for} \quad z \le 0 \\ 1 & \text{for} \quad z > 0 \end{cases}, \tag{6.8}$$

with $A_{ind}^{-} = -c \int_{+\infty}^{t} dt' \; g(t')$ the momentum transferred by the induced field. Note that the effect of the image charge of the emitted electron was not taken into account in the final distorted wave function $\chi_f^{(SJV)-}$ because its contribution has been found negligible [6.20].

Employing the final SJV wave function given by Eq. (6.5) within a time-dependent distorted-wave formalism [6.21], the transition amplitude reads:

$$T_{if}^{(SJV)} = T^{(C)} + T^{(PC)}, \tag{6.9}$$

where

$$T^{(C)} = -i \int_{0}^{\tau} dt \left\langle \chi_f^{(SJV)-}(t) \left| U(t) \right| \Phi_{\mathbf{k}_i}^{+}(t) \right\rangle \tag{6.10}$$

represents the primary or collision (C) term, with $U(z,t) = V_L(z,t) + V_{ind}(z,t)$ the perturbation introduced by the laser and the induced fields and $\Phi_{\mathbf{k}_i}^{+}$ the unperturbed initial state, given by Eq. (6.2). The second term of Eq. (6.9), $T^{(PC)}$, is here called post-collision (PC) transition amplitude, corresponding to the emission process after the pulse turns off at the time τ. It reads:

$$T^{(PC)} = -i \int_{\tau}^{+\infty} dt \left\langle \chi_f^{(SJV)-}(t) \left| V_{ind}(t) \right| \Phi_{\mathbf{k}_i}^{+}(t) \right\rangle. \tag{6.11}$$

6.2.2 TDSE solution

Replacing the semi-infinite jellium potential by the one corresponding to a one-dimensional slab of size a, $V_{slab} = -V_c \; \Theta(a/2 - z) \; \Theta(a/2 + z)$, and taking into account the symmetry of the system in the direction parallel to the surface, we can write the unperturbed eigenstates as

$$\Phi_{\mathbf{k},n}(\mathbf{r},t) = \frac{e^{i\mathbf{k}_s \cdot \mathbf{r}_s}}{2\pi} \varphi_n(z) e^{-iE_{\mathbf{k}}t}, \tag{6.12}$$

where now the functions $\varphi_n(z)$ are the discretized one-dimensional eigenstates of the slab potential.

The time evolution of the electronic eigenstates under the laser pulse perturbation is governed by the one-dimensional time-dependent Schrödinger equation

$$i\frac{\partial}{\partial t}\varphi_n(z,t) = H(z,t)\varphi_n(z,t), \tag{6.13}$$

where the unperturbed part of the Hamiltonian $H(z,t)$ is now $H_0 = -(1/2)(d^2/dz^2) + V_{slab}$.

The discrete time step evolution is given by the evolution operator

$$\varphi_n(z,t+\Delta t) = exp(-i\Delta t H)\varphi_n(z,t), \tag{6.14}$$

which is computed by using the Crank-Nicholson scheme, approximating the exponential by the Cayley form [6.22]

$$exp(-i\Delta t H) \approx \frac{1-\frac{i\Delta t}{2}H}{1+\frac{i\Delta t}{2}H}. \tag{6.15}$$

This scheme is unitary, unconditionally stable, and accurate up to order $(H\Delta t)^2$.

To obtain the transition amplitude we evolve every eigenstate within the Fermi sphere of the unperturbed slab, projecting then the evolved states over the discretization box "continuum" states, $\varphi_f^k(z)$,

$$T_{if}^{(TDSE)} = \left\langle \varphi_f^k(z) | \varphi_i(z, t\to\infty) \right\rangle. \tag{6.16}$$

Independence of the results with different slab sizes guarantees that the used slab size accurately represents the semi-infinite medium. For the simulation box we have taken completely reflective walls as boundary conditions.

6.3 Results

We applied the SJV and TDSE methods to study electron emission from the valence band of an Al(111) surface produced as a consequence of grazing incidence of ultrashort and intense laser pulses. As Aluminum is a typical metal surface, it will be considered as a benchmark for the theory. The Al(111) is described by the following parameters: the Fermi

energy $E_F = 0.414$ a.u., the work function $E_W = 0.156$ a.u., and the surface plasmon frequency $\omega_s = 0.4$ a.u..

For the TDSE calculations a slab with a width of 311.54 a.u. (142 Aluminum atomic layers), surrounded by 244.23 a.u. of vacuum on each side, was used. The grid sizes were $\Delta z = 0.1$ a.u. for the spacial grid and $\Delta t = 0.005$ a.u. for the time grid. The time evolution was considered finished when the induced potential had decayed two orders of magnitude from its value at the moment the laser pulse was switched off, at $t = \tau$. The same criteria was used to evaluate the upper limit of the time integral of Eq. (6.11). Note that to compare the SJV and TDSE results it is necessary to take into account that the former theory includes the proper asymptotic conditions, distinguishing the external from the internal ionization processes, while the latter does not. Then, as a first estimation we weighted TDSE values with the fraction of electrons emitted towards the vacuum derived from the SJV model [6.13].

In this work we considered symmetric pulses, with $\varphi = -\omega\tau/2 + \pi/2$. The field strength was fixed as $F_0 = 0.001$ a.u.($I \simeq 4\ 10^{10}$ W/cm^2), which belongs to the perturbative regime, far from the saturation region and the damage threshold [6.23, 6.24]. In accord with results of a previous theory [6.13], the maximum of the emission probability corresponds to the angle $\theta_e = 90^o$, which coincides with the orientation of the laser field. Therefore, all results presented here refer to this emission angle.

Since the dynamic response of the surface is characterized by the surface plasmon frequency ω_s, in order to investigate the influence of the induced potential we varied the carrier frequency ω of the laser field around the value of ω_s. We start considering laser pulses with several oscillations inside the envelope function, which correspond to the so-called multiphoton regime. In this regime, related to a Keldysh parameter $\gamma = \omega\sqrt{E_W}/F_0$ [6.25] greater than the unity, the laser frequency tends to the photon energy and the electron spectrum displays maxima associated with the absorption of photons.

In Fig. 6.1, six-cycle laser pulses with three different frequencies were considered: $\omega = 0.7$, 0.4 and 0.2 a.u.. In all the cases, to analyze the effect of the surface response on the electronic spectra SJV and TDSE values were compared to data derived within the previous IJV approach [6.13], which neglects the contribution of V_{ind}. In Fig. 6.1 (a) we show the emission probability corresponding to the frequency $\omega = 0.7$ a.u., which is higher than the surface plasmon frequency. For this frequency a good

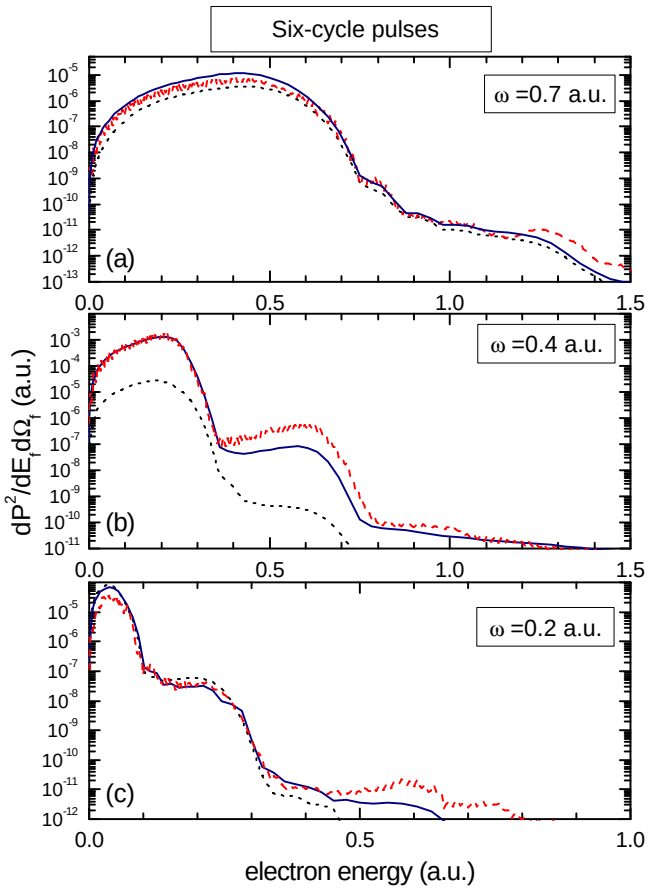

Figure 1

Figure 6.1: Differential electron emission probability, as a function of the electron energy, for the emission angle $\theta_e = 90°$. The parameters of the laser field are: $F_0 = 0.001$ a.u., (a) $\omega = 0.7$ a.u., $\tau = 54$ a.u., (b) $\omega = 0.4$ a.u., $\tau = 95$ a.u.and (c) $\omega = 0.2$ a.u., $\tau = 190$ a.u. Solid (blue) line, SJV results; dashed (red) line, TDSE values, and dotted line, results of the IJV model.

agreement between SJV and TDSE results is found. The SJV curve runs very close to TDSE values, showing only a small underestimation of TDSE results in high-velocity range. Note that both theories present a broad maximum, which can be associated with the above threshold ionization process. From the comparison to values obtained within the IJV approximation, we observe that for this high frequency the induced potential produces only a slight increment of the probability at low elec-

tron energies, having small influence on the overall electronic spectrum. However, when ω becomes resonant with the surface plasmon frequency, as in Fig. 6.1 (b), the induced potential contributes greatly to increase the ionization probability in the whole energy range. Energy distributions obtained with SJV and TDSE methods are more than one order of magnitude higher than the one derived from the IJV approach. In this case SJV results follows quantitatively well the behavior of the TDSE curve, describing properly the positions of the multiphoton maxima but underestimating TDSE probabilities around the second peak. Note that in this case V_{ind} does not represent a weak perturbation of the laser field, as shown in Fig. 6.2(b) and it might be the origin of the observed discrepancy. In Fig. 6.1 (c) we plot the emission probability for a laser field with a frequency $\omega = 0.2$ a.u., lower than the plasmon one. Again, as in Fig. 6.1 (a) SJV and TDSE results run very close to each other, displaying almost no differences with the IJV theory, which does not contain the induced potential. This indicates that the induced potential strongly affects emission spectra for frequencies resonant with the surface plasmon frequency, while for small deviations from this frequency it plays a minor role in the multiphoton ionization process.

With the aim of examinating in detail the contribution of the induced potential, in Fig. 6.2 we plot V_{ind} as a function of time, for a given position inside the solid and for the frequencies of Fig. 6.1(a) and (b). We observe that for $\omega = 0.7$ a.u. the induced potential tends to follow the oscillations of the external field and its intensity steeply diminished when the pulse is turned off. Then, in this case the collective response of the medium produces only a weak effect on the electronic spectrum, as shown in Fig. 6.1(a). Whereas for laser frequencies near to ω_s (Fig. 6.2 (b)) the process is dominated by the induced potential, which produces an increment of the emission probability, as observed in Fig. 6.1(b).

Finally, in Fig. 6.3 we study a six-cycle laser pulse with the frequency corresponding to the experimental value for the Ti:sapphire laser system [6.9] ($\omega = 0.057$ a.u.). For this low frequency, almost one order of magnitude lower than the plasmon one, the surface response approximates to the static limit and electronic fluctuations screen strongly the external field inside the solid. By comparing SJV and IJV results it is observed that in this case the induced potential contributes to reduce markedly the emission probability, up to two orders of magnitude at low electron energies. On the other hand, it should be noted that although the SJV theory describes properly the positions of multiphotonic maxima, it

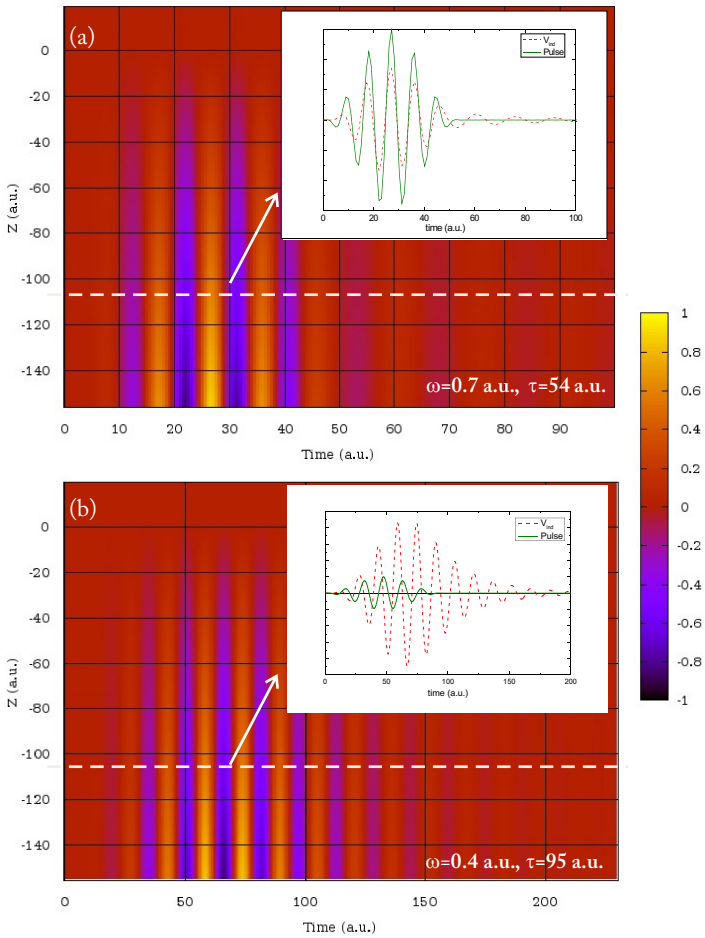

Figure 2

Figure 6.2: 2D-Representation of the induced potential, as a function of time and space. Laser pulse parameters are similar to Fig. 6.1(a) and (b). Inset figures correspond to a given position inside the solid, with solid line, the laser pulse curve, and dashed line, the induced potential.

overestimates the emission probability given by the TDSE method. Such a discrepancy, which arises when ω is lower than the mean energy of initial bound electrons, was also observed for other Volkov-type methods applied to photoionization of atomic targets [6.26].

To complete the previous analysis we reduce the duration of the pulse in order to investigate the contribution of the induced potential for photoelectron emission in the collisional regime [6.26]. In this regime, associ-

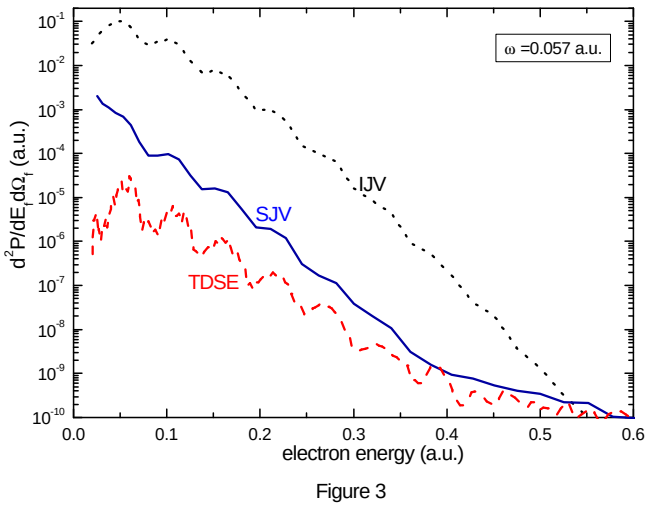

Figure 6.3: Similar to Fig. 6.1. Laser field with $F_0 = 0.001$ a.u., frequency $\omega = 0.057$ a.u. and duration $\tau = 660$ a.u.

ated with half-cycle pulses, the electromagnetic field does not oscillate, producing a perturbation similar to the one resulting of the interaction with a swift ion impinging grazingly on the surface (collision process). Notice that for such ultrashort pulses the carrier frequency ω loses its meaning and the pulse can be characterized by the sudden momentum transferred to the ejected electron, $\Delta p = -A^-(0)/c \simeq F_0\tau/2$ [6.27]. In Fig. 6.4 we plot electron distributions for half-cycle pulses with two different durations $\tau = 4.5$ and 16 a.u. In both cases we found a good agreement between SJV and TDSE methods in the whole electron velocity range. Both theories present a pronounced maximum at low electron velocities, which does not appear in the electron distribution derived from the IJV approach, being produced by the induced potential. To understand the origin of this increment of the probability at low electron energies, in Fig. 6.5 we plot again the induced potential for a given position inside the solid, now for the case of Fig. 6.4 (a). We observe that for half-cycle pulses, without oscillations, after the pulse has finished the induced potential still affects solid electrons during at least a hundred atomic units more. This effect is the main source of electrons emission at low velocities.

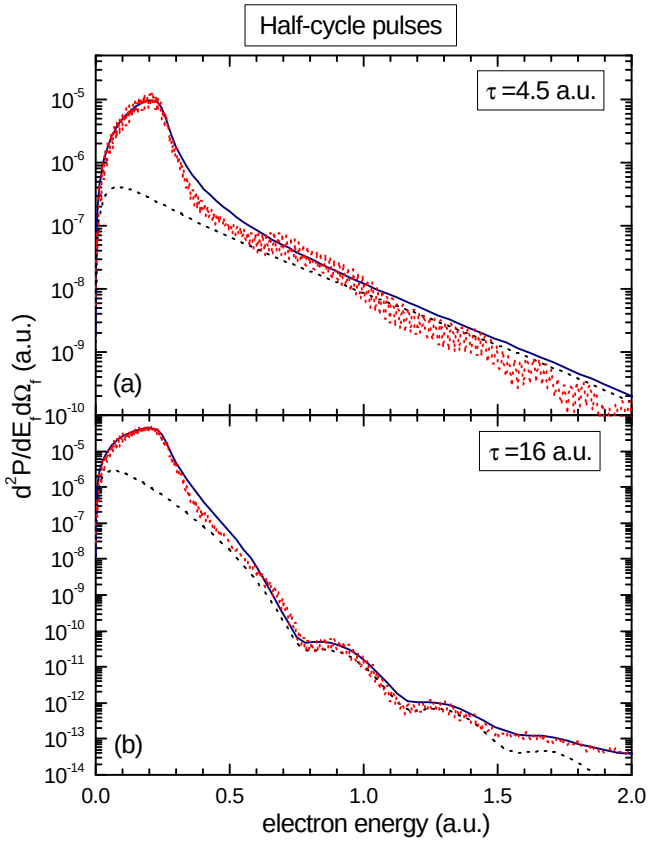

Figure 4

Figure 6.4: Similar to Fig. 6.1. Half-cycle pulse with $F_0 = 0.001$ a.u., (a) frequency $\omega = 0.7$ a.u. and duration $\tau = 4.5$ a.u., (b) frequency $\omega = 0.2$ a.u. and duration $\tau = 16$ a.u..

6.4 Conclusions

In the present work we have introduced the SJV approximation, which allowed us to investigate the effects of the induced potential on the electron emission process. The proposed theory was compared to values derived from the numerical solution of the corresponding TDSE, displaying a good description of the main characteristics of photoemission spectra in the whole range of studied frequencies and durations of the laser pulse. From the comparison between SJV probabilities and those derived from the previous IJV approach, which does not include V_{ind}, we conclude

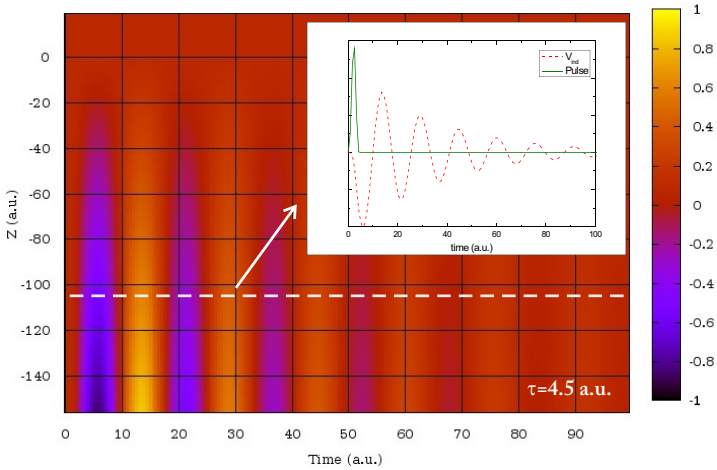

Figure 5

Figure 6.5: Similar to Fig. 6.2. Laser field with $F_0 = 0.001$ a.u., $\omega = 0.7$ a.u. and $\tau = 4.5$ a.u..

that the induced potential can play an important role in laser-induced electron emission from metal surfaces, as expected. For laser pulses with several oscillations inside the envelope, we found that the induced potential produces a considerable increment of the probability when the laser frequency is resonant with the surface plasmon one, but as ω diminishes tending to the static case, the surface electronic density shields the laser field inside the solid, leading to a markedly reduction of the photoemission process. In addition, for electromagnetic pulses in the collisional regime, the contribution of the surface induced potential after the pulse turns off gives rise to a maximum in the emission spectrum at low energies.

6.5 Acknowledgment

This work was done with the financial support of Grants UBACyT, ANPCyT and CONICET of Argentina. I. A, A. A. and V. M. S. gratefully acknowledge financial support by GU-UPV/EHU (grant no. IT-366-07) and MCI (grant no. FIS2007-66711-C02-02). The work of V.M.S is sponsored by the IKERBASQUE foundation.

6.6 References

[6.1] A. L. Cavalieri, *et al.* Nature (London), **449**, 1029 (2007).

[6.2] E. Goulielmakis, V. S. Yakovlev, A. L. Cavalieri, M. Uiberacker, V. Pervak, A. Apolonski, R. Kienberger, U. Kleineberg, F. Krausz, Science **317**, 769 (2007).

[6.3] R. Kienberger *et al.* Nature (London), **427**, 817 (2004).

[6.4] C. A. Haworth, L. E. Chipperfield, J. S. Robinson, P. L. Knight, J. P. Marangos and J. W. G. Tisch, Nature Physics **3**, 52 (2007).

[6.5] A. Baltuska, *et al.* Nature (London) **421**, 611 (2003).

[6.6] E. Lorin, S. Chelkowski and A. D. Bandrauk, New Journal of Physics **10**, 025033 (2008).

[6.7] D. B. Milošević, G. G. Paulus, D. Bauer and W. Becker, J. Phys. B **39**, R203 (2006).

[6.8] M. F. Kling, J.Rauschenberger, A. J. Verhoef, E. Hasovic, T. Uphues, D.B. Milosevic, H. G. Muller and M.J.J. Vrakking, New Journal of Physics **10**, 025024 (2008).

[6.9] L. Miaja-Avila *et al.* Phys. Rev. Lett. **101**, 046101 (2008).

[6.10] C. Lemell, B. Solleder, K. Tőkési, and J. Burgdörfer, Phys. Rev. A. **79**, 062901 (2009).

[6.11] D. M. Volkov, Z. Phys. **94**, 250 (1935).

[6.12] F..H. M. Faisal, J. Z. Kamiński and E. Saczuk, Phys. Rev. A. **72**, 023412 (2005).

[6.13] M. N. Faraggi, M. S. Gravielle and D. M. Mitnik, Phys. Rev. A **76**, 012903 (2007).

[6.14] J.C. Baggesen and L.B. Madsen, Phys. Rev. A **78**, 032903 (2008).

[6.15] C.-H. Zhang and U. Thumm, Phys. Rev. Lett. **102**, 123601 (2009).

[6.16] M.S. Gravielle and J.E. Miraglia, Phys. Rev. A **65**, 022901 (2002).

[6.17] P. Kurpick, U. Thumm and U. Wille, Phys. Rev. A **56,** 543-554 (1997).

[6.18] M. S. Gravielle, Phys. Rev. A **58**, 4622 (1998).

[6.19] M. Alducin, V. M. Silkin, J.I. Juaristi and E. V. Chulkov, Phys. Rev A **67**, 032903 (2003).

[6.20] P. Dombi, F. Krausz and G. Farkas, J. Mod. Optics **53**,163 (2006).

[6.21] D. P. Dewangan and J. Eichler, Phys. Rep. **247**, 59-219 (1997).

[6.22] W. H. Press, S. A. Teukolsky, W.T. Vetterling and B.P. Flannery, *Numerical Recipes* (Cambridge University Press, New York, 1992).

[6.23] G. Saathoff, L. Miaja-Avila, M. Aeschlimann, M. M. Murnane, and H.C. Kapteyn, Phys. Rev. A **77**, 022903 (2008).

[6.24] L. Miaja-Avila, J. Yin, S. Backus, G. Saathoff, M. Aeschlimann, M. M. Murnane, and H.C. Kapteyn, Phys. Rev. A **79**, 030901(R) (2009).

[6.25] L.V. Keldysh, Sov. Phys. JETP **20**, 1307 (1965).

[6.26] P. Macri, J. E. Miraglia and M. S. Gravielle, J. Optical Society of America B **20**, 1801 (2003).

[6.27] D.G. Arbó, K. Tőkési and J.E. Miraglia, Nucl. Instr. and Meth. B **267**, 382 (2009).

General conclusions

As the systems under study and the techniques used to analyze them were significantly different in the three Parts in which the present thesis is divided, we group here by these Parts, even if being a brief summary, the general conclusions obtained.

Part I: Electron emission in grazing collisions of protons with insulator surfaces

In Part I of our study, we essentially dealt with the same proton–surface collision system, only moving to a higher level of sophistication in the model used, as the project evolved.

We first saw that, with a simple atomic binary collision model, we could qualitative reproduce the convoy peak behaviour as a function of the electron emission angle. Furthermore, the model could be easily extended to other target surfaces by means of the material incoherent scattering function.

As we extended the study by taking into account electrons emitted from the surface, as well as the charge state of the projectile along its trajectory, we could measure the different contributions from the surface and projectile electrons to the convoy peak. By computing these contributions for the H^+–LiF case we found that, at convoy peak energies and low emission angles, both of them are of the same order of magnitude, being the projectile one higher. We also saw that, as we move to higher emissions angles, the surface electrons contribution to the convoy

peak becomes negligible and all convoy electrons come from the projectile ionization.

We then generalized the study to include other ionic crystal surfaces (KCl and KI) and projectiles (H^0). Once we computed the total electron emission yield in the collision process, we found that the main contribution to this emission are the surface electrons directly ionized by the bare proton (ECC electrons), both in the H^0 and H^+ case. This is essentially due to the fact that the projectile along the collision path has about one order of magnitude more probability of being in its ionized state than in its neutralized one, thus its electrons barely contribute to the total emission.

So, all in all, we found a good way to describe the contribution of the projectile electrons to the convoy peak and also to the total emission yield which allowed us to determine that i) the main contribution to the convoy peak is due to the projectile emitted electrons, and that ii) those convoy peak electrons barely contribute to the total electron emission product of the collisions, which is mainly due to the surface emitted electrons.

Part II: Field Emission Resonances in Cu(100) surfaces

In Part II we focused on two different systems, both of them having to do with spectroscopic measurements on Cu(100) surfaces. We specifically modelled a STM–surface system, working in its tunneling spectroscopy mode and in the field emission resonances regime.

In the first work we could see the role played by the STM tip lateral size in the formation of wave patterns, as is is experimentally observed. Additionally, we explained the broadening of the peaks observed in dI/dV spectra as due to the dynamic method of measurement, i.e. in constant current mode. We thus showed that STS in the field emission regime can be used to gain information about the electron dynamics and surface electronic properties at energies above the vacuum level.

In the second work, the effect that nano-scale adsorbate islands have on the clean surface FERs was studied. Comparison of the numerical spectra obtained from calculations for the clean surface and for the surface with the adsorbed islands on top, allowed us to undoubtedly assign the resonances to a metal-like or island-like origin.

The cylindrical symmetry present in our model allowed us to split the calculations in m-symmetry subspaces[1] and thus study the resonances origin accordingly. From this analysis we could conclude that the metal-like resonances are delocalized along the surface having contributions from all m channels, while the island-localized ones have a well defined m-character. We also could see that, because of the effect of the centrifugal barrier, the number of island localized states decreases with increasing m. This effect is so pronounced that, in our specific case or small islands, we could say that essentially only island resonances from the $m = 0$ channel contribute to the final spectra. That is, for the island states, the transmission is significant for the $m = 0$ subspace only.

Our model also allowed us to produce two-dimensional cuts of the charge density in planes parallel to the surface at bias voltages at which the different resonances were observed. These plots could be compared with the experimentally measured dI/dV maps, showing good agreement with them. These calculations also showed us that the island-like FERs are spatially localized at the center of the islands whereas the mixed states form ring-shaped structures extending outside the island boundaries.

Part III: Laser induced electron emission in metals

In Part III, linking Parts I and II of the thesis, we studied the electron emission spectra of a metallic surface under the influence of a laser pulse. Specifically, we were interested in the influence that the induced potential produced by this same laser pulse has on the electron emission process.

Even if lacking direct experimental measurements to compare with, we could compare the two different approaches used which accounted for the surface induced potential. Both models calculations showed a strong qualitative and quantitative agreement in all the laser frequencies studied, above, around, and below the plasmon frequency, and for different pulse durations. However, the reference model not accounting for the induced potential showed, as expected, discrepancies with these results.

We saw that for laser frequencies resonant with the surface plasmon, the induced potential produces a considerable increase of the electron emission probability. As the laser frequency diminishes towards the static

[1] being m the projection of the angular momentum over the symmetry axis, z.

case, the surface electronic density shields the laser field inside the solid, leading to a reduction of the emitted electrons.

We also studied pulses in the so-called collisional regime, associated with half-cycle pulses, where the electromagnetic field does not oscillate and produces a perturbation similar to that of a swift ion impinging grazingly on the surface. In those cases, after the pulse has finished, we could see that the induced potential keeps bumping for quite a long time while fading away. This effect induces an electron emission at low velocities, giving a maximum in the emission spectra at low energies which does not appear in the calculations ignoring the induced potential.

List of Publications

We present here the main scientific contributions derived from this thesis work, both in the form of papers published in peer reviewed journals as well as conference talks, posters, etc.

Papers published in peer reviewed journals

Every main chapter in this manuscript corresponds to a journal paper cited here, and it is indicated in the own chapters preamble. Reciprocally, the numbering in this section also correponds to the related chapters within this document.

1. I. Aldazabal, V.H. Ponce and A. Arnau,
   Grazing incidence collisions of fast protons with insulators: electron emission around the convoy peak,
   phys. stat. sol. (b) **241** (10), 2374 (2004).
   doi: 110.1002/pssb.200404881

2. I. Aldazabal, M.S. Gravielle, J.E. Miraglia, A. Arnau and V.H. Ponce,
   Role of projectile charge state in convoy electron emission by fast protons colliding with LiF(001),
   Nucl. Instr. and Meth. in Phys. Res. B **232**, 53 (2005). doi: 10.1016/j.nimb.2005.03.024

3. M.S. Gravielle, I. Aldazabal, A. Arnau, V.H. Ponce, J.E. Miraglia, F. Aumayr, S. Lederer and H. Winter,

Electron emission and energy loss in grazing collisions of protons with insulator surfaces,
Phys. Rev. A **76**, 012904 (2007). doi: 10.1103/PhysRevA.76.012904

4. J. I. Pascual, C. Corriol, G. Ceballos, I. Aldazabal, H.-P. Rust, K. Horn, J. M. Pitarke, P. M. Echenique and A. Arnau,
Role of electric field in surface electron dynamics above the vacuum level,
Phys. Rev. B **75**, 165326 (2007).
doi: 10.1103/PhysRevB.75.165326

5. S. Stepanow , A. Mugarza , G. Ceballos, P. Gambardella, I. Aldazabal , A. G. Borisov and A. Arnau,
Localization, splitting, and mixing of field emission resonances induced by alkali metal clusters on Cu(100),
Phys. Rev. B **83**, 115101 (2011).
doi: 10.1103/PhysRevB.83.115101

6. M. N. Faraggi, I. Aldazabal, M. S. Gravielle, A. Arnau and V. M. Silkin,
Study of the induced potential produced by ultrashort pulses on metal surfaces,
J. Opt.Soc. Am B **26** (12), 2331 (2009).
doi: 10.1364/JOSAB.26.002331

Contributions to conferences, workshops, etc.

- **Authors:** I. Aldazabal, V. Ponce, A. Arnau
  Title: Contribution from the projectile ionised electrons to the Convoy electrons in a Hydrogen - LiF surface grazing collision; a first approach.
  Type of contribution: Poster
  Congress: 5th Donostia Encounters on Particle-Solid Interactions. 8-13 Sept. 2003. San Sebastian, Spain

- **Authors:** I. Aldazabal, V.H. Ponce, and A. Arnau
  Title: Grazing incidence collisions of fast protons with insulators: electron emission around the convoy peak
  Type of contribution: Talk (A. Arnau)
  Congress: Congreso Latinoamericano de Ciencias de Superficies y

sus Aplicaciones - CLACSA - XI. 7-12 Dec. 2003. Pucon, Chile

- **Authors:** I. Aldazabal, M.S. Gravielle, J.E. Miraglia, A. Arnau, V.H. Ponce
  Title: Role of projectile charge state in convoy electron emission by fast protons colliding with LiF(001)
  Type of contribution: Poster
  Congress: 15th International Workshop on Inelastic Ion Surface Collisions (IISC-15). 17-22 Oct. 2004. Ise-Shima, Japan

- **Authors:** I. Aldazabal, M.S. Gravielle, A. Arnau, J.E. Miraglia, and V.H. Ponce
  Title: Convoy electron emission and energy loss of swift protons in grazing collision against LiF(001), ClK(001) and IK(001) surfaces
  Type of contribution: Talk (I. Aldazabal)
  Congress: 16th International Workshop on Inelastic Ion Surface Collisions (IISC-16). 17-22 Sept. 2006. Schloss Hemstein, Austria

- **Authors:** D.M. Mitnik, I. Aldazabal, A. Arnau, M.S. Gravielle, J.E. Miraglia, and V.H. Ponce
  Title: Time-dependent simulations of electron emission in grazing ion-surface collisions
  Type of contribution: Poster
  Congress: 16th International Workshop on Inelastic Ion Surface Collisions (IISC-16). 17-22 Sept. 2006. Schloss Hemstein, Austria

- **Authors:** D.M. Mitnik, A. Arnau, I. Aldazabal and V.H. Ponce
  Title: Time–dependent simulations: Acceleration and deceleration of convoy electrons in grazing–ion–surface collisions
  Type of contribution: Poster
  Congress: XX International Symposium on Ion–Atom collisions (ISIAC). 1-4 Aug. 2007. Crete, Greece

- **Authors:** D.M. Mitnik, A. Arnau, I. Aldazabal and V.H. Ponce
  Title: Time–dependent simulations of electron emission in grazing ion-surfaces collisions
  Type of contribution: Invited talk (D. M. Mitnik)

Congress: XX International Symposium on Ion–Atom collisions (ISIAC). 1-4 Aug 2007. Crete, Greece

- **Authors:** M.N. Faraggi, I. Aldazabal, M.S. Gravielle, A. Arnau, V. M. Silkin
  Title: Efectos del potencial inducido en la fotoemisión desde superficies metálicas
  Type of contribution: Poster
  Congress: IV Encuentro Sudamericano de Colisiones Inelásticas en la Materia. 29-31 Oct. 2008. Rio de Janeiro, Brasil

- **Authors:** M.N. Faraggi, I. Aldazabal, M.S. Gravielle, A. Arnau, V. M. Silkin
  Title: Effects of the induced potential on the photoelectron emission from a metal surface
  Type of contribution: Poster
  Congress: XXVI International Conference on Photonic, Electronic, and Atomic Collisions (ICPEAC). 22-28 Jul. 2009. Kalamazoo, MI - USA

- **Authors:** M.N. Faraggi, I. Aldazabal, M.S. Gravielle, A. Arnau, V. M. Silkin
  Title: Electron emission from metal surfaces by ultra-short pulses
  Type of contribution: Poster
  Congress: II International Conference on Attosecond Physics. Jul. 28 - Aug. 1 2009. Manhattan, KS - USA

- **Authors:** Stepanow, A. Mugarza, G. Ceballos, and P. Gambardella, I. Aldazabal, A. Borisov and A. Arnau
  Title: Mapping electron resonances on nanosized alkali metal dots grown on Cu(100)
  Type of contribution: Talk (A. Arnau)
  Congress: Symposium on Surface Science - 3S'10. 7-13 March 2010. St. Christoph am Arlberg, Austria

- **Authors:** Stepanow, A. Mugarza, G. Ceballos, and P. Gambardella, I. Aldazabal, A. Borisov and A. Arnau

Title: Mapping electron resonances on nanosized alkali metal dots grown on Cu(100)
Type of contribution: Talk (A. Arnau)
Congress: Conferencia Fuerzas y Túnel 2010. 27-29 Sept. 2010. Tarragona, Spain